MASTER THESIS

APOSTOLOS PANTOUSAS

UNIVERSITY OF CRETE

DEPARTMENT OF MATERIALS SCIENCE

Synthesis and characterization of

2D Layered Halide Perovskite

Quantum Wells

ΠΑΝΕΠΙΣΤΗΜΙΟ
ΚΡΗΤΗΣ

UNIVERSITY
OF CRETE

crystal chemistry lab

Table of Contents

ABSTRACT

Perovskites are a class of semiconducting materials with great interest in optoelectronic applications due to their high efficiency, high absorption coefficients and low cost. Two-dimensional (2D) perovskite structures provide the ability to further tune these properties and manufacture high-performance devices. In this work, we focus on the synthesis and characterization of a new homologous series of 2D layered lead halide perovskites based on the CH3NH3PbBr3 bulk perovskite. The homologous series, with general formula (CH3(CH2)5NH3)2(CH3NH3)n-1PbnBr3n+1, where n corresponds to the number of layers of the perovskite, produces a fertile ground for the study of quantum wells, since the alternating organic and inorganic layers generate a natural, periodic quantum well structure . By tuning the thickness, we control the degree of dielectric and quantum confinement of the photogenerated carriers inside the inorganic layers, thus creating a series of compounds with tunable optical properties in the visible spectrum range. The compounds were synthesized in pure form and their crystal structure was determined via single-crystal X-ray diffraction. The structural phase transitions were monitored via Differential Scanning Calorimetry (DSC) in the -80 – 120 oC temperature range while the optical properties were studied via steady-state and time-resolved photoluminescence (PL) spectroscopy in the -195- 25^{o}C temperature range. The results suggest that the new compounds are excellent excitonic model systems and can be employed in specific applications like LEDs and lasers.

INTRODUCTION

Perovskites are a class of materials that are based on the $CaTiO_3$ mineral crystal structure[1-3]. These materials have been implemented in the development of many new technologies, such as ferroelectric insulators, superconductors and recently as medium and wide gap semiconductors. They have applications in solar cells, LEDs, TFTs, ferroelectrics and more[4-8]. Halide based perovskites, in particular, are employed in applications that rely on the remarkable optoelectronic properties of perovskites, such as tunable energy gap, inverted band structure, and high intensity photoluminescence at room temperature. These properties are related to the crystal structure of perovskites, that is highly modular and exhibits dynamic disorder[9]. The crystal structure of metal-halide perovskites consists of a central, bivalent, generally p-block metal cation, connected to 6 halogen anions, forming an octahedron around the metal[10]. These octahedra are connected to each other via their vertices. To balance the charge, the space between the octahedra is occupied by small, monovalent counter-cations, aka "perovskitizers", residing at the corners of the unit cell. The only cations that can occupy this position are Cs^+, $CH_3NH_3^+$[11] and $HC(NH_2)_2^+$[12]. This structure has the general formula AMX_3[2], where A is the perovskitizer, M is the metal cation and X is the halide anion **(Figure 1)**.

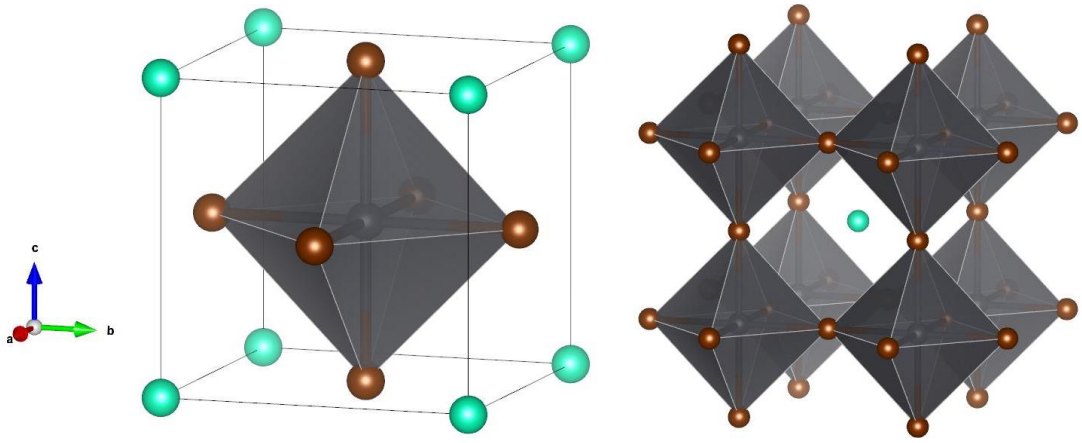

Figure 1: The two equivalent representations of the ideal cubic perovskite unit cell, exemplified in the α-$SrTiO_3$ (oxides) or α-$CsPbI_3$ (halides) perovskites.

Other than selecting different metals, halogens and perovskitizers, it is possible to further modify the perovskite structure by introducing larger cation that cannot act as perovskitizers and, due to size restrictions, do not fit in the space between the octahedra[7, 13]. Such cations are called "spacer cations" and their function is to break some of the bonds between the octahedra, still preserving the structure directing characteristics towards lower dimensionality. Reducing the connectivity between octahedra, a process known for extended solids as dimensional reduction[14] **(Figure 2)**., can be done in a controlled

manner, by selecting appropriate spacers[15]. By using large alkyl chain or aromatic ammonium cations and generally cations that can self-assemble in polar media, one can “force” the anionic octahedra to form layers around the organic self-assemblies. In the case of a lipid-like bilayers, this means that the octahedral connectivity is broken in one direction, producing a two-dimensional, layered perovskite structure. The same process can target connections in more directions, producing one- or zero-dimensional perovskites.

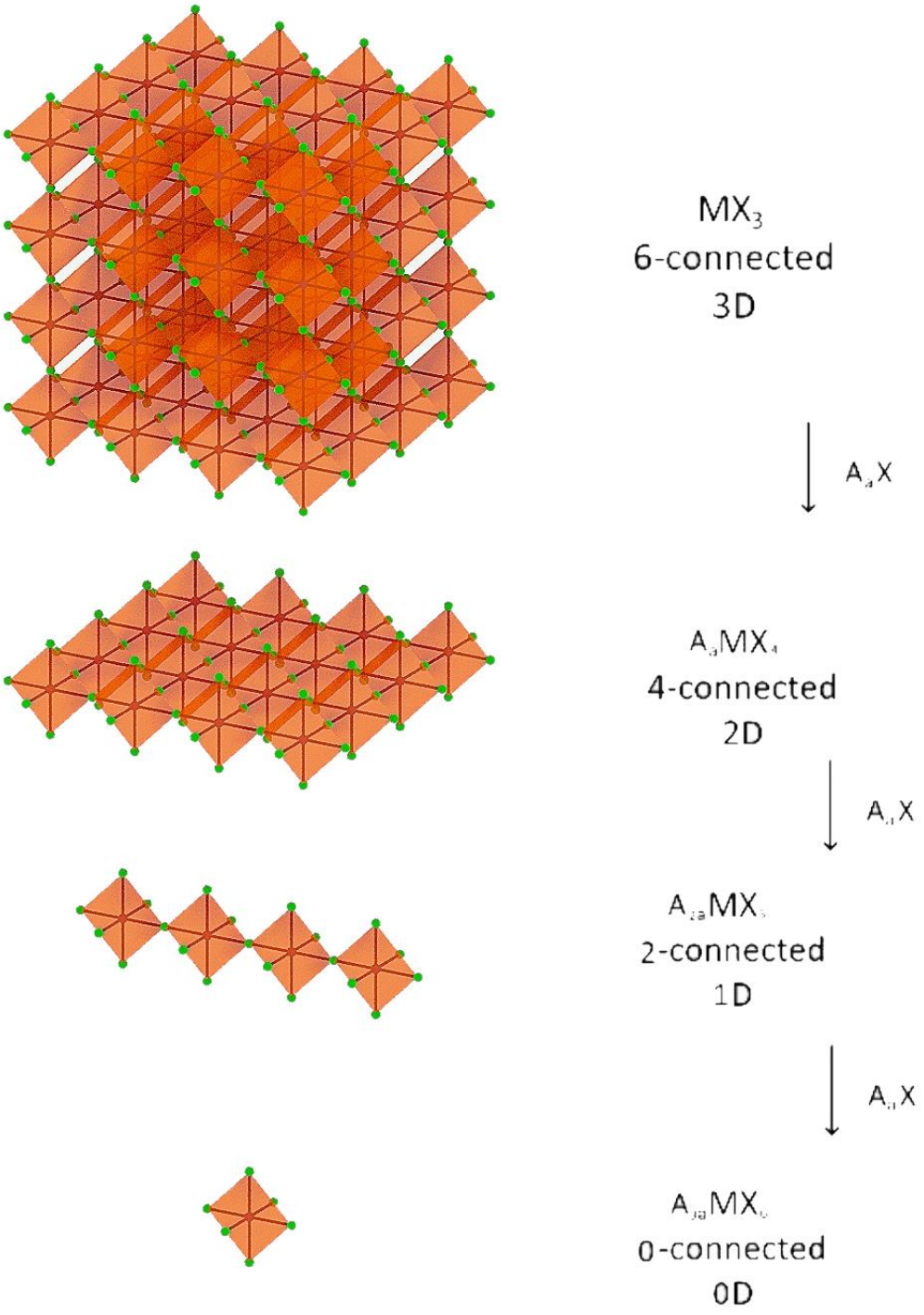

Figure 2: Dimensional reduction of a framework of vertex-sharing octahedra. M and X atoms are represented by blue and green spheres, respectively. Reaction with A_aX incorporates additional X atoms into the M-X framework, inserting into M-X-M bridges to reduce the connectedness and dimensionality of the framework. Figure adapted from [13].

Two-dimensional (2D) perovskites, thus form a wide family of materials that have many permutations regarding their crystal structure. One such classification is the orientation of the 2D sheets with respect to one another. When the octahedra of the different layers are stacked with a shift of half a unit cell, the structure can be classified as a Ruddlesden-Popper structure[16-18]. On the other hand, when the octahedra of the layers are stacked on top of each other, the structure can be classified as a Dion-Jacobson structure **(Figure 3)**.

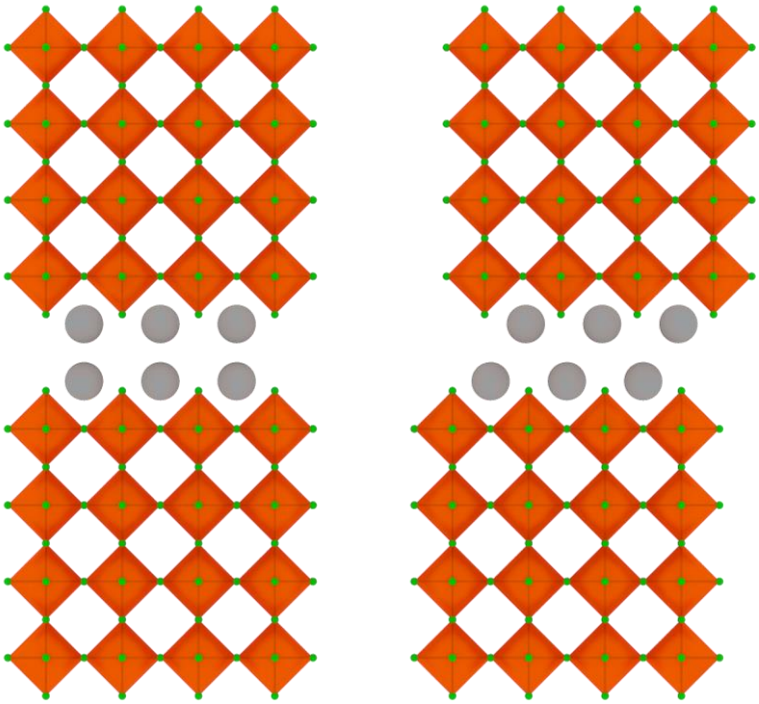

Figure 3: Representation of the difference between Dion-Jacobson (left) and Ruddlesden-Popper (right) phases.

The alternating organic-inorganic layers have a perovskite slab thickness that is constrained to the nanoscale. This allows them to act as multiple quantum wells[19-21] **(Figure 4)**, perfectly ordered on top of each other, with the organic layers acting as potential barriers and the inorganic layers acting as the wells. The length of the well is inversely proportional to the energy gap, which is therefore inversely proportional to the square of the number of layers, resulting to higher wavelength absorption, the higher the number of layers is. This relationship can be surmised by the following formalization (Equation (1)):

$$E = \frac{\hbar^2 n^2 \pi^2}{2mL_z^2} (1)$$

$$n_{layers} \propto L_z$$

where n is the excitation state of the electron, m the electron mass and $L_z$is the quantum thickness proportional to the number of layers[22, 23].

This means that, the energy of any particles (e.g., excitons) travelling through the crystal is greater, and its magnitude directly depends on the degree of confinement. The difference in the dielectric constant of the organic and organic layers is also important, as it causes a secondary form of confinement based on the dielectric gradient and it is termed dielectric confinement. This means that, the energy of the particles (e.g., excitons) travelling through the crystal increases as a result of the coulombic screening (binding energy), simultaneously spatially localizing the particle (Bohr radius) as derived from Equation (2). These phenomena affect the optoelectronic properties of the perovskites, as they act upon the main mechanism of their interaction with light. When the perovskites interact with incident light, they absorb some of its energy, by exciting electrons from their valence band to their conduction band. In the course of a few hundred picoseconds, these electrons return to their ground state, by losing an exact amount of energy corresponding to the two energy levels difference, in the form of photons. Another mechanism is the excitation of electrons which causes them to displace, leaving a hole in their stead. The coulomb interaction between the negatively charged electron and the positively charged hole binds them together, forming a quasiparticle, called exciton. By confining the exciton through quantum and dielectric confinement, its energy is greatly increased. As a result, by engineering the thickness of the perovskite layers, it is possible to tune the energy gap of the material (spatial confinement) as well as the degree of interaction between the photo-generated excited states (dielectric confinement). The energy holding the electron-hole pair together is called exciton binding energy and can be extrapolated using the model of the hydrogen atom, modified to account for the difference in dielectric constant between the organic and inorganic layers, as a function of their thickness (Equation (3)), as well as the reduced mass of the hole and the electron in each material (Equation (2)). As such, the equation can also yield an equivalent Bohr radius, which we use to classify excitons as Mott-Wannier[24] excitons or Frenkel[25] excitons (Equation (4))[26, 27].

$$E_b = \frac{\mu e^4}{8h^2 {\varepsilon_0}^2 {\varepsilon_{eff}}^2} \quad (2)$$

$$\mu = \frac{m_e m_h}{m_e + m_h}$$

$$\varepsilon_{eff} = \frac{\varepsilon_b L_b + \varepsilon_w L_w}{L_b + L_w} \quad (3)$$

$$E_b = \frac{e^4}{4\pi\varepsilon_0 \varepsilon_{eff} {a_B}^{2D}} \quad , \quad {a_B}^{2D} = \frac{2\pi\varepsilon_0 \varepsilon_{eff} \hbar^2}{\mu e^2} \quad (4)$$

While this covers free excitons, or the unobstructed, direct recombination and subsequent photon emission, other phenomena are also observed, as excitons are trapped by crystal imperfections and

structural defects, placing them in a modified energy landscape. This landscape mimics that of the bulk material and allow the excitons to perform trap mediated recombination, a phenomenon which gives off broad emission peaks of lower energy and a significantly increased exciton lifetime. This phenomenon has a bi-exponential decay rate (Equation (5)), with each characteristic time, τ_1 and τ_2 corresponding to free exciton recombination and trap mediated recombination phenomena, respectively.

$$I = Ae^{-t/\tau_1} + Be^{-t/\tau_2} + I_0 \quad (5)^{[28]}$$

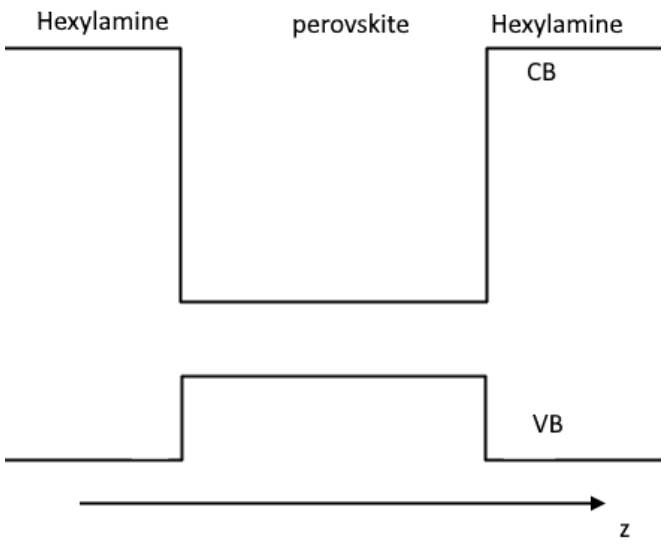

Figure 4: Schematic representation of an energy diagram of the layered perovskite heterostructure quantum well.

The scope of the present Thesis is to synthesize a novel homologous 2D perovskite series based on the bromide anions, so that we can investigate the effect of the reduced dielectric constant of the inorganic layer to the optical properties of the series and determine whether they follow the Wannier[24]- or Frenkel[25]-like excitonic behaviour. The system chosen for the study is the homologous series $(CH_3(CH_2)_5NH_3)_2(CH_3NH_3)_{n-1}Pb_nBr_{3n+1}$ (n = 1-6,. . ., ∞). The homology is constructed by n metal cations (incidentally representing the number of perovskite sheets) and 3n+1 bromide anions (the +1 occurs as a result of the non-bridging bromides along the stacking direction). The organic spacer layer is not affected by the thickness of the inorganic layer and it always requires two equivalents of monovalent cations to form the surfactant bilayer, in the Ruddlesden-Popper structure. The study involves the tuning of the synthetic parameters in order to obtain the materials in pure form. The crystal structures of the compounds were determined via single-crystal X-ray diffraction in different temperatures between 100-400K in order to take into account (examine carefully or altogether avoid) the temperature-dependent phase transitions, which were visible in the calorimetric analysis. All the

compounds were characterized spectroscopically and their optical energy gaps at room temperature were determined via reflectance and emission measurements. We discovered that, the synthesis is very sensitive, mostly to the amount of hexylamine used for the reaction. The products have an energy gap that gets narrower as the number of layers increases, with a decrease in the carrier lifetimes.

RESULTS AND DISCUSSION

Syntheses

The 2D Ruddlesden-Popper layered $(HA)_2(MA)_{n-1}Pb_nBr_{3n+1}$ (n=1-6) perovskite series was pursued using Pb^{2+} and MA^+ as M^{2+} and perovskitizer, respectively. The "spacer" that was used was the monovalent hexylammonium $(HA)^+$ cation, assuming that it can template layers[29-34]. in order to chemically cleave the sheets of the bulk material. Since we were targeting the Ruddlesden-Popper type of perovskites we deliberately chose a univalent cation[35], such as *n*-hexylamine. As the component of lowest solubility in the aqueous medium, hexylamine played the role of the reaction limiting reagent, and because of this the synthetic pathway requires to move the reaction away from its stoichiometric ratios. The rest of the components were added stoichiometrically, except for HBr, which was used in excess (~ 10 fold), in the form of concentrated (~9M) aqueous solution, which also used as the solvent medium. This concept, borrowed from the synthetic approach of the iodide series[11], was experimentally modified to adjust to the different solubility of the reaction component in the HBr medium. We find that when we employ ~ 1/4 of the amount of hexylamine required by stoichiometry we were able to obtain the compounds of the homologous series in pure form, according to equation (6):

$$2\,(CH_3(CH_2)_5NH_3)Br \quad + n - 1\,CH3NH3Br + \; nPbO \quad + 3n + 1\,HBr$$
$$\xrightarrow{HBr_{(aq)}} (CH_3(CH_2)_5NH_3)_2(CH3NH3)n - 1PbnBr_{3n+1_{(s)}}. + n\,H2O \qquad (6):$$

The synthesis reaction for n=1 proceeds smoothly, by successful dissolution of the metal precursor (*PbO*), in the acidic aqueous *HBr* solution, producing a clear solution. This step follows the chemical reaction (Equation (7)):

$$PbO_2 \xrightarrow{HBr_{(aq)}} Pb^{2+}_{(aq)} + 2Br^-_{(aq)} + H_2O_{(l)}. (7)$$

After that, the liquid hexylamine is added in the solution and the following reaction occurs (Equation 8):

$$2(CH_3(CH_2)_5NH_2)_{(l)} \xrightarrow{HBr_{(aq)}} 2(CH_3(CH_2)_5NH_3)^+_{(aq)} + 2Br^-_{(aq)}.(8)$$

The reaction vessel was immediately covered using a glass cover, and the solution was heated to boiling (~120 ºC). At this temperature, using a soda lime glass microscope slide as a cover to maintain the gas-liquid equilibrium, the reaction mixture was left under reflux condition for 10-15 minutes, in order for it to reach a thermodynamic equilibrium. After the reaction deemed to be complete, stirring and heating were discontinued and the reaction was left to cool slowly to ambient temperature, using the glass cover to maintain the equilibrium conditions. Upon cooling, small, white, thin plate-like crystals began to precipitate. The reaction to form this solid is as follows:

$$2(CH_3(CH_2)_5NH_3)^+_{(aq)} + Pb^{2+}_{(aq)} + 4Br^-_{(aq)} \xrightarrow{HBr_{(aq)}} (CH_3(CH_2)_5NH_3)_2PbBr_{4(s)}.(9)$$

The precipitation was complete in ~30min. The resultant precipitate was isolated via suction filtration.

The synthesis reaction for n=2-6 proceeds in a similar fashion, by successful dissolution of the metal precursor (PbO) and the methylammonium salt (CH_3NH_3Cl), in the acidic aqueous HBr solution, producing a clear solution. This step follows the reaction:

$$nPbO_2 \xrightarrow{HBr_{(aq)}} nPb^{2+}_{(aq)} + 2nBr^-_{(aq)} + nH_2O_{(l)}.(10)$$

and

$$(n-1)CH_3NH_3Cl_{(s)} \xrightarrow{HBr_{(aq)}} (n-1)CH_3NH_3{}^+_{(aq)} + (n-1)Cl^-_{(aq)}. (11)$$

After that, the liquid hexylamine is added in the solution and the following reaction occurs:

$$2(CH_3(CH_2)_5NH_2)_{(l)} \xrightarrow{HBr_{(aq)}} 2(CH_3(CH_2)_5NH_3)^+_{(aq)} + 2Br^-_{(aq)}.(12)$$

The reaction vessel was immediately covered using a glass cover, and the solution was heated up to 120ºC. Under the reflux condition, thermal equilibrium is reached in 10-15 minutes. After the reaction deemed to be complete, stirring and heating were discontinued and the reaction was left to cool slowly to ambient temperature, using the glass cover to maintain the equilibrium condition. Upon cooling, small, white, plate-like crystals began to precipitate. The reaction to form this solid is as follows:

$$2(CH_3(CH_2)_5NH_3)^+_{(aq)} + (n-1)CH_3NH_3{}^+_{(aq)} + nPb^{2+}_{(aq)} + (3n+1)Br^-_{(aq)} \xrightarrow[-\Delta]{HBr_{(aq)}}$$

$(CH_3(CH_2)_5NH_3)_2(CH_3NH_3)_{(n-1)}Pb_nBr_{(3n+1)_{(s)}}$.(13)

The excess chloride anions of the previous step are likely not favored over the bromide anions in this equilibrium (we have not been able to detect any traces of Cl from elemental analyses) since the massive excess of bromide ions over chloride drives the reaction towards the bromide product. The precipitation was complete in ~30min in all cases. The resultant precipitate in each case was isolated via suction filtration.

In order to assess the successful outcome of our reaction, we used two standard tools; X-ray diffraction (XRD) for pattern comparison and Energy-Dispersive X-ray Spectroscopy (EDS) for elemental ratio (Pb:Br) analysis EDS spectra collected were collected for different regions of the crystals in order to have a statistically correct average. EDS analysis revealed that the actual composition of all the compounds were very close to the one suggested from the chemical formulae (**Table 1**). Morphologically, the shape of the crystals exhibits an interesting trend, with the facets of the crystals being irregular and generally rounded around the edges of the crystals for n = 1 and n = 2 members, whereas the higher n-members of the $(CH_3(CH_2)_5NH_3)_2(CH_3NH_3)_{n-1}Pb_nBr_{3n+1}$ (n = 3-6) appear to have much sharper crystal edges. **Figure 5**.

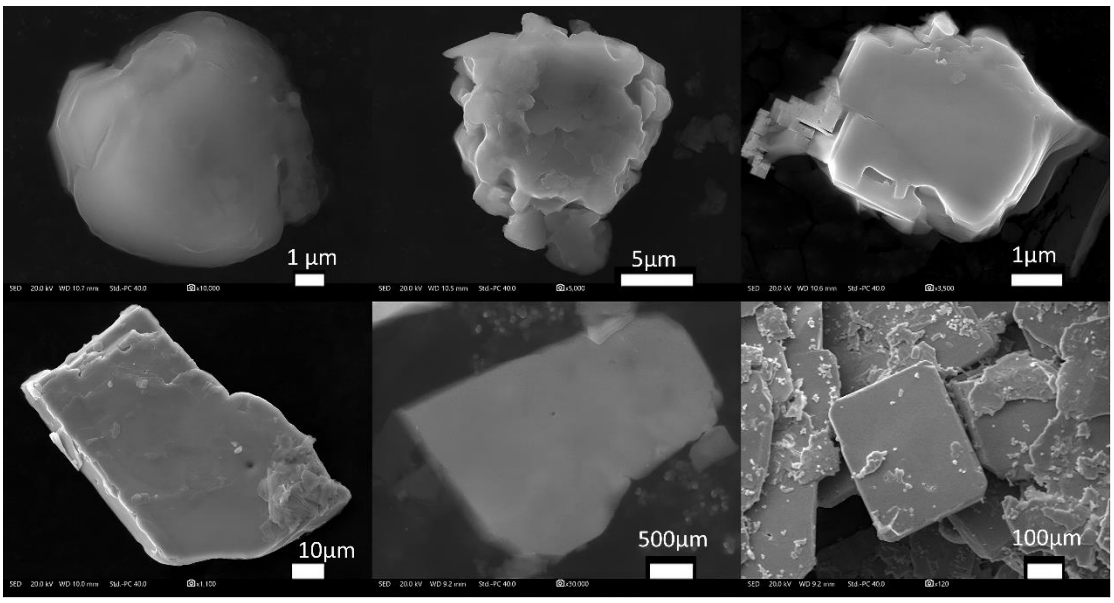

Figure 5: Scanning electron micrographs of crystal samples of $(HA)_2(MA)_{n-1}Pb_nBr_{3n+1}$ for a) n=1, b) n=2, c) n=3, d) n= 4, e) n = 5 and f) n=6, respectively.

Table 1: EDS atomic ratios, normalized as to the equivalents of Pb.

EDS RATIOS	Pb (molar)	Br (molar)	Br theoretical (molar)	Br:Pb ratio	Br:Pb ratio theoretical
Pb_nBr_{3n+1}	-	-	3n+1	-	-
n = 1	1	4.01777	4	4	4
n = 2	2	7.01408	7	3.51	3.5
n = 3	3	8.69811	10	2.9	3.33
n = 4	4	13.14943	13	3.29	3.25
n = 5	5	16.84343	16	3.39	3.2
n = 6	6	19.13324	19	3.19	3.16

All compounds were examined by X-ray powder diffraction (XRD) for the purpose of phase purity and identification **(Figure 6-7)**. All experimental patterns seem to agree with their calculated ones. Comparing the powder patterns for n = 1-6, we observe that all patterns exhibit peaks in different angles. For the n=1, an intense characteristic peak shows up right before 2θ = 5°, with a d-spacing of about 17.0 Å, corresponding to the (002) plane, while there is a weak peak right before 2θ = 10°, with a d-spacing of about 8.5 Å, corresponding to the (004) plane **(Figure 7)**. For n=2, we observe a small shift between the experimental and calculated pattern, with two double like peaks showing up right before 2θ = 4°, with a d-spacing of about 23.4 Å, and 2θ = 12°, with a d-spacing of about 7.8 Å, corresponding to the (002) and (006) planes, respectively. For n=3 we can clearly see three main peaks with the first one (right after 2θ = 3°, with a d-spacing of about 29.4 Å, (020) plane) being weaker compared to the calculated pattern, probably due to preferential orientation. The other two main peaks are not that intense and appear right before 2θ = 6°, with a d-spacing of about 14.7 Å, and 12°, with a d-spacing of about 7.3 Å, corresponding to (040) and (080), respectively. For n=4 we have the two main peaks observed right before 2θ = 3°, with a d-spacing of about 36.2 Å, and 5°, with a d-spacing of about 18.1 Å, corresponding to (200) and (400) planes, respectively, together with two smaller characteristic peaks right after 2θ = 7°, with a d-spacing of about 12.1 Å, and 10°, with a d-spacing of about 9.0 Å, corresponding to (600) and (800) planes, respectively. Also, a single, intense peak at 2θ ~ 12°, with a d-spacing of about 7.2 Å, corresponding to (10 0 0) plane is observed. For the n=5, we observe an intense peak wight after 2θ = 2°, with a d-spacing of about 41.4 Å, and a slightly weaker are around 2θ = 4°, with a d-spacing of about 20.7 Å, corresponding to (020) and (040) planes, respectively. Also, we observe three weak characteristic peaks at around 2θ = 6°, with a d-spacing of about 13.8 Å, 10°, with a d-spacing of about 8.3 Å, and 12°, with a d-spacing of about 6.9 Å, corresponding to (060), (0 10 0) and (160) planes, respectively. For n=6, we observe an intense characteristic peak right before 2θ = 4°, with a d-spacing of about 23.7 Å, corresponding to (400) plane. Also, we observe two main

characteristic peaks right before 2θ = 12°, with a d-spacing of about 7.9 Å, and 14°, with a d-spacing of about 6.8 Å, corresponding to (12 0 0) and (14 0 0) planes, respectively. Due to preferential orientation and the low intensity of some peaks we cannot clearly observe any peaks between 2θ = 4° and 12°, like we do in the calculated pattern of n=6. All samples exhibit a characteristic perovskite peak at about 15°, with a d-spacing of about 17 Å, corresponding to the (111) crystallographic plane, and to the d-spacing between Pb and Br.

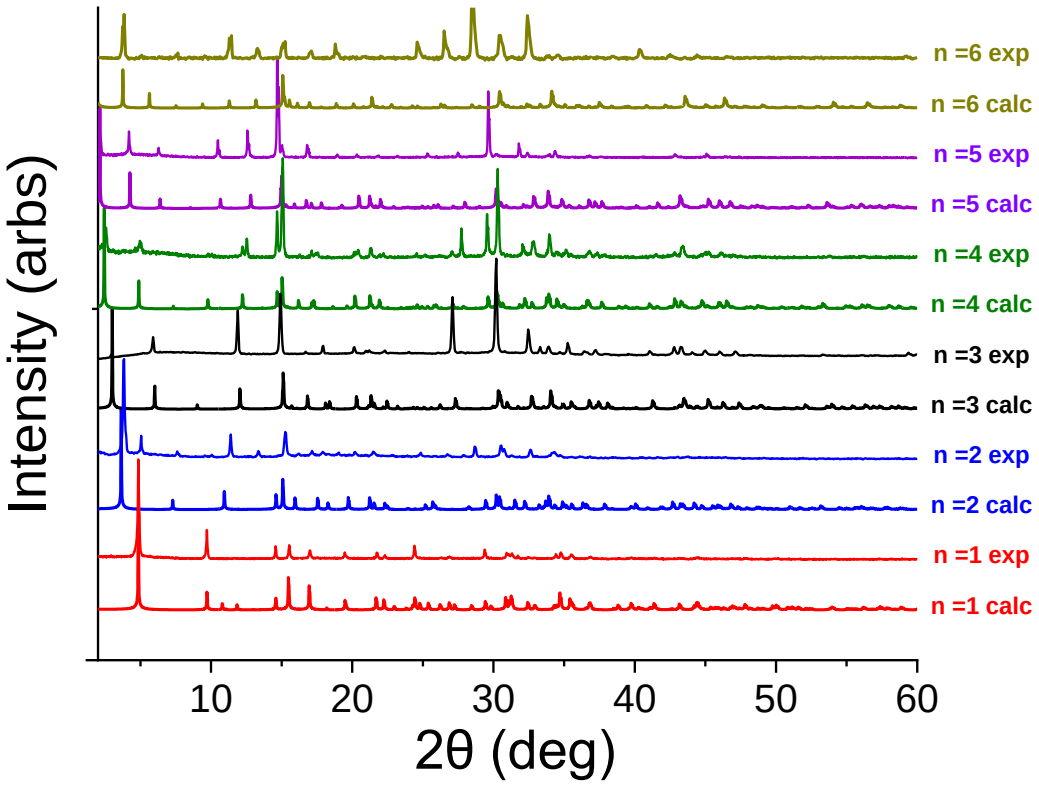

Figure 6: Powder X-ray diffraction (PXRD) patterns of the $(HA)_2(MA)_{n-1}Pb_nBr_{3n+1}$ perovskite series (n=1-6), compared to the calculated ones, produced from the crystallographic data.

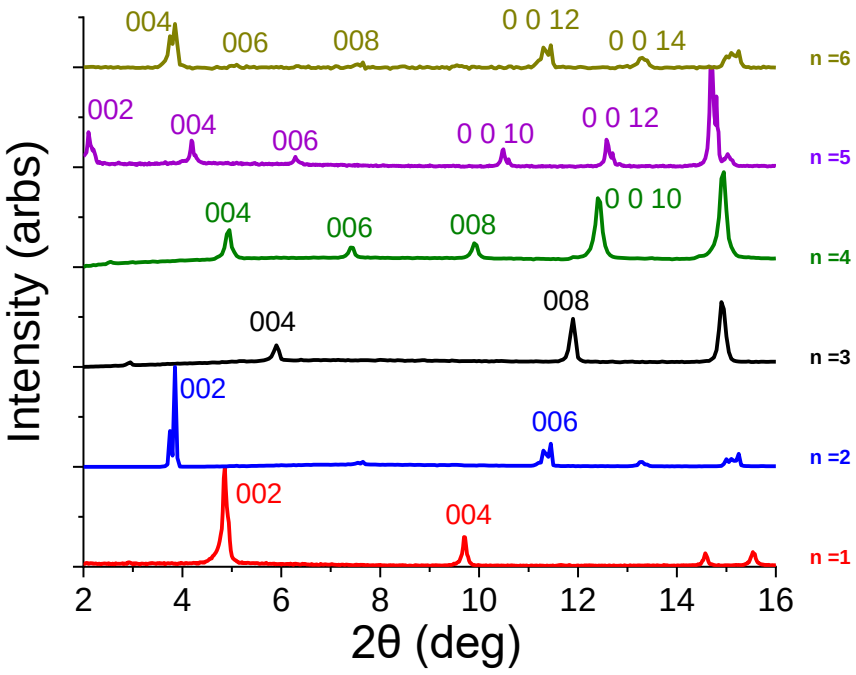

Figure 7: Crystallographic plane analysis for 2θ = 2-16 degrees. The peaks in this region correspond to the number of layers of each $(HA)_2(MA)_{n-1}Pb_nBr_{3n+1}$ compound.

Crystal Structure Description

The crystal structures of the $(HA)_2(MA)_{n-1}Pb_nBr_{3n+1}$ (n = 1-6) compounds comprise of alternating organic-inorganic layers, elongating the crystal lattice along the stacking axis. The inorganic layers consist of layers of regular, corner-sharing $[PbBr_{4/2}Br_2]^{-2}$ octahedra, with the central atom being a bivalent metal (Pb^{+2}) surrounded by six Br^- anions at its apices. Four of the bromine ions are shared along the layer direction, whereas the remaining two, along the stacking axes, serve as terminal ions that form the interface of the layer. For n>1, the methylammonium cations reside in the cavities between the octahedra. The number of octahedral layers coincides as the n number in the formula of the homologous series. The organic layers are formed by self-assembled hexyalammonium bilayers, with the carbon tails interdigitating in the inner part of the bilayer and the positively charged ammonium heads facing outwards, at the surface of the bilayer. This positive charge is attracted to the negative charge of the inorganic layers that flank the organic layers on both sides. For the room temperature structures, two inorganic layers are needed to complete the unit cell, due to symmetry consideration. The high-n compounds (n >3) crystallize in non-centrosymmetric space groups. The compounds with odd number of layers (n = 3 and n = 5) crystalize in the non-centrosymmetric *Aea*2 space group, while the compounds with even number of layers (n = 4 and n = 6) crystalize in the non-centrosymmetric *Cc* space group. The low-n members (n = 1 and n = 2) exhibit a very unusual behavior at room temperature with both of them crystallizing in aperiodic space groups. The n=1 member has an incommensurately modulated structure at room temperature, with a modulation vector of ~ q_1 = 0.15a* + 0b* + 0.4250c*

operating on the monoclinic cell (a = 8.2637(9) Å, b = 8.1942(6) Å, c = 18.047(2) Å β = 103.324(15)°)) to generate the centrosymmetric $P2_1/a(\alpha 0\gamma)00$ 4-dimensional space group. Similarly, n = 2 also crystallizes in an aperiodic structure where the modulation vector $q_1 = 0.56a^* + 0^* - 0.12c^*$ operates on the noncentrosymmeric monoclinic cell with (a = 23.8043(9) Å, b = 8.2975(2) Å, c = 8.360(2) Å, β = 100.025(9)° producing the 4-dimensional $Pc(\alpha 0\gamma)0$ space group (**Table** 2). The modulation vector generates a long-range ripple across the layers with the ripple half period corresponding to ~6 and ~ 8 octahedral units for n = 1 and n = 2, respectively.. Detailed crystallographic data are shown in **Table** 4.

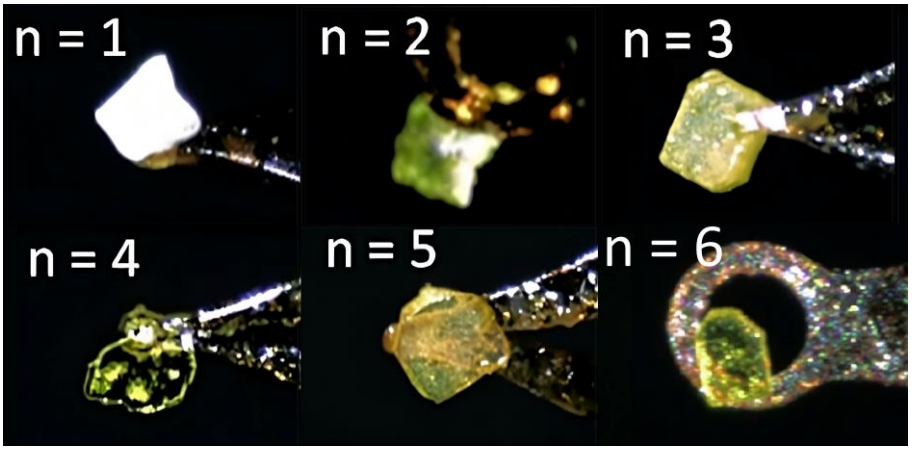

Figure 11. Photographs of the n = 1-6 crystals, mounted on the goniometer for the sc-XRD measurements.

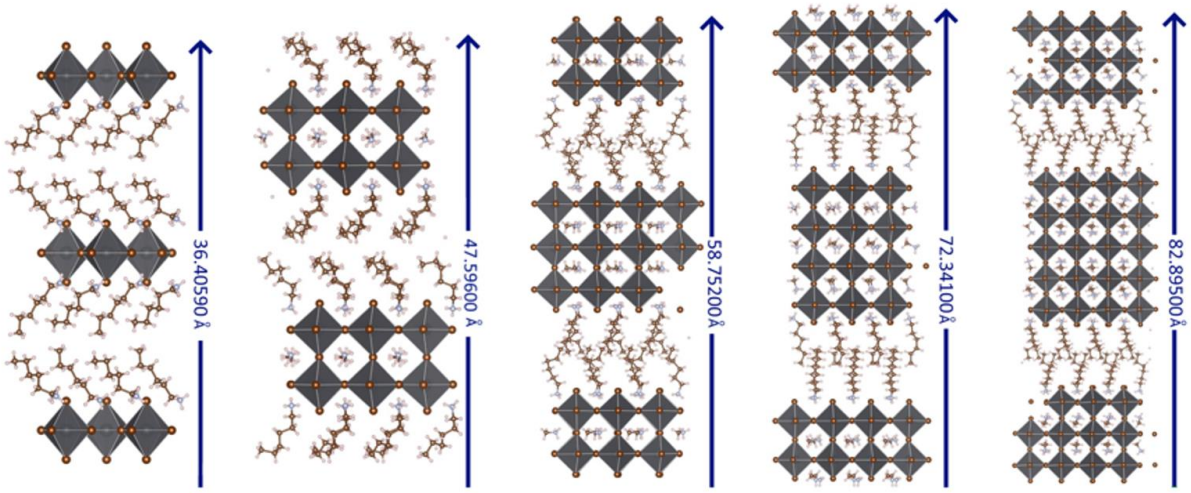

Figure 8: Illustration of all the $(CH_3(CH_2)_5NH_3)_2(CH_3NH_3)_{n-1}Pb_nBr_{3n+1}$ (n = 1-5) homologous series compounds, their respective space groups and display of the elongation of the unit cell at room temperature

The room temperature structures display a progressive elongation of the crystal lattice by ~12 Å per integer increment of n **(Figure 8)**. This corresponds to the extra Pb-Br octahedral layers (2 layers per

unit cell, Pb-Br bond length ~3 Å). The n=1 and n=2 members differ from that pattern, as they exhibit an aperiodic ripple deformation. In the approximant structure (x by x by x supercell), n=1 compound displays a high degree of in-plane tilting of the octahedra along the c and b axes, respectively. In-plane tilting is the inclination of octahedra to rotate along the axis which is perpendicular the layers. The average of the in-plane Pb−Br−Pb angles is 153.60° for n=1. The structures have a progressively lower in-plane tilting, as the number of layers increases, down to 174.9°, as seen in **Table** 2. Bond distance analysis also reveals that, as the number of layers increases, the lengths of the surface Br-Pb bonds are shortened, in relation to the lengths of the inner bonds of the layers in all structures. This doesn't happen for the n=1 member, which has no inner Br-Pb bonds. Both core and interface Pb-Br bonds tend to shorten, as the number of layers increases. This means that the octahedra are more closely packed, as the number of layers increases (or possibly the accuracy of the diffraction pattern decreases with increased n, possibly as a result of twinning and other stacking-fault effects). The bond distances can be seen in detail in **Table 3** and its corresponding bond distance diagrams.

Table 2: In-plane tilting for $(HA)_2(MA)_{n-1}Pb_nBr_{3n+1}$ at 293K.

Compound	$(HA)_2PbBr4$	$(HA)_2(MA)_1Pb_2Br_7$	$(HA)_2(MA)_2Pb_3Br_{10}$	$(HA)_2(MA)_3Pb_4Br_{13}$	$(HA)_2(MA)_4Pb_5Br_{16}$
Octahedral tilting angle (o)	153.59	168.84	170.7	171.78	174.91

Corresponding bond angle diagrams:

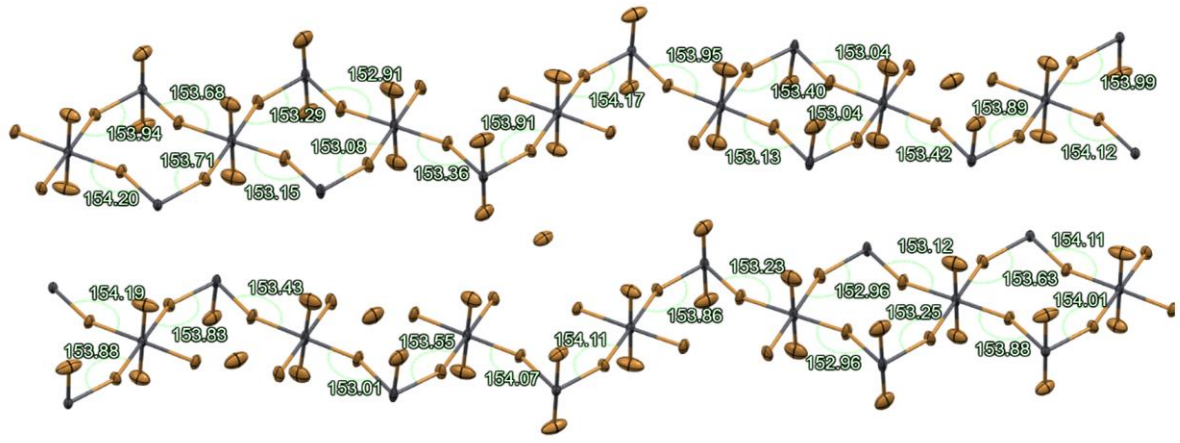

Figure 9: Schematic of the n=1 structure with relevant bond length and bond angle parameters indicated. The thermal ellipsoids have been drawn in 50% probability.

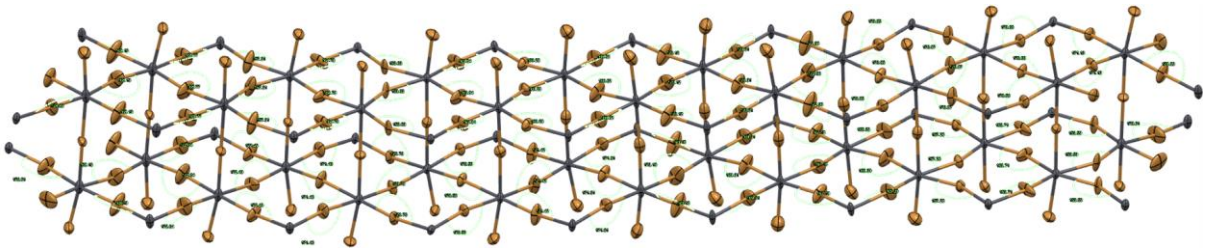

Figure 10: Schematic of the n=2 structure with relevant bond length and bond angle parameters indicated. The thermal ellipsoids have been drawn in 50% probability.

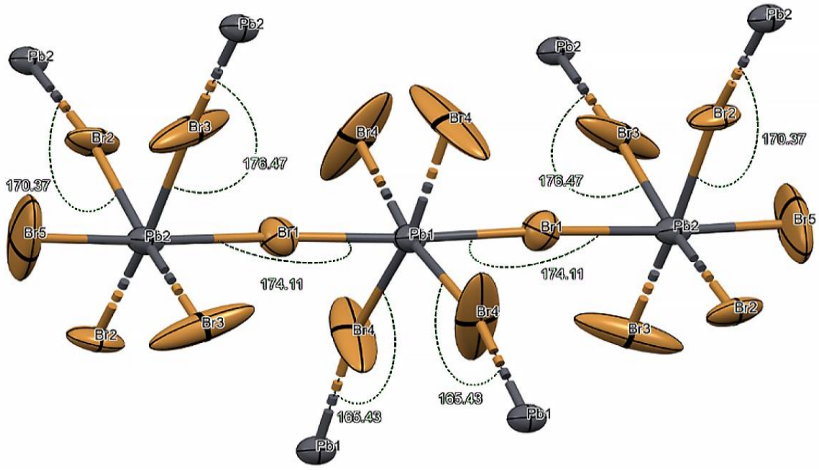

Figure 11: Schematic of the n=3 structure with relevant bond length and bond angle parameters indicated. The thermal ellipsoids have been drawn in 50% probability.

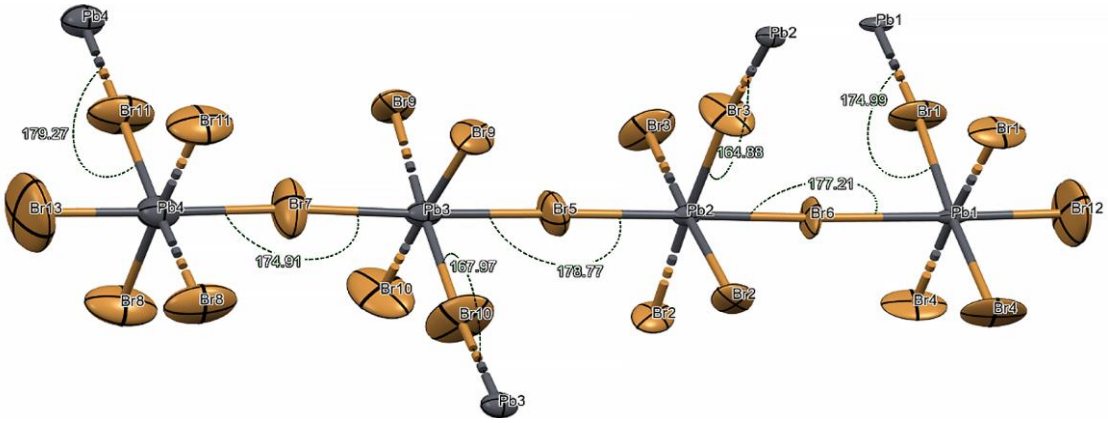

Figure 12: Schematic of the n=4 structure with relevant bond length and bond angle parameters indicated. The thermal ellipsoids have been drawn in 50% probability.

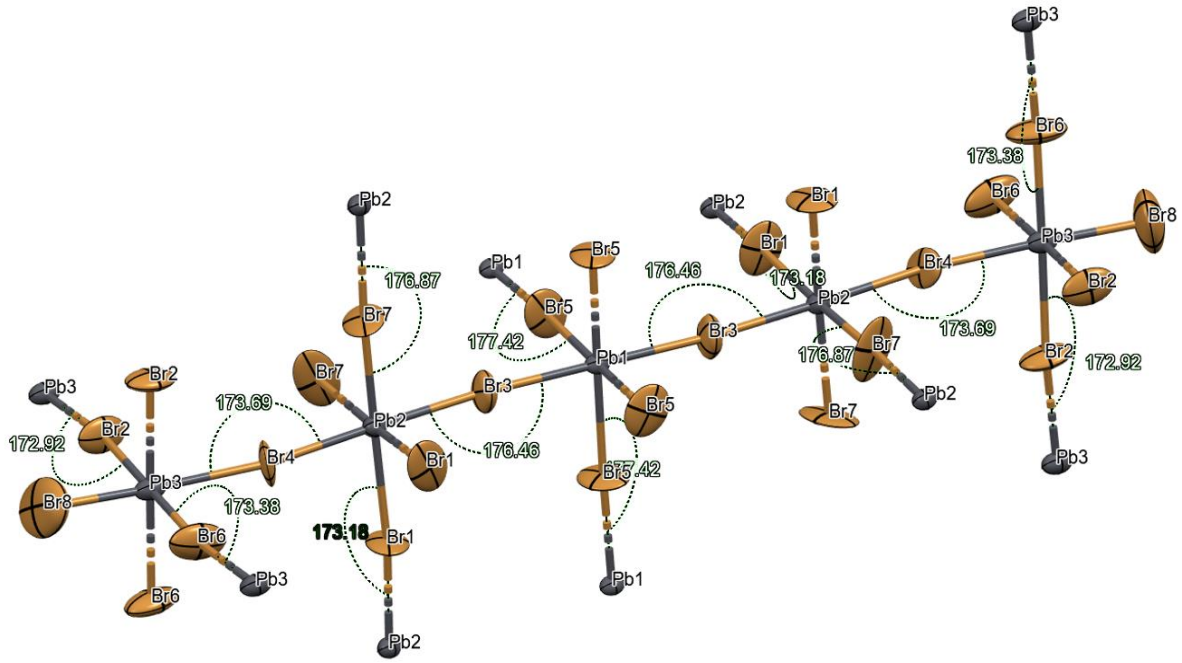

Figure 13: Schematic of the n=5 structure with relevant bond length and bond angle parameters indicated. The thermal ellipsoids have been drawn in 50% probability.

Table 3: Surface bond shortening for $(HA)_2(MA)_{n-1}Pb_nBr_{3n+1}$ 1 at 293K.

Compound	$(HA)_2PbBr_4$	$(HA)_2(MA)_1Pb_2Br_7$	$(HA)_2(MA)_2Pb_3Br_{10}$	$(HA)_2(MA)_3Pb_4Br_{13}$	$(HA)_2(MA)_4Pb_5Br_{16}$
Surface bond length	-	2.888	2.835	2.820	2.779
Average inner bond length	-	3.069	3.063	3.029	2.999

Corresponding bond distance diagrams (n=2-5)

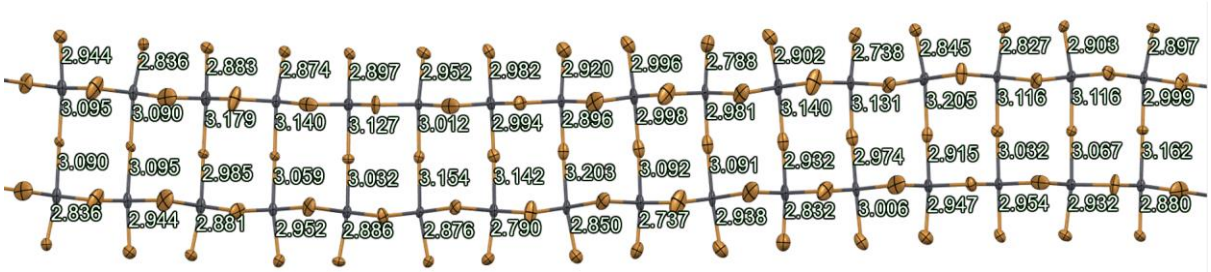

Figure 14: Schematic of the n=2 structure, showing the lengths of the inner and outer bonds that are perpendicular to the layers.

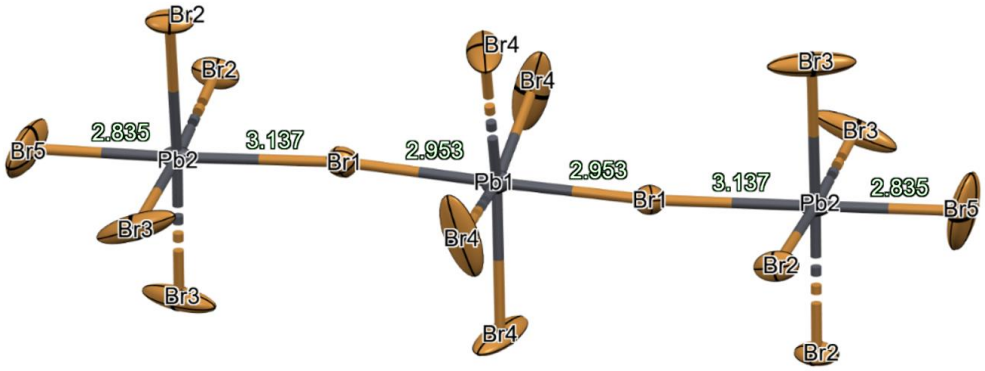

Figure 15: Schematic of the n=3 structure, showing the lengths of the inner and outer bonds that are perpendicular to the layers.

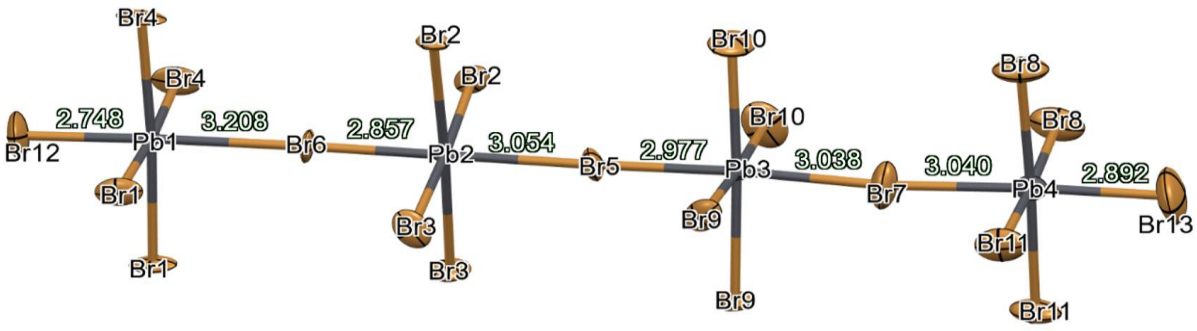

Figure 16: Schematic of the n=4 structure, showing the lengths of the inner and outer bonds that are perpendicular to the layers.

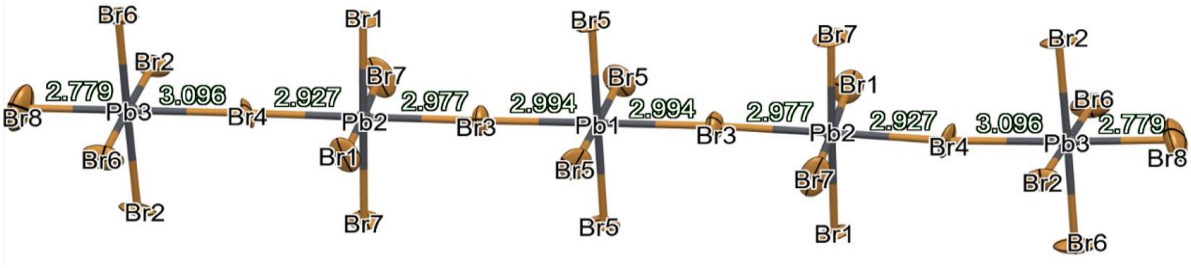

Figure 17: Schematic of the n=5 structure, showing the lengths of the inner and outer bonds that are perpendicular to the layers.

Table 4. Crystallographic Data for $(HA)_2(MA)_{n-1}Pb_nBr_{3n+1}$ at Room Temperature.

Compound	$(HA)_2PbBr_4$	$(HA)_2(MA)_1Pb_2Br_7$	$(HA)_2(MA)_2Pb_3Br_{10}$	$(HA)_2(MA)_3Pb_4Br_{13}$	$(HA)_2(MA)_4Pb_5Br_{16}$
Empirical Formula	Pb Br4 N2 C12 H32	Pb2 Br7 N3 C13 H38	C14 H44 Br10 N4 Pb3	C15 H50 Br13 N5 Pb4	C16 H56 Br16 N6 Pb5
Formula Weight	731.21	1210.18	1689.1	2168.1	2647.1
Temperature (K)	283	293	293	293	293
Wavelength (Å)	0.71073	0.71073	0.71073	0.71073	0.71073
Crystal System	triclinic	monoclinic	orthorhombic	monoclinic	orthorhombic
Space Group	$P2_1/a(a0g)00$	$Pc(\alpha 0\gamma)0$	*Aea*2	*Cc*	*Aea*2
Unit Cell Dimens					
a (Å)	a = 58.2099(5)	a = 23.8043(9)	a = 8.3828(3)	a = 72.3410(2)	a = 8.36460(10)
b (Å)	b = 8.2270(3)	b = 8.2975(2)	b = 60.2406(3)	b = 8.3556(12)	b = 82.8955(12)
c(Å)	c = 35.060(17)	c = 8.360(2)	c = 8.3885(18)	c = 8.3570(2)	c = 8.36420(10)
α (deg)	α = 90.000°	α = 90	α = 90.000(3)	α = 90.0000(14)	α = 90
β (deg)	β = 103.714(8)	β = 100.025(9)	β = 90.000(2)	β = 90.0174(15)	β = 90
γ (deg)	γ = 90.000°	γ = 90	γ = 90.000(3)	γ = 90.0000(15)	γ = 90
q-vector (1)	0.15a* + 0.00b* + 0.43c*	0.56a* + 0.00b* + -0.12c*	-	--	-
V ($Å^3$)	16311.5(11)	1626.0(4)	4236.1(9)	5051.4(7)	5799.63(13)
Z	2	2	4	4	4
Density (g/cm^3)	2.0421	2.4718	2.6486	2.8509	3.0316
Absorption Coefficient (mm^{-1})	13808	18947	21.337	23.59	25.508

F(000)	616	1016	3008	3832	4656
θ Range for Data Collection (deg)	1.78 to 35.25	1.74 to 41.01	2.03 to 33.67	1.69 to 35.5	1.97 to 34.44
Index Ranges	-13<=h<=13 -13<=k<=13 -29<=l<=29 -2<=m<=2	-39<=h<=42 -12<=k<=14 -14<=l<=13 -2<=m<=2	-12<=h<=12 -93<=k<=92 -13<=l<=12	-114≤h≤116 -13≤k≤13 -12≤l≤13	-13≤h≤13 -129≤k≤131 -12≤l≤13
Reflections Collected	291341	566021	80349	136882	153693
Independent Reflections	10716 (4970 main + 19942 satellites) [Rint = 0.1996]	74045 (14809 main + 59236 satellites) [Rint = 0.5597]	3829 [Rint = 0.0879]	9079 [Rint = 0.1132]	5208 [R_{int} = 0.1232]
Completeness to θ = 35.04° (%)	98	98	98	98	98
Refinement Method	Least squares on F^2	Least squares on F^2	Least squares on F	Least squares on F	Least squares on F
Data / Restraints / Parameters	10716 / 36 / 11 / 394	74045 / 15 / 23 / 645	3829 / 12 / 99	9079 / 25 / 208	5208 / 13 / 133
Goodness-of-Fit	1.62	1.21	2.76	3.39	4.71
Final R Indices [I>2σ(I)]	Robs = 0.0641 wRobs = 0.1316	Robs = 0.1355 wRobs = 0.2033	Robs = 0.0851 wRobs = 0.0907	Robs = 0.0870 wRobs = 0.1055	R_{obs} = 0.1043 wR_{obs} = 0.1303
R Indices [all data]	Rall = 0.1448 wRall = 0.1470	Rall = 0.4837 wRall = 0.2925	Rall = 0.1239 wRall = 0.0941	Rall = 0.1079 wRall = 0.1073	R_{all} = 0.1258 wR_{all} = 0.1313
Fourier Difference max and min (e·Å^{-3})	1.86 and -1.33	8.58 and -6.77	3.03 and -1.11	3.96 and -3.22	8.63 and -4.58

The structure for the n=6 member has not been fully probed, so far, so we have only obtained a partial solution. The n=1 and n=2 compounds exhibit structure modulation at room temperature[36, 37]. The single-crystal diffraction patterns, observed exhibit satellite diffraction peaks around the positions of the main diffraction pattern **(Figure 18).** These correspond to a variation of the interatomic distances. First, second and third (only for n =1) order satellites can be observed, as seen in (**Figure 19)**. The satellites are separated from the main reflections by vectors that are integral linear combinations of some basic modulation vectors denoted by q_i (i = 1, 2, 3… d)[38, 39]. Since the modulation is incommensurate, the set of all positions does not form a lattice and at least one q_i is irrational. Here we observe 1st, 2nd and 3rd order satellite reflections that are irrational numbers, corresponding to a displacive modulation, consisting of a periodic displacement from the atomic positions of the basic structure[36, 39, 40]. The result is a ripple effect along the Pb-Br bonds of the structure **(Figure 20)**, with each unit cell including a sine-like wave with maximum and minimum interlayer distances of 12.12 Å and 9.99 Å respectively, for the n=1 compound and 13.01 Å **(Figure 21)**. and 10.05 Å respectively for n=2 **(Figure 22)**. This phenomenon becomes less pronounced for n=2 and is barely discernable for n=3. At the time of this writing, a structure of the n=2 member at room temperature has already been reported, without, however, any modulation effect[41].

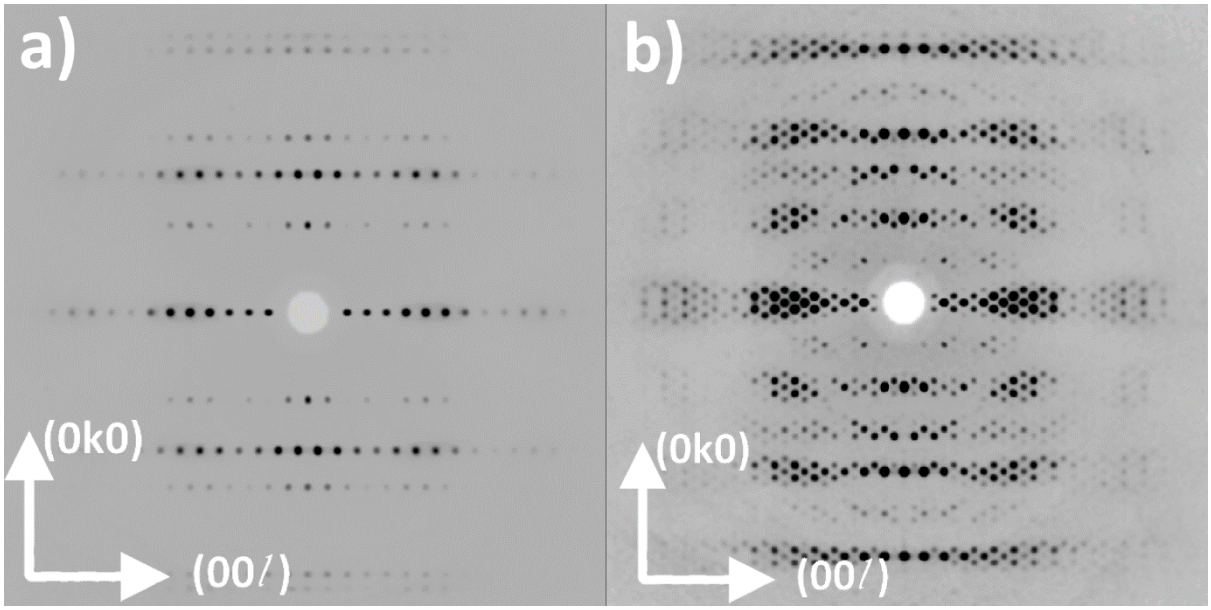

Figure 18: Precession images calculated from scXRD diffraction data in the indicated plane (0kl) pattern for the n=1 compound at: a) 393K and b) 283K, showing the emergence of satellite reflections upon the phase transition.

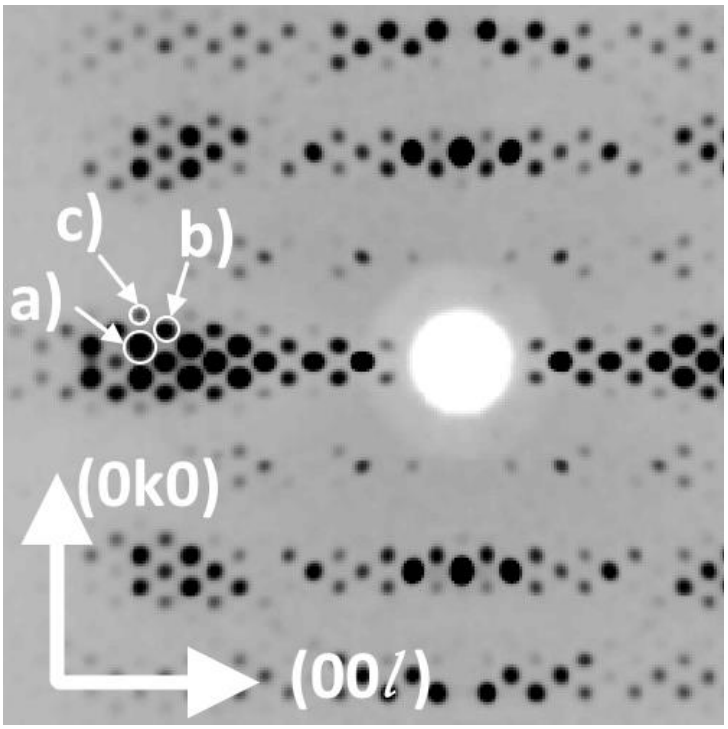

Figure 19: Diffraction patter of a single crystal of the n=1 compound normal the (0kl) plane. The pattern displays satellite reflections of a)1st, b)2nd and c)3rd order.

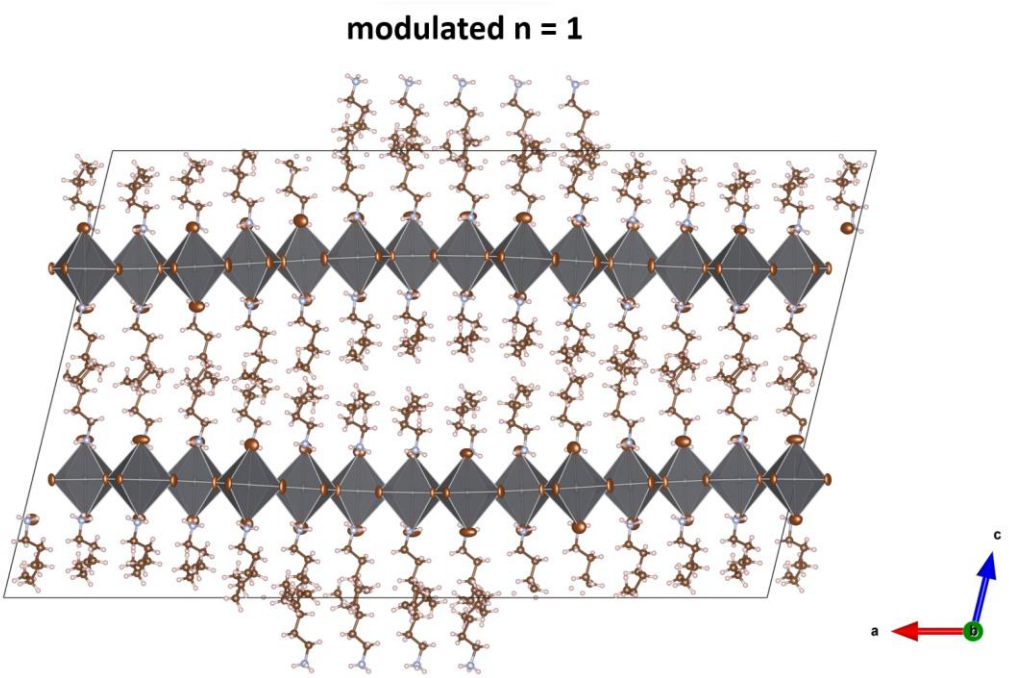

Figure 20: Incommensurately modulated structure of the n=1 member at 283K. The 2 x 1 x 6 supercell shows the approximate structure which exhibits a wave-like deformation of octahedra propagated along the (**a)** axis.

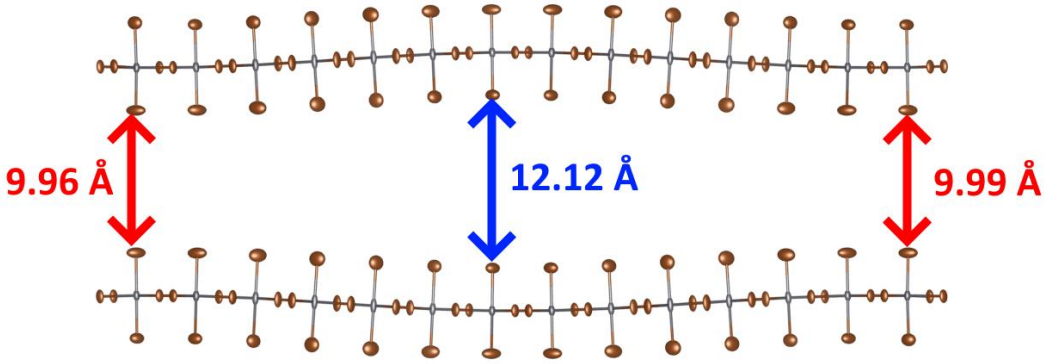

Figure 21: Incommensurately modulated structure of the n=1 member at 283K. The structure ripple has a period of about 14 octahedra, with maximum and minimum interlayer distances of 12.12 Å and 9.99 Å respectively.

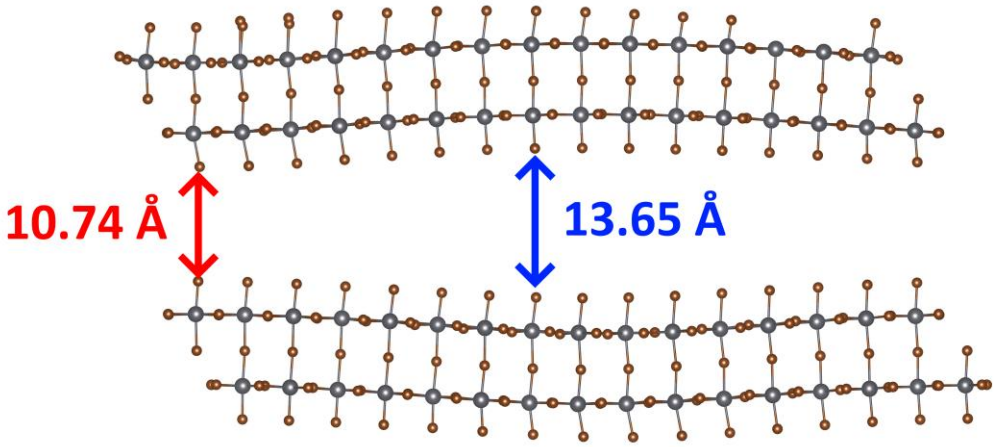

Figure 22: Incommensurately modulated structure of the n=2 member at 293K. The structure ripple has a period of about 18 octahedra, with maximum and minimum interlayer distances of 13.65 Å and 10.74 Å respectively.

Due to the peculiarities of single crystal x-ray diffraction at room temperature, we performed DSC measurements for all compounds **(Figure 23)**, in order to identify possible phase transitions. Indeed, for the n=1 and n=2 members, we observed phase transitions close to room temperature, whereas for n > such transitions appear below room temperature. The transitions are reversible and the origin of such transitions is the change in the crystal structure. For n >2, the compounds exhibit 3 phase transitions, with the first one around 273K and the other transitions appearing between 200-250K. The temperature of the highest symmetry transition observed for the compounds tends to decrease as the number of layers increases. The other transitions appear to follow the opposite trend.

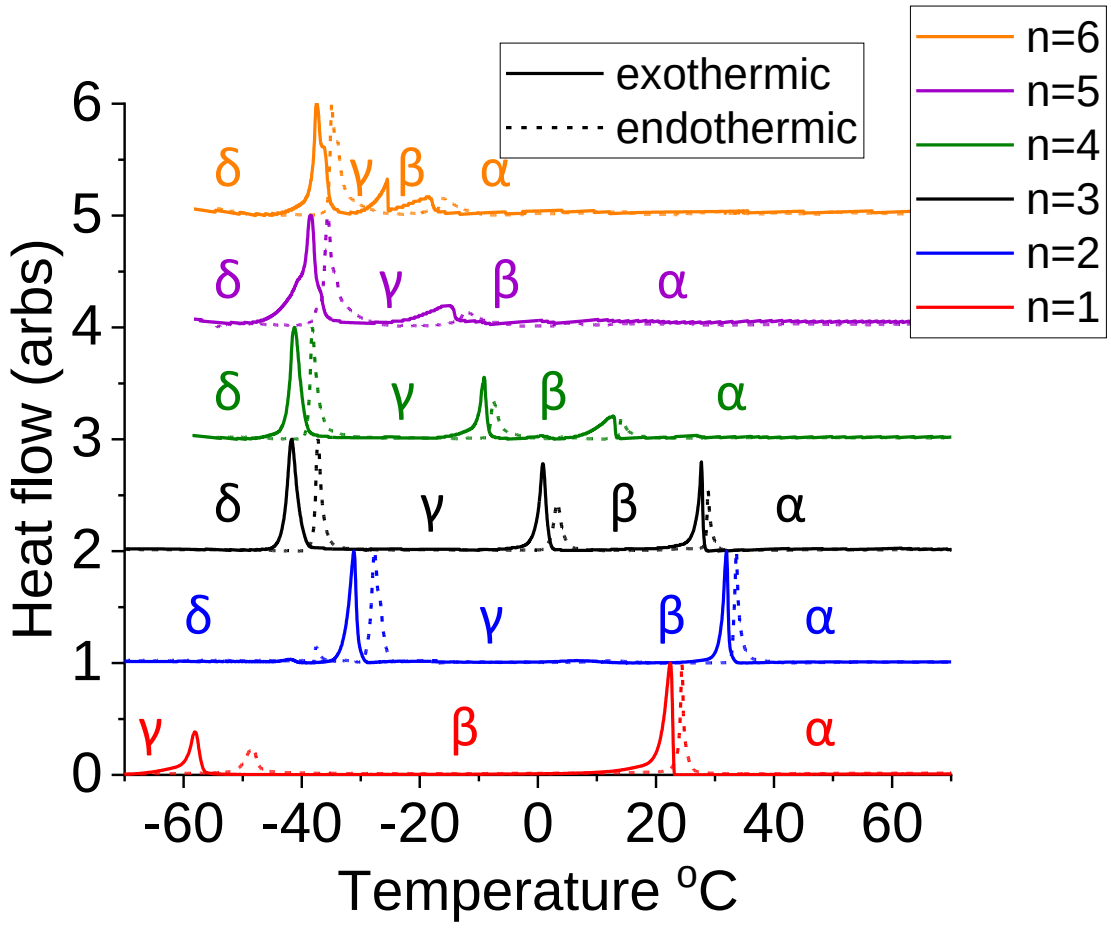

Figure 23: Cumulative DSC diagrams of n=1-6. The exothermic proccesses are depicted by solid lines, while the endothermic ones by dashed lines. For n=1-3, we observe a phase transition at around room temperature. Transitions occur from the highest symmetry, (α-phase), to the lowest symmetry (γ-phase).

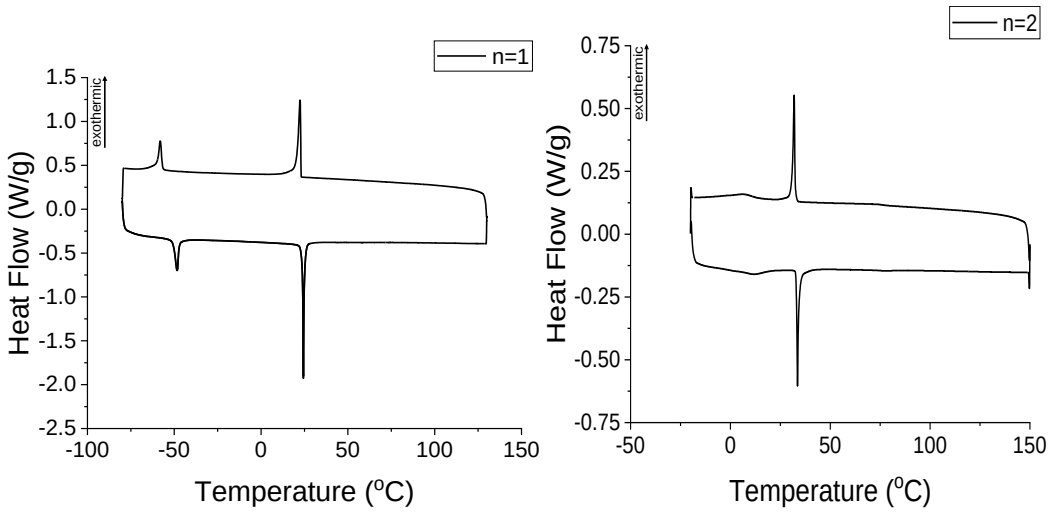

Figure 24: DSC spectra showing the phase transitions at around room temperature for a) n = 1 and b) n = 2

Based on the DSC measurements, we have performed single-crystal diffraction measurements at higher temperature in order to identify the crystal structure of the high temperature phases (α-phases). In order to avoid temperatures close to the critical transitions, we determined their crystal structures at a highest available temperature of 393K. For the high temperature structures, the symmetry indeed changes and for n>2, the size of the unit cell is decreased so that it can accommodate only one inorganic layer per unit cell. The compounds crystalize in non-centrosymmetric space groups. The general trend observed, suggests that the compounds with odd number of layers (n=3 and 5) crystalize in the non-centrosymmetric *Cm* space group, while the compounds with even number of layers (n=2, 4 and 6) crystalize in the non-centrosymmetric *Cc* space group. Note that the *Cm* structures for n > 2 have a true *I*4/*mmm* symmetry, the highest possible symmetry for a 2D perovskite structures [18]. The lowering in symmetry is due to the disordered HA cations which requires a monoclinic symmetry to be modelled in a fixed lattice position. Detailed crystallographic data are shown in **Table 7.**

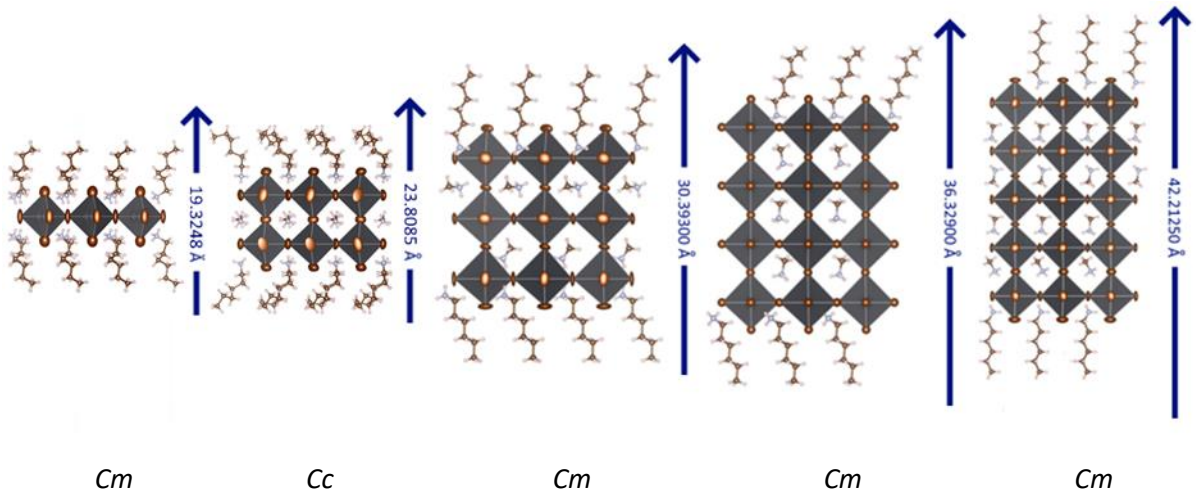

Figure 25: Illustration of all the **$(HA)_2(MA)_{n-1}Pb_nBr_{3n+1}$** (n = 1-5) homologous series compounds, their respective space groups and display of the elongation of the unit at 393K.

The high temperature structures display a progressive elongation of the crystal lattice by about ~6 Å that corresponds to the extra Pb-Br octahedral layers. The n = 1 and n = 2 members differ from that pattern, as their unit cells are distinctively different, incorporating two layers in the unit cell due to symmetry. The structures have a progressively lower in-plane tilting, as the number of layers increases, as shown in **Table 4**. This trend suggests that the α-phase in these systems does not reach the ideal maximal symmetry of the Ruddlesden-Popper phases (*I*4/*mmm* space group) but instead they are 'locked" in a strained monoclinic structure. Bond distance analysis reveals that, as in the case of the room temperature structures, the interfacial Br-Pb bonds at the edges of the layer are shortened, in relation to the lengths of the inner bonds of the layers in all structures, except for the n=1 member, which has no inner Br-Pb bonds. Both inner and interface bonds tend to shorten, as the number of layers

increases. This means that the octahedra are more densely packed, as the number of layers increases. The bond distances can be seen in detail in **Table 5** and **Figures 31-34**.

Table 5: In-plane tilting for $(HA)_2(MA)_{n-1}Pb_nBr_{3n+1}$ at 393K.

	$(HA)_2PbBr_4$	$(HA)_2(MA)_1Pb_2Br_7$	$(HA)_2(MA)_2Pb_3Br_{10}$	$(HA)_2(MA)_3Pb_4Br_{13}$	$(HA)_2(MA)_4Pb_5Br_{16}$
Octahedral tilting angle (o)	154.02	174.37	176.60	179.28	174.50

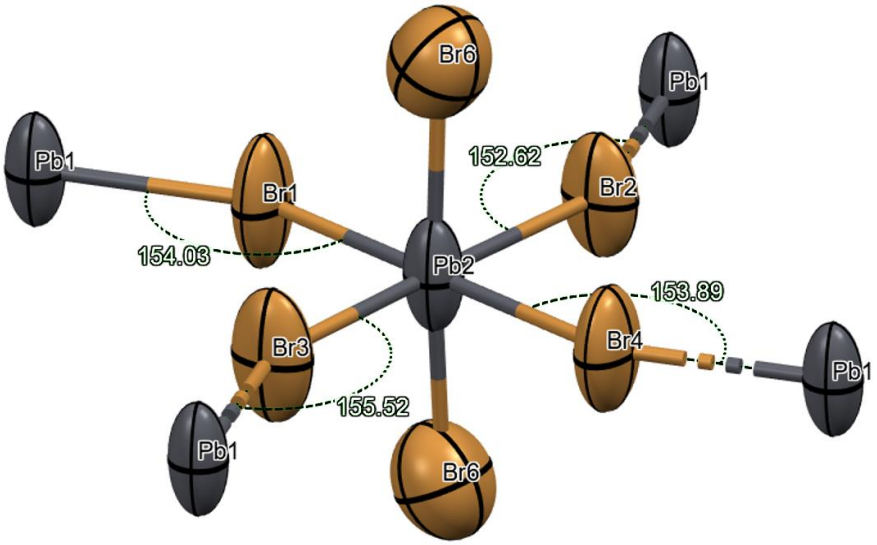

Figure 26: Schematic representation of the building unit of the n=1 structure with relevant bond length and bond angle parameters indicated. The thermal ellipsoids have been drawn in 50% probability.

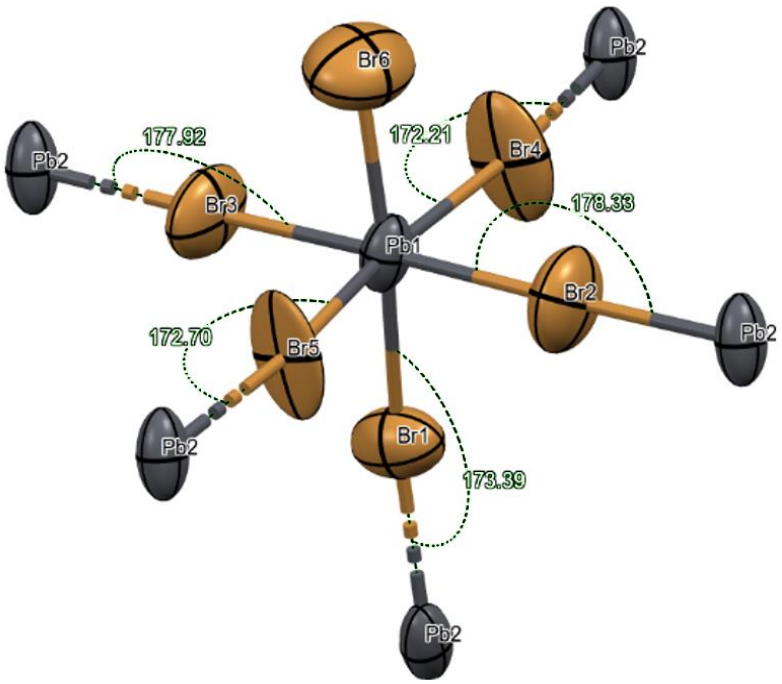

Figure 27: Schematic representation of the building unit of the n =2 structure with relevant bond length and bond angle parameters indicated. The thermal ellipsoids have been drawn in 50% probability.

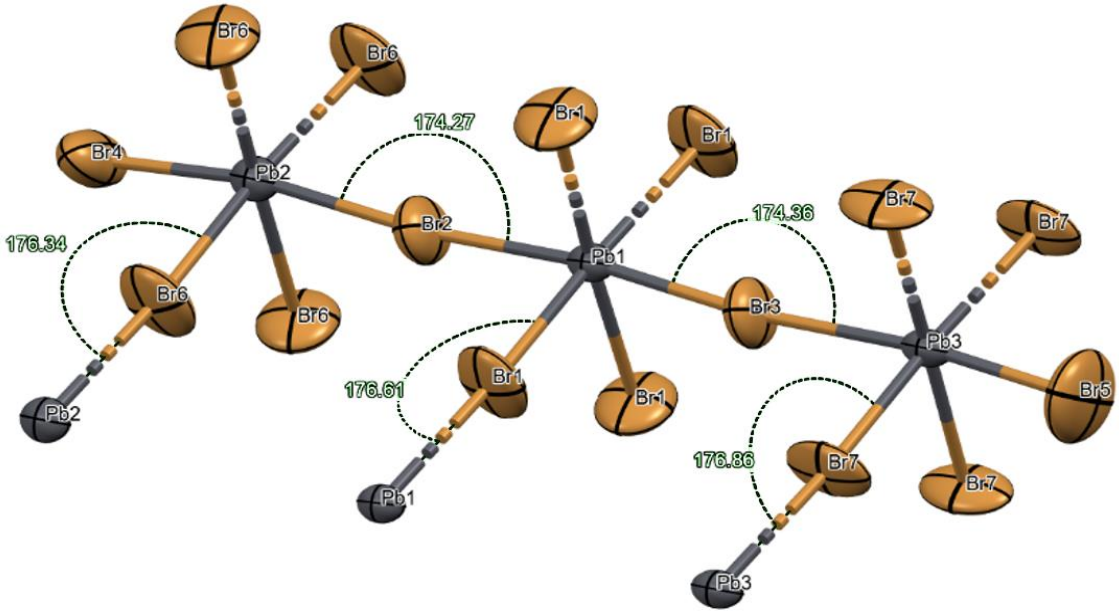

Figure 28: Schematic representation of the building unit of the n =3 structure with relevant bond length and bond angle parameters indicated. The thermal ellipsoids have been drawn in 50% probability.

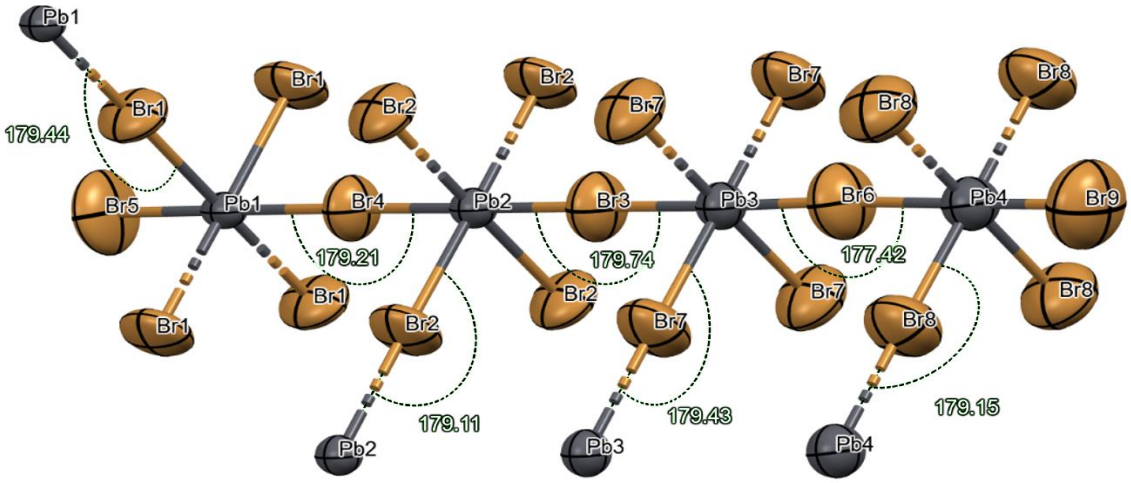

Figure 29: Schematic representation of the building unit of the n =4 structure with relevant bond length and bond angle parameters indicated. The thermal ellipsoids have been drawn in 50% probability.

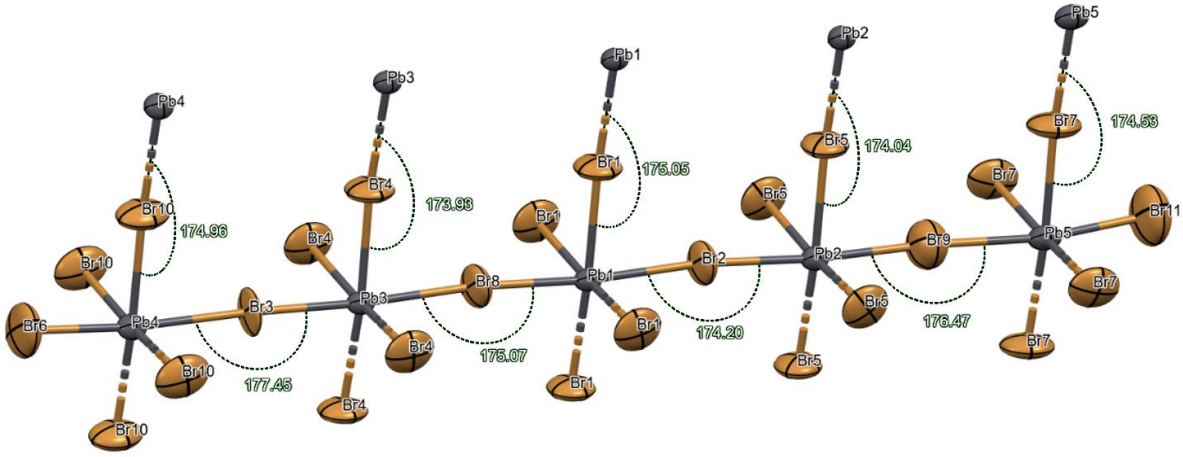

Figure 30: Schematic representation of the building unit of the n =5 structure with relevant bond length and bond angle parameters indicated. The thermal ellipsoids have been drawn in 50% probability.

Table 6:Surface bond shortening for $(HA)_2(MA)_{n-1}Pb_nBr_{3n+1}$ at 293K.

	$(HA)_2PbBr4$	$(HA)_2(MA)_1Pb_2Br_7$	$(HA)_2(MA)_2Pb_3Br_{10}$	$(HA)_2(MA)_3Pb_4Br_{13}$	$(HA)_2(MA)_4Pb_5Br_{16}$
Surface bond length	-	2.861	2.894	2.833	2.837
Average inner bond length	-	3.075	3.035	3.017	3.009

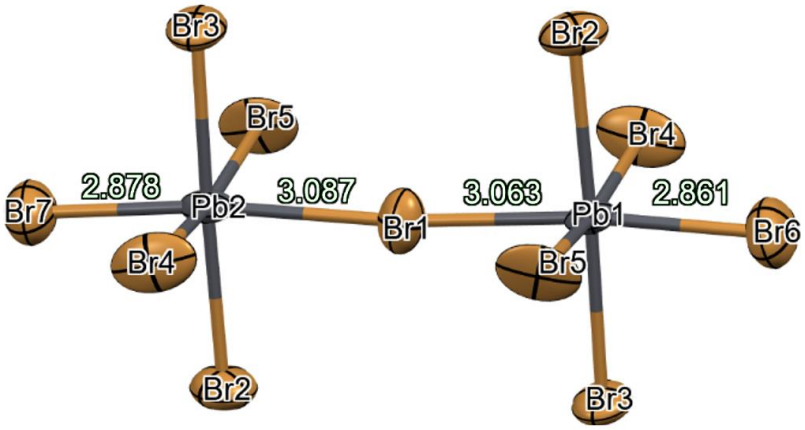

Figure 31: Schematic of the n=2 structure, showing the lengths of the inner and outer bonds that are perpendicular to the layers.

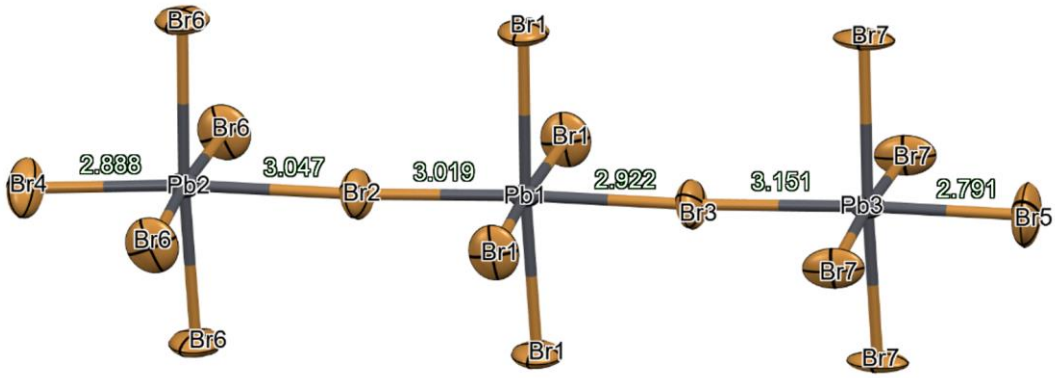

Figure 32: Schematic of the n=3 structure, showing the lengths of the inner and outer bonds that are perpendicular to the layers.

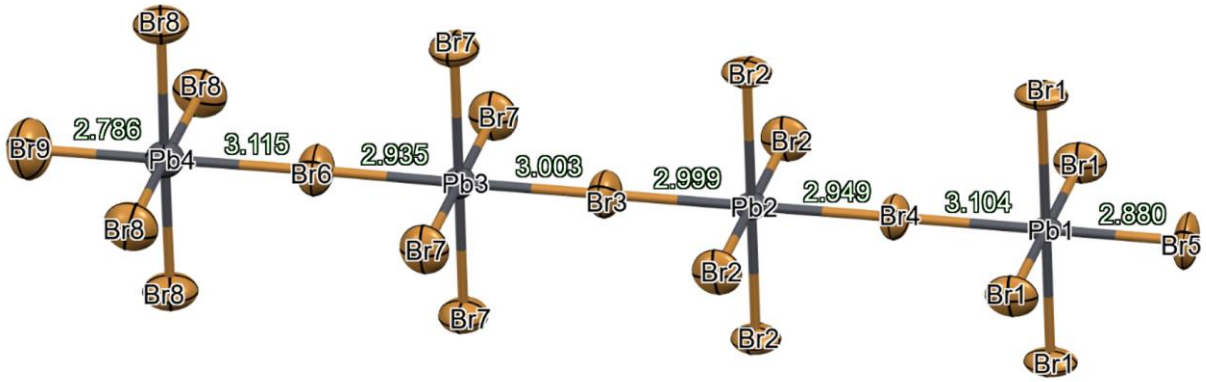

Figure 33: Schematic of the n=4 structure, showing the lengths of the inner and outer bonds that are perpendicular to the layers.

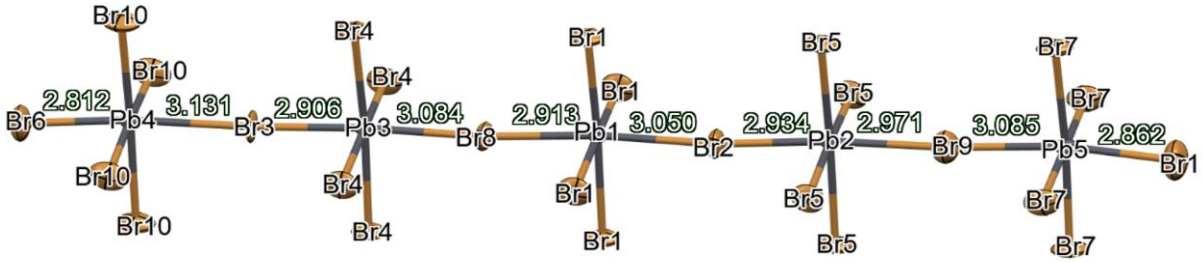

Figure 34: Schematic of the n=5 structure, showing the lengths of the inner and outer bonds that are perpendicular to the layers.

Table 7. Crystallographic Data for $(HA)_2(MA)_{n-1}Pb_nBr_{3n+1}$ at 393K.

Compound	$(HA)_2PbBr_4$	$(HA)_2(MA)_1Pb_2Br_7$	$(HA)_2(MA)_2Pb_3Br_{10}$	$(HA)_2(MA)_3Pb_4Br_{13}$	$(HA)_2(MA)_4Pb_5Br_{16}$
Empirical Formula	Pb Br4 N2 C12 H32	Pb2 Br7 N3 C13 H38	C14 H44 Br10 N4 Pb3	C15 H50 Br13 N5 Pb4	C16 H56 Br16 N6 Pb5
Formula Weight	731.2	1210.2	1689.1	2168.1	2647.1
Temperature (K)	393	393	393	293	293
Wavelength (Å)	0.71073	0.71073	0.71073	0.71073	0.71073
Crystal System	monoclinic	monoclinic	monoclinic	monoclinic	monoclinic
Space Group	*Cm*	*Cc*	*Cm*	*Cm*	*Cm*
Unit Cell Dimens					
a (Å)	a = 8.2172(3)	a = 8.3650(2)	a = 8.3958(6)	a = 8.4039(6)	a = 8.4025(2)
b (Å)	b = 37.7660(15)	b = 48.502(2)	b = 8.3958(6)	b = 8.4008(5)	b = 8.40020(10)
c(Å)	c = 8.2176(3)	c = 8.3641(2)	c = 30.393(6)	c = 36.329(2)	c = 42.2125(8)
α (deg)	α = 90	α = 90	α = 90	α = 90.000(5)	α = 90.0000(13)
β (deg)	β = 90.009	β = 90.0000(19)	β = 97.9391	β = 96.593(5)	β = 95.6702(16)
γ (deg)	γ = 90	γ = 90	γ = 90	γ = 90.000(5)	γ = 90.0000(14)
V ($Å^3$)	2550.17(17)	3393.48(18)	2121.9(5)	2547.8(3)	2964.89(10)

Z	4	4	2	2	2
Density (g/cm^3)	1.9045	2.3687	2.6438	2.8261	2.9651
Absorption Coefficient (mm^{-1})	12.877	18.156	21.299	23.385	24.948
F(000)	1360	2184	1504	1916	2328
Crystal Size (mm^3)	? x ? x ?	? x ? x ?	? x ? x ?	? x ? x ?	? x ? x ?
θ Range for Data Collection (deg)	2.16 to 34.94	1.68 to 34.47	2.71 to 30.52	1.69 to 34.94	1.94 to 34.45
Index Ranges	-12≤h≤13 -60≤k≤60 -13≤l≤12	-12≤h≤11 -76≤k≤77 -13≤l≤13	-11≤h≤11 -11≤k≤11 -43≤l≤43	-13≤h≤13 -13≤k≤13 -57≤l≤57	-13≤h≤13 -13≤k≤12 -66≤l≤66
Reflections Collected	64881	85289	38752	50580	81783
Independent Reflections	4507 [R_{int} = 0.1016]	5984 [R_{int} = 0.1727]	12235 [R_{int} = 0.0683]	4901 [R_{int} = 0.0675]	5730 [R_{int} = 0.0919]
Completeness to θ = 35.04° (%)	98	98	100	98	98
Refinement Method	F	F	F	F	F
Data / Restraints / Parameters	4507 / 22 / 99	5984 / 23 / 136	12235 / 24 / 113	4901 / 25 / 131	5730 / 38 / 112
Goodness-of-Fit	1.54	1.44	1.20	2.03	5.00
Final R Indices [I>2σ(I)]	R_{obs} = 0.0454 wR_{obs} = 0.0896	R_{obs} = 0.0821 wR_{obs} = 0.1271	R_{obs} = 0.0480 wR_{obs} = 0.1035	R_{obs} = 0.0834 wR_{obs} = 0.0867	R_{obs} = 0.0754 wR_{obs} = 0.1210
R Indices [all data]	R_{all} = 0.0968 wR_{all} = 0.0988	R_{all} = 0.1506 wR_{all} = 0.1461	R_{all} = 0.0987 wR_{all} = 0.1219	R_{all} = 0.1071 wR_{all} = 0.0891	R_{all} = 0.0832 wR_{all} = 0.1215
Fourier Difference max and min (e·Å^{-3})	1.75 and -1.01	4.97 and -3.36	2.36 and -2.42	2.16 and -1.28	2.94 and -3.28

Optical Properties

In order to estimate the band gap of the new compounds and determine whether they emit in the visible spectrum, we performed diffuse reflectance measurements between 185-1400nm (UV-vis-NIR spectroscopy) and photoluminescence spectroscopy (PL) close to the estimated absorption edges. The results are tabulated in **Table 8** and the spectra are summarized in **Figures 35**.

Table 8: Optical Properties and Color of the $(HA)_2(MA)_{n-1}Pb_nBr_{3n+1}$.

	Compounds	Absorption edge E_g (eV)	Photoluminescence PL (eV)	(E_g-PL) (meV)	Color
n=1	$(HA)_2PbBr_4$	2.99	2.98	10	White
n=2	$(HA)_2(MA)Pb_2Br_7$	2.77	2.83	60	Pale yellow
n=3	$(HA)_2(MA)_2Pb_3Br_{10}$	2.59	2.70	110	Yellow
n=4	$(HA)_2(MA)_3Pb_4Br_{13}$	2.44	2.59	150	Dark yellow
n=5	$(HA)_2(MA)_4Pb_5Br_{16}$	2.28	2.50	220	Light orange
n=6	$(HA)_2(MA)_5Pb_6Br_{19}$	2.23	2.45	220	Orange

The photoluminescence properties of all the homologous series compounds were obtained at room temperature, as shown in **Figure 36**, and measured at room temperature using a laser excitation of λ_{exc} = 532 nm in a custom-made PL spectrometer. The photoluminescence emission energy of all the 2D halide perovskites described here decreases with increasing layer thickness similar to the optical band gap trend (**Table 8**). The photoluminescence spectra consist of one single emission peak for each of the compounds corresponding to the kink observed in the absorption spectra. The compounds emit between 400 and 550 nm. A sharp PL emission was observed for all of the compounds except for n=1 (λ_{em} = 416nm), at λ_{em} =438nm, λ_{em} =459nm, λ_{em} =479nm and λ_{em} =496nm, for n=2-5, respectively. The emission wavelength is consistent with the experimentally determined band gaps providing further evidence for the direct nature of the band gap. order to confirm the semiconducting nature of the materials, optical diffuse reflectance measurements were carried out **(Figure 35**), revealing the presence of sharp optical gaps. The Absorption spectra were obtained by the Kubelka-Munk transformations ($\alpha/S = (1 - R)2 /2R$)[42, 43] of the reflectivity spectra, to better ascertain the energy of the band gaps, by the linear fitting of the lowest energy transition of each spectrum. The compounds exhibit two curves, with the first one probably corresponding to the free exciton energy[44]. The bandgap, E_g, of the n compounds can be assessed at 2.99 eV, 2.77 eV, 2.59 eV, 2.44 eV, 2.28 eV and 2.25eV, for n=1-6, respectively. The sharp nature of the absorption edges points toward a direct band gap in all compounds and it it consistent with the observed color of the solids

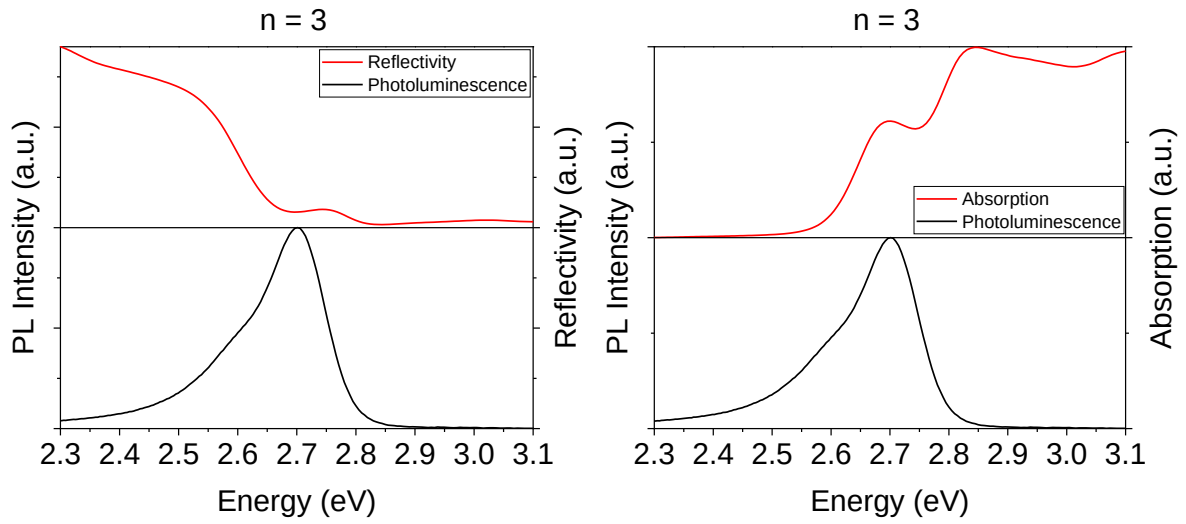

Figure 35: Comparison of the photoluminescence, diffuse reflectance and absorption spectra for the n=3 member.

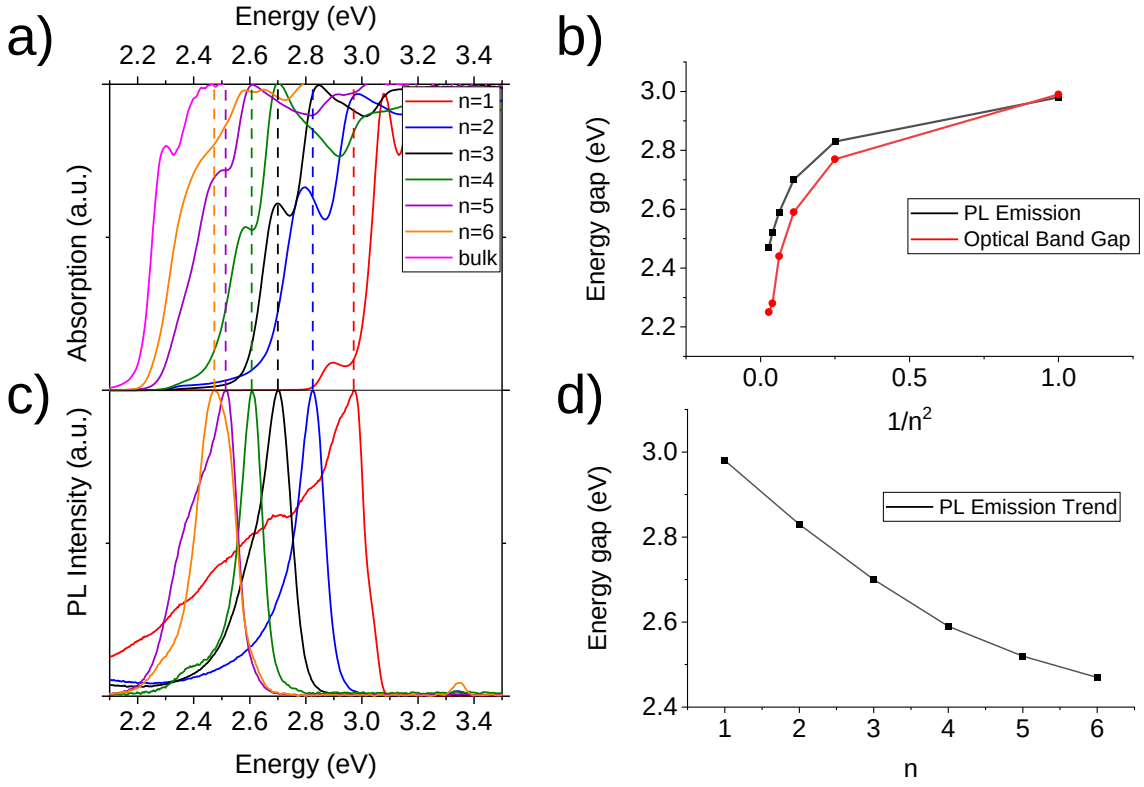

Figure 36: Optical properties of the $\mathbf{(HA)_2(MA)_{n-1}Pb_nBr_{3n+1}}$perovskites (for n = 1-6). a) Optical absorption of the compounds were obtained from diffuse reflectance measurements converted using the

Kubelka−Munk function ($\alpha/S = (1 - R)^2/2R$)[42, 43]. b) Photoluminescence spectra of n=1-6. c) PL emission energy versus layer thickness (n). d) Plot of the band gap and photoluminescence versus layer thickness with the latter expressed in the form of $1/n^2$. Note that in panels a, b the energy is plotted in a reciprocal scale and the wavelength in a linear scale.

In an attempt to estimate the exciton recombination lifetime, the samples were subjected to time-resolved photoluminescence measurements in a Time Correlated Single Photon Counting (TCSPC) setup using a low power laser.

All samples exhibit a biexponential decay rate, with the characteristic times shown in **Figure 37**. And were fitted according to equation (d), as mentioned in the introduction.

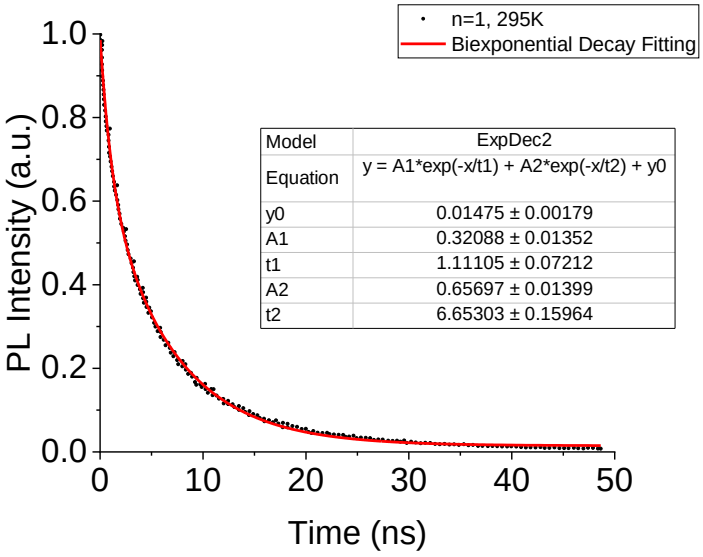

Figure 37: Biexponential fitting of the time-resolved photoluminescence spectrum for n=1, showing the equation used for the fitting, as well as the resulting carrier lifetimes.

The PL lifetimes for n=1 fall in a range of 40-50 ns, while for n=6 the range in all these different temperatures was 0-1.6 ns. The PL lifetimes get longer, as the number of layers increases, which is an indication of slower carrier recombination and improved carrier transport in crystals with lower numbers of layers. The trend can be seen in **Figure 39**. As hinted to in the introduction, the short lifetimes correspond to free exciton recombination, representing the ideal case. The longer lifetimes correspond to trap-mediated recombination, which slows the phenomenon down considerably. This can be seen in **Figure 41**, and a detailed catalogue including all lifetimes for all member measured can be seen in **Table 9**.

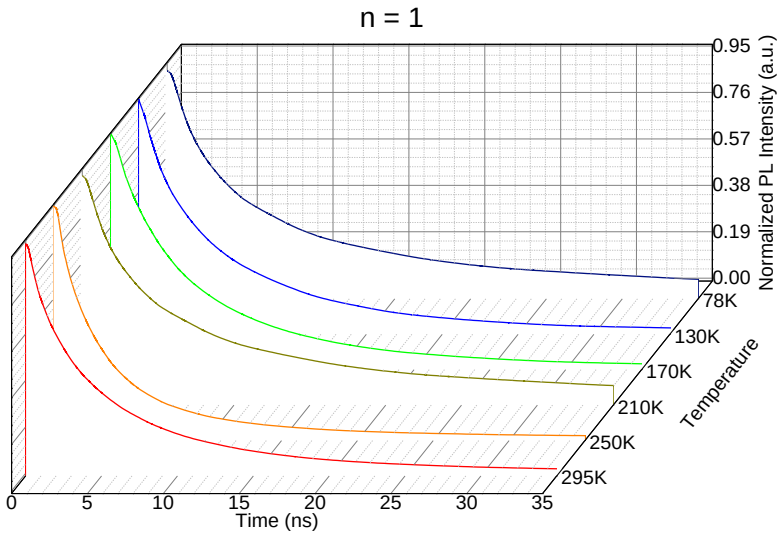

Figure 38: Time and temperature-resolved PL measurements for n=1. This sample exhibits long-lasting PL emission, that becomes more short-lived, as the number of layers increases.

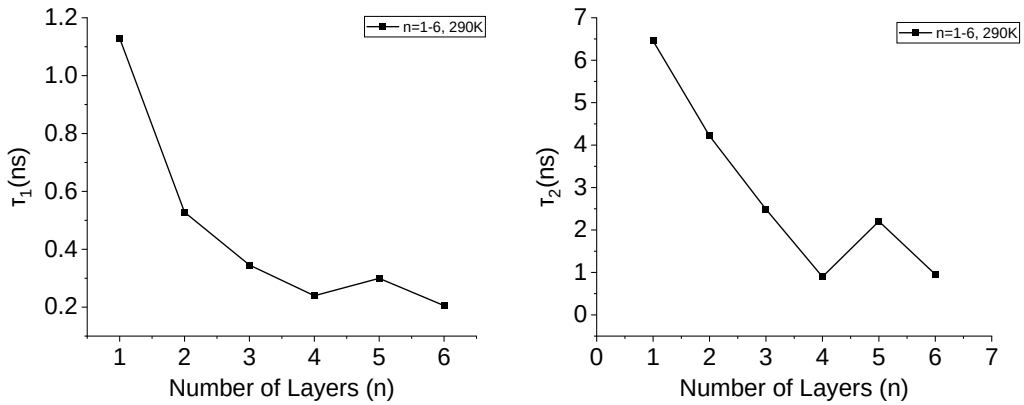

Figure 39: τ_1 (short) and τ_2 (long) photoemission lifetimes at 290K, as calculated by biexponential decay fitting.

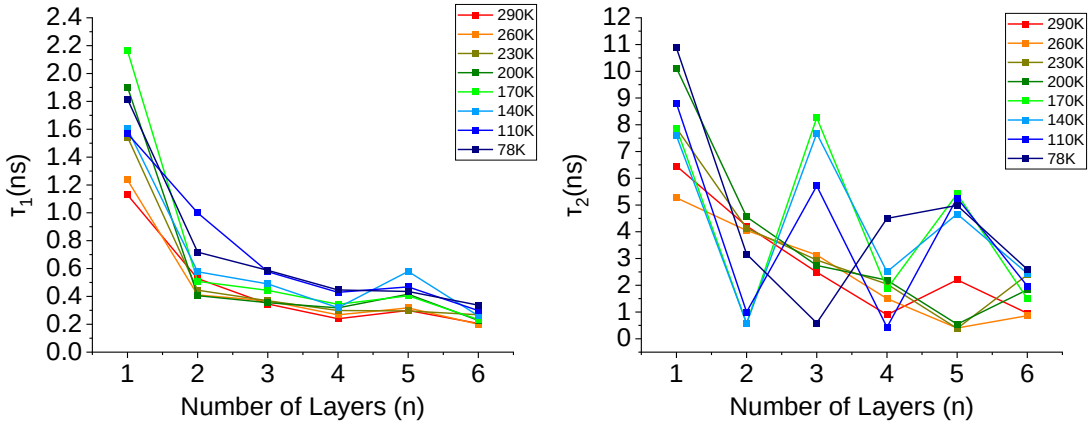

Figure 40: τ_1 (short) and τ_2 (long) photoemission lifetimes at all measurement temperatures, as calculated by biexponential decay fitting. There appears to be a trend to reduce τ1 as the temperature and the number of layers increase. The trend is not as clear for τ2.

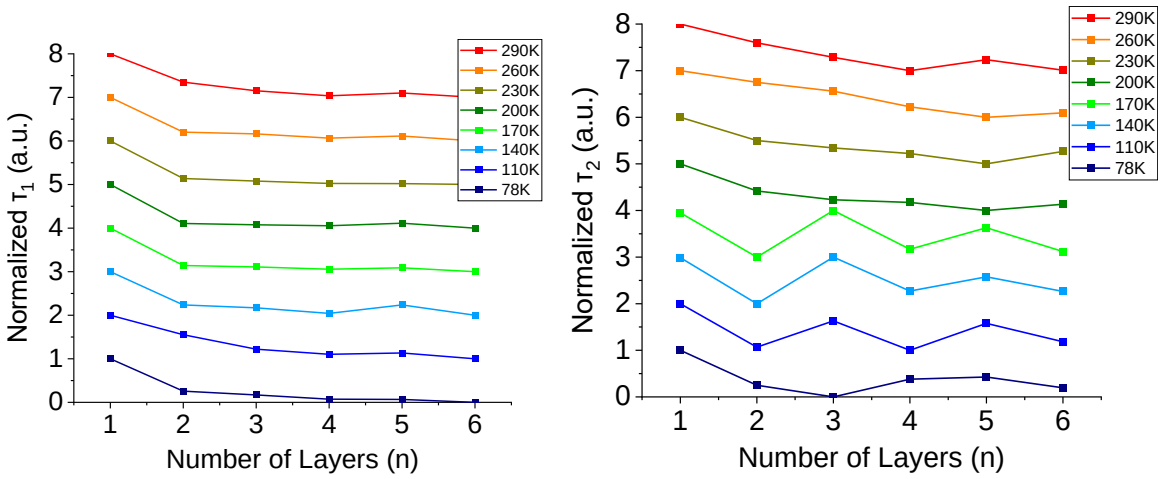

Figure 41: Normalized τ_1 (short) and τ_2 (long) photoemission lifetimes at all measurement temperatures, as calculated by biexponential decay fitting. There appears to be a trend to reduce τ1 as the temperature and the number of layers increase. The trend is not as clear for τ2.

Table 9: τ1 (short) and τ2 (long) photoemission lifetimes at all measurement temperatures, as calculated by biexponential decay fitting of the original data.

	n=1		n=2		n=3		n=4		n=5		n=6	
Temp. (K)	τ_1(ns)±0.1	τ_2(ns) ±0.1	τ_1(ns)±0.1	τ_2(ns) ±0.1	τ_1(ns)±0.1	τ_2(ns) ±0.1	τ_1(ns)±0.1	τ_2(ns) ±0.1	τ_1(ns)±0.1	τ_2(ns) ±0.1	τ_1(ns)±0.1	τ_2(ns) ±0.1
78	1.8	10.9	0.7	3.2	0.6	0.6	0.4	4.5	0.4	5.0	0.3	2.6
110	1.6	8.8	1.0	1.0	0.6	5.7	0.4	0.4	0.5	5.3	0.3	2.0
140	1.6	7.6	0.6	0.6	0.5	7.7	0.3	2.5	0.6	4.7	0.3	2.4
170	2.1	7.9	0.5	0.6	0.4	8.3	0.3	1.9	0.4	5.4	0.2	1.5
200	1.9	10.1	0.4	4.6	0.4	2.7	0.3	2.2	0.4	0.5	0.2	1.8

230	1.5	7.9	0.4	4.1	0.4	2.9	0.3	2.0	0.3	0.4	0.3	2.4
260	1.2	5.3	0.4	4.0	0.4	3.1	0.3	1.5	0.3	0.4	0.2	0.9
290	1.1	6.5	0.5	4.2	0.3	2.5	0.2	0.9	0.3	2.2	0.2	1.0

In order to determine the role of traps in the emission spectra, we have performed temperature dependent PL measurements for all samples were in the 78-293K temperature range **(Figure42)**. All samples exhibit narrowing of the emission peaks at the temperature decreases, suggesting that a large fraction of the emitted light is produced via thermally activated processes.

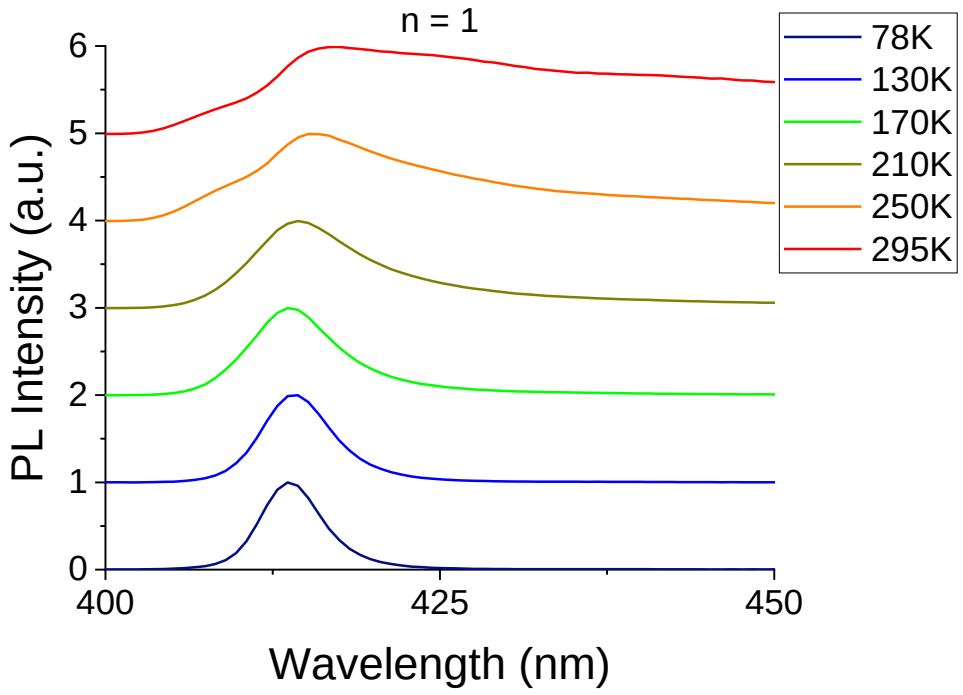

Figure 42: Normalized Time resolved PL decay measurements for $(HA)_2PbBr_4$ in different temperatures, clearly displaying a temperature-dependent broadening.

As the number of layers increases, more trapped states appear to affect the PL emission of the crystals, as shown in **Figure 43**. We attribute this phenomenon to the so-called "edge effect"[45], first reported by J.-C. Blancon et al. in 2017. While the primary peaks of our samples correspond to the emission of the chemically pure crystals, the secondary peaks roughly approach the emission of the bulk material. This is in agreement with observations that correspond to the edge effect and are caused by defect states created at the edges or the defects of the crystals. These edge states, tend to approximate the emission of the bulk perovskite, but they are also distinctively different in terms of recombination lifetimes and absolute emission wavelength. The fact that we observe the clean excitonic peak at low temperatures suggests that the compounds are chemically and optically pure and the secondary peaks are more likely trap states rather than secondary phases. This scenario is consistent with our structural data.

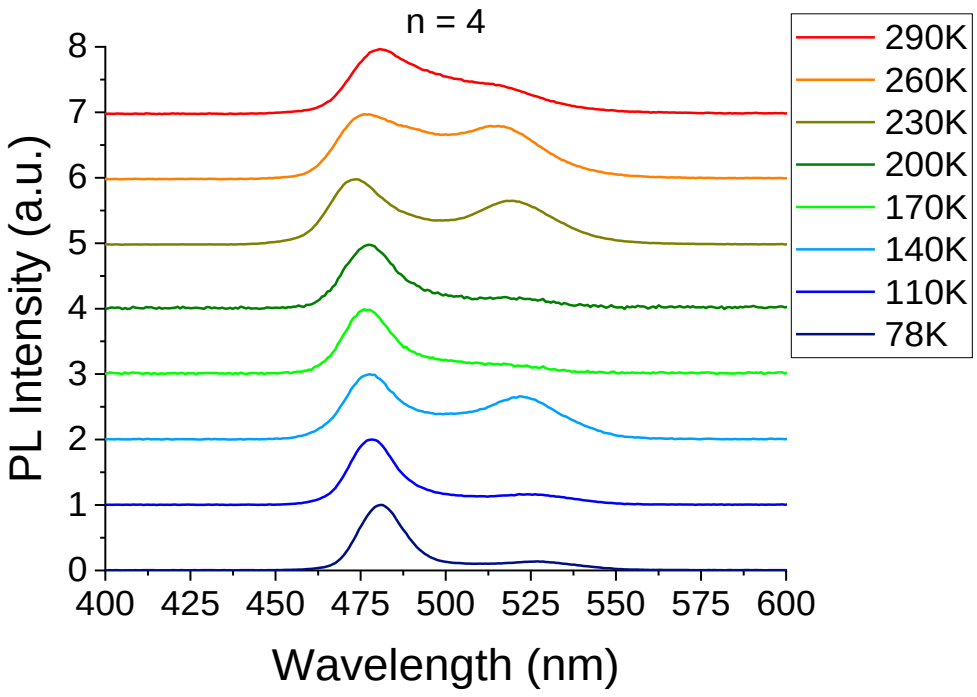

Figure 43: Normalized Time resolved PL decay measurements for $(HA)_2(MA)_3Pb_4Br_{13}$ in different temperatures, exhibiting secondary emission peaks at different temperatures.

Ab initio calculations (DFT), as well as DOS calculations were performed for the n=1-5 compounds. The results give us some insight into the optoelectronic phenomena taking place in each structure. All compounds appear to have clear band edges at the Γ-point of the Brillouin zone, making them direct bandgap semiconductors. The experimentally determined trend of energy gaps that are inversely proportional to the number of layers is confirmed by the theoretical calculations. Density of states calculations reveal the orbitals that form these bands. The -s orbitals of Br, are the main contributors of electrons to the valence band, while the -p orbitals of Pb are contributing in the formation of the conduction band edge. Both bands exhibit high dispersion, without any noticeable flattening which might be characteristic of other 2D layered perovskites.

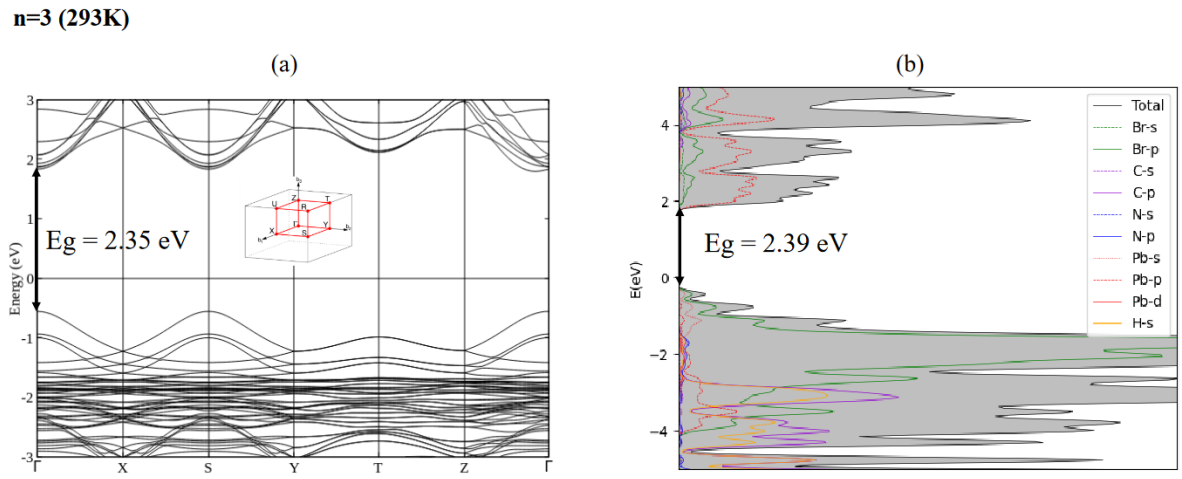

Figure 44: DFT (PBE) calculated band structure (BS) (a) and partial Density of States (PDOS) (b) of the n = 3 member of the (HA)2(MA)n-1PbnBr3n+1 series. The Fermi level is set to 0 eV.

CONCLUSIONS

A new Ruddlesden-Popper homologous series has been successfully synthesized and characterized. The $(HA)_2(MA)_{n-1}Pb_nBr_{3n+1}$ (n=1-6) compounds exhibit temperature-dependent, reversible structural phase transitions close to room temperature with n=1, 2 and 3 being below the transition temperature while n = 4, 5 and 6 being above at 293K. The n=1 and 2 compounds exhibit incommensurately modulated structures at that temperature, which appears to impact their PL emission bandwidth noticeably. All the compounds reach their high symmetry phase at 393K, crystallize in the pseudo tetragonal symmetry (*I*4/*mmm* is the maximal space group) ut were instead refined in the monoclinic non-centrosymmetric *Cm* space group to model the disordered spacer cations. All the compounds are semiconductors with bandgaps between 2.99 eV (n=1) – 2.44 eV (n=6) and emissions that get narrower as the number of layers increases. As it was expected, the energy gap increases as the number of layers decreases ($Eg_{n=1}$> $Eg_{n=2}$> $Eg_{n=3}$> $Eg_{n=4}$> $Eg_{n=5}$> $Eg_{n=6}$). Time-resolved PL measurements shows that for n>3 the compounds exhibit pure excitonic characteristics with PL carrier recombination lifetimes being in the few hundred picoseconds while n = 1 and n = 2 which exhibit severe structural modulation exhibit much longer lifetimes, influenced by trapping effects. DFT calculations support the experimental data suggesting a direct bandgap for n-members of the series. The present study opens a new direction in the study of 2D perovskites by directly correlating the structural modulation caused by structural phase transitions with the trends in the observed photo-physical properties. Further studies will be dedicated to the complete mapping of the phase transitions present in 2D lead bromide perovskites and assess whether the structural modulation trend can be observed in similar systems with variable spacer chain lengths.

METHODS

Materials. PbO (99.9%), hydro bromic acid (HBr, 48% w/w in H_2O) and hexylamine (HA) MAI (>99.5%) were purchased from Merck and used as received. CH_3NH_3Cl was synthesized from a neutralization reaction (pH = 7) of 37% w/w aqueous HCl 40% w/w aqueous CH_3NH_2.

Synthesis of $(HA)_2PbBr_4$ (n=1).

PbO (223.2mg, 1mmol) was added in a 20mL scintillation vial and dissolved in HBr (4mL), under continuous stirring at 125ºC. When the solution became clear, the HA(66μL, 0.5 mmol) was added. After 10 minutes, stirring was discontinued and the reaction was allowed to cool naturally to ambient temperature. After 10 minutes, yellow, plate-like crystals precipitated at the bottom of the vial. The resultant precipitate was isolated via suction filtration. Yields were calculated based on $C_6H_{15}N$, which is the limiting reagent. Yield ~73%.

Synthesis of $(HA)_2(MA)Pb_2Br_7$ (n=2).

PbO (446.4mg, 2mmol) and CH_3NH_3Cl (67.5mg, 1mmol) were added in a 20mL scintillation vial and dissolved in HBr (4mL), under continuous stirring at 125ºC. When the solution became clear, the *n* – $CH_3(CH_2)_5NH_2$ (77μL, 0.58 mmol) was added. After 10 minutes, stirring was discontinued and the reaction was allowed to cool naturally to ambient temperature. After 10 minutes, yellow, plate-like crystals precipitated at the bottom of the vial. The resultant precipitate was isolated via suction filtration. Yield (based on $C_6H_{15}N$) ~44%.

Synthesis of $(HA)_2(MA)_2Pb_3Br_{10}$ (n=3).

PbO (669.6mg, 3mmol) and CH_3NH_3Cl (135.0mg, 2mmol) were added in a 20mL scintillation vial and dissolved in HBr (4mL), under continuous stirring at 125ºC. When the solution became clear, the *n* – $CH_3(CH_2)_5NH_2$ (79μL, 0.6 mmol) was added. After 10 minutes, stirring was discontinued and the reaction was allowed to cool naturally to ambient temperature. After 10 minutes, yellow, plate-like crystals precipitated at the bottom of the vial. The resultant precipitate was isolated via suction filtration. Yield (based on $C_6H_{15}N$) ~31%.

Synthesis of $(HA)_2(MA)_3Pb_4Br_{13}$ (n=4).

PbO (892.8 mg, 4mmol) and CH_3NH_3Cl (202.6mg, 3mmol) were added in a 20mL scintillation vial and dissolved in HBr (4mL), under continuous stirring at 125ºC. When the solution became clear, the *n* –

$CH_3(CH_2)_5NH_2$ (92μL, 0.7 mmol) was added. After 10 minutes, stirring was discontinued and the reaction was allowed to cool naturally to ambient temperature. After 10 minutes, yellow, plate-like crystals precipitated at the bottom of the vial. The resultant precipitate was isolated via suction filtration. Yield (based on $C_6H_{15}N$) ~26%.

Synthesis of $(HA)_2(MA)_4Pb_5Br_{16}$ (n=5).

PbO (1116mg, 5mmol) and CH_3NH_3Cl (299.8, 4.44mmol) were added in a 20mL scintillation vial and dissolved in HBr (4mL), under continuous stirring at 125ºC. When the solution became clear, the *n* – $CH_3(CH_2)_5NH_2$ (98μL, 0.74 mmol) was added. After 10 minutes, stirring was discontinued and the reaction was allowed to cool naturally to ambient temperature. After 10 minutes, yellow, plate-like crystals precipitated at the bottom of the vial. The resultant precipitate was isolated via suction filtration. Yield (based on $C_6H_{15}N$) ~20%.

Synthesis of $(HA)_2(MA)_5Pb_6Br_{19}$ (n=6).

PbO (1116 mg, 5mmol) and CH_3NH_3Cl (202, 3mmol) were added in a 20mL scintillation vial and dissolved in HBr (12mL), under continuous stirring at 125ºC. When the solution became clear, the n – $CH_3(CH_2)_5NH_2$ (97μL, 0.73 mmol) was added. After 10 minutes, stirring was discontinued and the reaction was allowed to cool naturally to ambient temperature. After 10 minutes, yellow, plate-like crystals precipitated at the bottom of the vial. The resultant precipitate was isolated via suction filtration. Yield (based on $C_6H_{15}N$) ~16%.

Scanning Electron Microscopy with Energy Dispersive Spectroscopy (SEM/EDS): SEM images and elemental microprobe analyses were performed using a JEOL JSM-6390LV SEM system equipped with an Oxford INCA PentaFETx3 EDS detector (Oxfordshire, UK). Data acquisition was performed using an accelerating voltage of 20kV and a 60 s accumulation time.

Powder X-ray Diffraction (XRD):

Powder X-ray diffraction measurements were performed using a Rigaku SmartLab SE automated multipurpose diffractometer equipped with a theta-theta goniometer and a horizontal sample mount, operating at 40kV and 50 mA, measuring from $2\theta = 2\text{-}60^{O}$.

Single Crystal X-ray Diffraction: Full-sphere data were collected using a Bruker D8 VENTURE diffractometer equipped with a Kappa goniometer stage, a PHOTON II CPAD detector, and an IμS 3.0 Mo Kα source (λ = 0.71073 Å). Data were collected at 293 K. The collected data were integrated and applied with multiscan absorption correction using the APEX3 software. Crystal structures were solved by charge flipping and refined (full-matrix least-squares on F^2) using the Jana2006 package[46].

Differential Scanning Calorimetry (DSC). A full set of data were collected via DSC-250 for all n compounds. Approximately 2.3 mg of each sample were placed in aluminum pans which were then hermetically closed. They were placed in the calorimeter along with an empty reference pan. The samples were first maintained in a 2 min isothermal state and then heated from 30 ℃ up to 170 ℃ with a rate of 10 ℃/min. The samples then maintained in a 2 min isothermal state and then cooled from 170 ℃ down to 30 ℃ with a rate of 10 ℃/min. The process was repeated twice, with the first cycle discarded as it was performed only to erase the samples thermal history.

Optical Absorption Spectroscopy. Optical diffuse reflectance measurements were performed using a Shimadzu UV-2600 plus UV-vis-NIR spectrometer operating in the 185-1400 nm region using $BaSO_4$ as the reference of 100% reflectance. The band gap of the material was estimated by converting reflectance to absorption according to the Kubelka-Munk equation: $\frac{\alpha}{s} = \frac{(1-R)2}{2R}$, where R is the reflectance and α and S are the absorption and scattering coefficients[47], respectively.

Photoluminescence

Photoluminescence (PL) was performed on a homemade microscopic setup. The excitation source was a 375 nm ps laser (Picoquant LDHD-C-375). A 10x objective ((Mitutoyo, 10X, NA=0.28)) focused the laser on the sample and collected the PL signal. A dichroic mirror was placed on the path to block the excitation laser and then the PL signal was focused into a spectrograph (Andor Kymera 328i) and guided to a Si EMCCD (Andor iXon Life 888) to eventually generate the time-integrated PL spectra. The PL signal was also focused into homemade time-correlated single photon counting (TCSPC) to get the time-resolved PL. For temperature-dependent PL, the samples were mounted in a liquid-nitrogen cryostat (Janis VPF-100) with a low pressure of less than 10^{-4} Torr.

REFERENCES

1. Naray-Szabo, S., *Die Strukturen von Verbindungen ABO 3„Schwesterstrukturen.“.* Die Naturwissenschaften, 1943. **31**(39-40): p. 466-466.
2. Megaw, H.D., *Crystal structure of double oxides of the perovskite type.* Proceedings of the Physical Society, 1946. **58**(2): p. 133.
3. Goldschmidt, V.M., *Die gesetze der krystallochemie.* Naturwissenschaften, 1926. **14**(21): p. 477-485.
4. Glazer, A.M., *The classification of tilted octahedra in perovskites.* Acta Crystallographica Section B: Structural Crystallography and Crystal Chemistry, 1972. **28**(11): p. 3384-3392.
5. Kojima, A., et al., *Organometal Halide Perovskites as Visible-Light Sensitizers for Photovoltaic Cells.* Journal of the American Chemical Society, 2009. **131**(17): p. 6050-6051.
6. Weber, D., *CH3NH3PbX3, ein Pb (II)-system mit kubischer perowskitstruktur/CH3NH3PbX3, a Pb (II)-system with cubic perovskite structure.* Zeitschrift für Naturforschung B, 1978. **33**(12): p. 1443-1445.
7. Androulakis, J., et al., *Dimensional reduction: a design tool for new radiation detection materials.* Advanced Materials, 2011. **23**(36): p. 4163-4167.
8. MØLler, C.K., *Crystal Structure and Photoconductivity of Cæsium Plumbohalides.* Nature, 1958. **182**(4647): p. 1436-1436.
9. Seliger, J., et al., *Proton-14N double resonance study of the structural phase transitions in the perovskite type layer compound (CH3NH3)2CdCl4.* Zeitschrift für Physik B Condensed Matter, 1976. **25**(2): p. 189-195.
10. Wells, H.L., *Über die Cäsium- und Kalium-Bleihalogenide.* Zeitschrift für anorganische Chemie, 1893. **3**(1): p. 195-210.
11. Papavassiliou, G.C. and I. Koutselas, *Structural, optical and related properties of some natural three-and lower-dimensional semiconductor systems.* Synthetic Metals, 1995. **71**(1-3): p. 1713-1714.
12. Eperon, G.E., et al., *Formamidinium lead trihalide: a broadly tunable perovskite for efficient planar heterojunction solar cells.* Energy & Environmental Science, 2014. **7**(3): p. 982-988.
13. Tulsky, E.G. and J.R. Long, *Dimensional reduction: a practical formalism for manipulating solid structures.* Chemistry of materials, 2001. **13**(4): p. 1149-1166.
14. Androulakis, J., et al., *Dimensional Reduction: A Design Tool for New Radiation Detection Materials.* Advanced Materials, 2011. **23**(36): p. 4163-4167.
15. Tanaka, K. and T. Kondo, *Bandgap and exciton binding energies in lead-iodide-based natural quantum-well crystals.* Science and Technology of Advanced Materials, 2003. **4**(6): p. 599-604.
16. Dion, M., M. Ganne, and M. Tournoux, *Nouvelles familles de phases MIMII2Nb3O10 a feuillets “perovskites”.* Materials Research Bulletin, 1981. **16**(11): p. 1429-1435.
17. Jacobson, A. and J. Hutchison, *An investigation of the structure of 12HBaCoO2. 6 by electron microscopy and powder neutron diffraction.* Journal of Solid State Chemistry, 1980. **35**(3): p. 334-340.
18. Ruddlesden, S.N. and P. Popper, *The compound Sr3Ti2O7 and its structure.* Acta Crystallographica, 1958. **11**(1): p. 54-55.
19. Mao, L., et al., *Hybrid Dion–Jacobson 2D Lead Iodide Perovskites.* Journal of the American Chemical Society, 2018. **140**(10): p. 3775-3783.
20. Mazin, I. and S. Rashkeev, *Effect of low symmetry on electron-phonon coupling in perovskite superconductors.* Solid state communications, 1988. **68**(1): p. 93-95.
21. Rupprecht, G. and R. Bell, *Dielectric constant in paraelectric perovskites.* Physical Review, 1964. **135**(3A): p. A748.
22. Katan, C., N. Mercier, and J. Even, *Quantum and Dielectric Confinement Effects in Lower-Dimensional Hybrid Perovskite Semiconductors.* Chemical Reviews, 2019. **119**(5): p. 3140-3192.

23. Andrews, D.L., *Quantum dynamics of simple systems.* Quantum and Semiclassical Optics: Journal of the European Optical Society Part B, 1996. **8**(6): p. 010.
24. Wannier, G.H., *The Structure of Electronic Excitation Levels in Insulating Crystals.* Physical Review, 1937. **52**(3): p. 191-197.
25. Frenkel, J., *On the Transformation of light into Heat in Solids. I.* Physical Review, 1931. **37**(1): p. 17-44.
26. Soe, C.M.M., et al., *Structural and thermodynamic limits of layer thickness in 2D halide perovskites.* Proceedings of the National Academy of Sciences, 2019. **116**(1): p. 58-66.
27. Kataoka, T., et al., *Magneto-optical study on excitonic spectra in (${\mathrm{C}}_{6}$${\mathrm{H}}_{13}$${\mathrm{NH}}_{3}$$)}_{2}$${\mathrm{PbI}}_{4}$.* Physical Review B, 1993. **47**(4): p. 2010-2018.
28. Reci, A., et al., *Optimising sampling patterns for bi-exponentially decaying signals.* Magnetic Resonance Imaging, 2019. **56**: p. 14-18.
29. Vashishtha, P., et al., *High Efficiency Blue and Green Light-Emitting Diodes Using Ruddlesden–Popper Inorganic Mixed Halide Perovskites with Butylammonium Interlayers.* Chemistry of Materials, 2019. **31**(1): p. 83-89.
30. Tsai, H., et al., *High-efficiency two-dimensional Ruddlesden-Popper perovskite solar cells.* Nature, 2016. **536**(7616): p. 312-6.
31. Vasileiadou, E.S., et al., *Insight on the Stability of Thick Layers in 2D Ruddlesden–Popper and Dion–Jacobson Lead Iodide Perovskites.* Journal of the American Chemical Society, 2021. **143**(6): p. 2523-2536.
32. Gong, J., et al., *Layered 2D Halide Perovskites beyond the Ruddlesden–Popper Phase: Tailored Interlayer Chemistries for High-Performance Solar Cells.* Angewandte Chemie International Edition, 2022. **61**(10): p. e202112022.
33. Stoumpos, C.C., et al., *Ruddlesden–Popper Hybrid Lead Iodide Perovskite 2D Homologous Semiconductors.* Chemistry of Materials, 2016. **28**(8): p. 2852-2867.
34. Tsai, H., et al., *Stable Light-Emitting Diodes Using Phase-Pure Ruddlesden–Popper Layered Perovskites.* Advanced Materials, 2018. **30**(6): p. 1704217.
35. Mercier, N., *Hybrid Halide Perovskites: Discussions on Terminology and Materials.* Angewandte Chemie International Edition, 2019. **58**(50): p. 17912-17917.
36. Hoffman, J.M., et al., *Long periodic ripple in a 2D hybrid halide perovskite structure using branched organic spacers.* Chemical Science, 2020. **11**(44): p. 12139-12148.
37. Morris, C.D., C.D. Malliakas, and M.G. Kanatzidis, *Germanium Selenophosphates: The Incommensurately Modulated 1/∞[Ge4-xPxSe124–] and the Molecular [Ge2P2Se14]6–.* Inorganic Chemistry, 2011. **50**(20): p. 10241-10248.
38. Petříček, V. and M. Dušek. *Modulation and its Crystallographic Methodology*. in *High-Pressure Crystallography*. 2004. Dordrecht: Springer Netherlands.
39. Janssen, T., et al., *Incommensurate and commensurate modulated structures*, in *International Tables for Crystallography Volume C: Mathematical, physical and chemical tables*, E. Prince, Editor. 2004, Springer Netherlands: Dordrecht. p. 907-955.
40. Li, C., et al., *Ultrafast and broadband photodetectors based on a perovskite/organic bulk heterojunction for large-dynamic-range imaging.* Light: Science & Applications, 2020. **9**(1): p. 31.
41. Steirer, K.X., et al., *Defect tolerance in methylammonium lead triiodide perovskite.* ACS Energy Letters, 2016. **1**(2): p. 360-366.
42. Chondroudis, K., T.J. McCarthy, and M.G. Kanatzidis, *Chemistry in Molten Alkali Metal Polyselenophosphate Fluxes. Influence of Flux Composition on Dimensionality. Layers and Chains in APbPSe4, A4Pb(PSe4)2 (A = Rb, Cs), and K4Eu(PSe4)2.* Inorganic Chemistry, 1996. **35**(4): p. 840-844.
43. McCarthy, T.J. and M.G. Kanatzidis, *Synthesis in Molten Alkali Metal Polyselenophosphate Fluxes: A New Family of Transition Metal Selenophosphate Compounds, A2MP2Se6 (A = K, Rb,*

Cs; M = Mn, Fe) and A2M'2P2Se6 (A = K, Cs; M' = Cu, Ag). Inorganic Chemistry, 1995. **34**(5): p. 1257-1267.
44. Hirasawa, M., et al., *Magnetoabsorption of the lowest exciton in perovskite-type compound (CH3NH3) PbI3.* Physica B: Condensed Matter, 1994. **201**: p. 427-430.
45. Blancon, J.-C., et al., *Extremely efficient internal exciton dissociation through edge states in layered 2D perovskites.* Science, 2017. **355**(6331): p. 1288-1292.
46. Mao, L., et al., *Seven-Layered 2D Hybrid Lead Iodide Perovskites.* Chem, 2019. **5**(10): p. 2593-2604.
47. Christy, A.A., O.M. Kvalheim, and R.A. Velapoldi, *Quantitative analysis in diffuse reflectance spectrometry: A modified Kubelka-Munk equation.* Vibrational Spectroscopy, 1995. **9**(1): p. 19-27.

APPENDIX

TABLES

Table S1. Bond Distances for $(HA)_2(MA)_{n-1}Pb_nBr_{3n+1}$ at 293K.

$(HA)_2PbBr_4$		$(HA)_2(MA)_1Pb_2Br_7$		$(HA)_2(MA)_2Pb_3Br_{10}$		$(HA)_2(MA)_3Pb_4Br_{13}$		$(HA)_2(MA)_4Pb_5Br_{16}$	
Label	Distances (Å)	Label	Distances (Å)	Label	Distances (Å)	Label	Distances (Å)	Label	Distances (Å)
Pb(1)-Br(1)	2.996(4)	Pb(1)-Br(1)	3.05(5)	Pb(1)-Br(1)	2.945(17)	Pb(1)-Br(1)	3.004(4)	Pb(1)-Br(3)	2.994(3)
		Pb(1)-Br(3)	2.97(3)	Pb(1)-Br(1)#0	2.985(17)	Pb(1)-Br(1)#0	2.919(4)	Pb(1)-Br(5)	3.010(9)
		Pb(1)-Br(4)	2.85(5)	Pb(1)-Br(2)	2.967(2)	Pb(1)-Br(4)#0	2.987(4)	Pb(1)-Br(5)#0	2.906(9)
		Pb(1)-Br(5)	2.994(19)	Pb(2)-Br(2)	3.098(2)	Pb(1)-Br(6)#0	3.208(3)	Pb(2)-Br(1)	3.067(6)
				Pb(2)-Br(3)	2.835(4)	Pb(1)-Br(12)	2.748(6)	Pb(2)-Br(1)#0	2.855(5)
				Pb(2)-Br(4)	2.950(15)	Pb(2)-Br(2)	2.968(2)	Pb(2)-Br(3)	2.977(3)
				Pb(2)-Br(4)#0	2.984(15)	Pb(2)-Br(2)#0	2.992(3)	Pb(2)-Br(4)	2.927(3)
				Pb(2)-Br(5)	2.946(16)	Pb(2)-Br(3)	2.952(4)	Pb(2)-Br(7)	2.849(6)
				Pb(2)-Br(5)#0	2.979(16)	Pb(2)-Br(3)#0	3.012(3)	Pb(2)-Br(7)#0	3.072(6)
						Pb(2)-Br(5)	3.054(5)	Pb(3)-Br(2)	3.000(6)
						Pb(2)-Br(6)	2.857(3)	Pb(3)-Br(2)#0	2.924(5)
						Pb(3)-Br(5)#0	2.977(5)	Pb(3)-Br(4)#0	3.096(3)
						Pb(3)-Br(7)	3.038(6)	Pb(3)-Br(6)	2.876(7)
						Pb(3)-Br(9)	2.923(3)	Pb(3)-Br(6)#0	3.050(6)
						Pb(3)-Br(9)#0	3.030(4)	Pb(3)-Br(8)	2.779(6)
						Pb(3)-Br(10)#0	2.959(5)		
						Pb(3)-Br(10)#0	2.977(4)		
						Pb(4)-Br(7)#0	3.040(6)		
						Pb(4)-Br(8)	3.019(5)		

						Pb(4)-Br(8)#0	2.904(5)		
						Pb(4)-Br(11)	2.988(5)		
						Pb(4)-Br(11)#0	2.911(5)		
						Pb(4)-Br(13)	2.892(7)		
Average					2.9618		2.9668		2.9423

Table S2. Bond Angles for $(HA)_2(MA)_{n-1}Pb_nBr_{3n+1}$ at 293K.

$(HA)_2PbBr_4$		$(HA)_2(MA)_1Pb_2Br_7$		$(HA)_2(MA)_2Pb_3Br_{10}$		$(HA)_2(MA)_3Pb_4Br_{13}$		$(HA)_2(MA)_4Pb_5Br_{16}$	
Label	Angle (°)	Label	Angle (°)	Label	Angle (°)	Label	Angle (°)	Label	Angle (°)
Pb(1)-Br(1)-Pb(1)#0	153.44(10)	Pb(1)-Br(1)-Pb(2)	174.4(7)	Pb(1)-Br(1)-Pb(1)#0	178.9(7)	Pb(1)-Br(1)-Pb(1)#0	175.00(17)	Pb(2)-Br(1)-Pb(2)#0	173.2(2)
		Pb(2)-Br(2)-Pb(2) #0	165.6(10)	Pb(1)-Br(2)-Pb(2)	178.0(8)	Pb(2)-Br(2)-Pb(2)#0	164.50(11)	Pb(3)-Br(2)-Pb(3)#0	172.9(2)
				Pb(2)-Br(4)-Pb(2)#0	179.0(5)	Pb(2)-Br(3)-Pb(2)#0	164.88(14)	Pb(1)-Br(3)-Pb(2)	176.48(15)
				Pb(2)-Br(5)-Pb(2)#0	178.4(5)	Pb(1)-Br(4)-Pb(1)#0	175.3(2)	Pb(2)-Br(4)-Pb(3)#0	173.70(15)
						Pb(2)-Br(5)-Pb(3)#0	178.77(13)	Pb(1)-Br(5)-Pb(1)#0	177.4(2)
						Pb(1)#0-Br(6)-Pb(2)	177.21(9)	Pb(3)-Br(6)-Pb(3)#0	173.4(2)
						Pb(3)-Br(7)-Pb(4)#0	174.90(18)	Pb(2)-Br(7)-Pb(2)#0	176.86(19)
						Pb(3)-Br(9)-Pb(3)#0	166.93(13)		
						Pb(3)#0-Br(10)-Pb(3)#0	167.97(18)		
						Pb(4)-Br(8)-Pb(4)#0	175.3(3)		
						Pb(4)-Br(11)-Pb(4)#0	179.3(2)		

Average					171.6		172.7		174.8

Table S3. Bond Distances for $(HA)_2(MA)_{n-1}Pb_nBr_{3n+1}$ at 393K.

$(HA)_2PbBr_4$		$(HA)_2(MA)_1Pb_2Br_7$		$(HA)_2(MA)_2Pb_3Br_{10}$		$(HA)_2(MA)_3Pb_4Br_{13}$		$(HA)_2(MA)_4Pb_5Br_{16}$	
Label	Distances (Å)	Label	Distances (Å)	Label	Distances (Å)	Label	Distances (Å)	Label	Distances (Å)
Pb(1)-Br(1)	3.001(7)	Pb(1)-Br(1)#0	3.063(7)	Pb(1)-Br(1)#0	2.926(5)	Pb(1)-Br(1)	2.997(13)	Pb(1)-Br(1)	2.982(10)
Pb(1)-Br(2)#0	2.987(7)	Pb(1)-Br(2)	2.980(15)	Pb(1)-Br(1)#0	3.013(5)	Pb(1)-Br(1)#0	2.945(13)	Pb(1)-Br(1)#0	2.964(11)
Pb(1)-Br(3)#0	2.977(7)	Pb(1)-Br(3)#0	3.027(14)	Pb(2)-Br(1)	2.952(7)	Pb(1)-Br(4)#0	3.102(18)	Pb(1)-Br(2)	3.050(4)
Pb(1)-Br(4)#0	2.965(7)	Pb(1)-Br(4)	2.956(14)	Pb(2)-Br(2)	2.988(6)	Pb(1)-Br(5)	2.880(15)	Pb(1)-Br(8)	2.912(4)
Pb(1)-Br(5)	2.990(2)	Pb(1)-Br(5)#0	2.919(13)	Pb(2)-Br(3)	2.975(7)	Pb(2)-Br(2)	2.949(14)	Pb(2)-Br(2)	2.934(4)
Pb(2)-Br(1)	2.952(7)	Pb(1)-Br(6)	2.861(6)	Pb(2)-Br(4)	3.009(7)	Pb(2)-Br(2)#0	2.993(14)	Pb(2)-Br(5)	2.989(9)
Pb(2)-Br(2)	2.988(6)	Pb(2)-Br(1)#0	3.087(7)	Pb(2)-Br(6)	2.985(2)	Pb(2)-Br(3)	3.00(2)	Pb(2)-Br(5)#0	2.959(10)
Pb(2)-Br(3)	2.975(7)	Pb(2)-Br(2)	2.942(15)	Pb(2)-Br(4)	2.888(4)	Pb(2)-Br(4)#0	2.948(18)	Pb(2)-Br(9)	2.971(5)
Pb(2)-Br(4)	3.009(7)	Pb(2)-Br(3)#0	2.882(14)	Pb(2)-Br(6)#0	2.916(5)	Pb(3)-Br(6)	2.93(2)	Pb(3)-Br(3)	2.906(4)
Pb(2)-Br(6)	2.985(2)	Pb(2)-Br(4)#0	2.975(14)	Pb(2)-Br(6)#0	3.023(5)	Pb(3)-Br(7)	2.942(15)	Pb(3)-Br(4)	2.991(9)
		Pb(2)-Br(5)#0	3.005(13)	Pb(2)-Br(6)#0	2.916(5)	Pb(3)-Br(7)#0	2.999(15)	Pb(3)-Br(4)#0	2.958(10)
		Pb(2)-Br(7)	2.878(7)	Pb(2)-Br(6)#0	3.023(5)	Pb(4)-Br(6)	3.12(2)	Pb(3)-Br(4)#0	2.991(9)
				Pb(3)-Br(3)	3.151(4)	Pb(4)-Br(8)	2.941(14)	Pb(3)-Br(8)#0	3.084(4)
				Pb(3)-Br(5)	2.791(4)	Pb(4)-Br(8)#0	3.001(14)	Pb(4)-Br(3)	3.131(4)
				Pb(3)-Br(7)#0	2.881(4)	Pb(4)-Br(9)	2.786(18)	Pb(4)-Br(6)2.812(5)Pb(4)-Br(10)	2.972(8)

				Pb(3)-Br(7)#0	3.057(4)			Pb(4)-Br(10)#0	2.974(9)
								Pb(5)-Br(7)	2.972(7)
								Pb(5)-Br(7)#0	2.975(8)
								Pb(5)-Br(7)#0	2.972(7)
								Pb(5)-Br(9)	3.086(5)
								Pb(5)-Br(11)	2.862(5)
Average	2.985		2.965		2.969		3.218		2.974

Table S4. Bond Angles for $(HA)_2(MA)_{n-1}Pb_nBr_{3n+1}$ at 393K.

$(HA)_2PbBr_4$		**$(HA)_2(MA)_1Pb_2Br_7$**		**$(HA)_2(MA)_2Pb_3Br_{10}$**		**$(HA)_2(MA)_3Pb_4Br_{13}$**		**$(HA)_2(MA)_4Pb_5Br_{16}$**	
Label	Angle (°)	Label	Angle (°)	Label	Angle (°)	Label	Angle (°)	Label	Angle (°)
Pb(1)#0-Br(3)-Pb(2)	155.5(3)	Pb(1)#0-Br(1)-Pb(2)#0	173.4(5)	Pb(1)#0-Br(1)-Pb(1)#0	176.6(2)	Pb(2)-Br(2)-Pb(2)#0	179.1(5)	Pb(1)-Br(1)-Pb(1)#0	175.0(4)
Pb(1)#0-Br(2)-Pb(2)	152.6(2)	Pb(1)-Br(2)-Pb(2)	178.4(4)	Pb(1)-Br(2)-Pb(2)	174.28(10)	Pb(2)-Br(3)-Pb(3)	179.9(8)	Pb(1)-Br(2)-Pb(2)	174.201(18)
Pb(1)-Br(1)-Pb(2)	154.0(2)	Pb(1)#0-Br(3)-Pb(2)#0	177.9(4)	Pb(1)#0-Br(3)-Pb(3)	174.35(10)	Pb(1)#0-Br(4)-Pb(2)#0	179.2(7)	Pb(3)-Br(3)-Pb(4)	177.454(14)
Average	154.0	Pb(1)-Br(4)-Pb(2)#0	172.2(5)	Pb(2)#0-Br(6)-Pb(2)#0	176.36(16)	Pb(3)-Br(6)-Pb(4)	177.5(8)	Pb(3)-Br(4)-Pb(3)#0	173.9(3)

Pb(1)#0-Br(3)-Pb(2)	155.5(3)	Pb(1)#0-Br(5)-Pb(2)#0	172.7(5)	Pb(3)#0-Br(7)-Pb(3)#0	176.86(14)	Pb(3)-Br(7)-Pb(3)#0	179.5(6)	Pb(2)-Br(5)-Pb(2)#0	174.0(3)
						Pb(4)-Br(8)-Pb(4)#0	179.1(6)	Pb(5)-Br(7)-Pb(5)#0	174.5(3)
								Pb(1)-Br(8)-Pb(3)#0	175.073(17)
								Pb(2)-Br(9)-Pb(5)	176.47(2)
								Pb(4)-Br(10)-Pb(4)#0	175.0(3)
Average			174.9		175.7		179.1		175.1

APPENDIX FIGURES

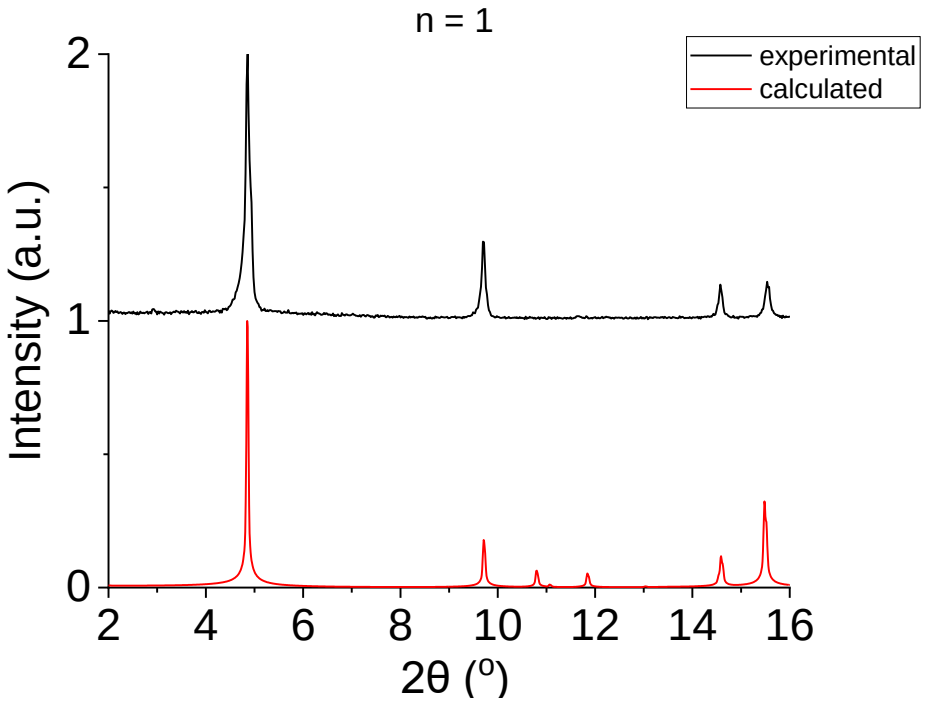

Figure S1: Powder X-ray diffraction (PXRD) patterns of the experimental n=1 compound compared to the calculated pattern at room temperature.

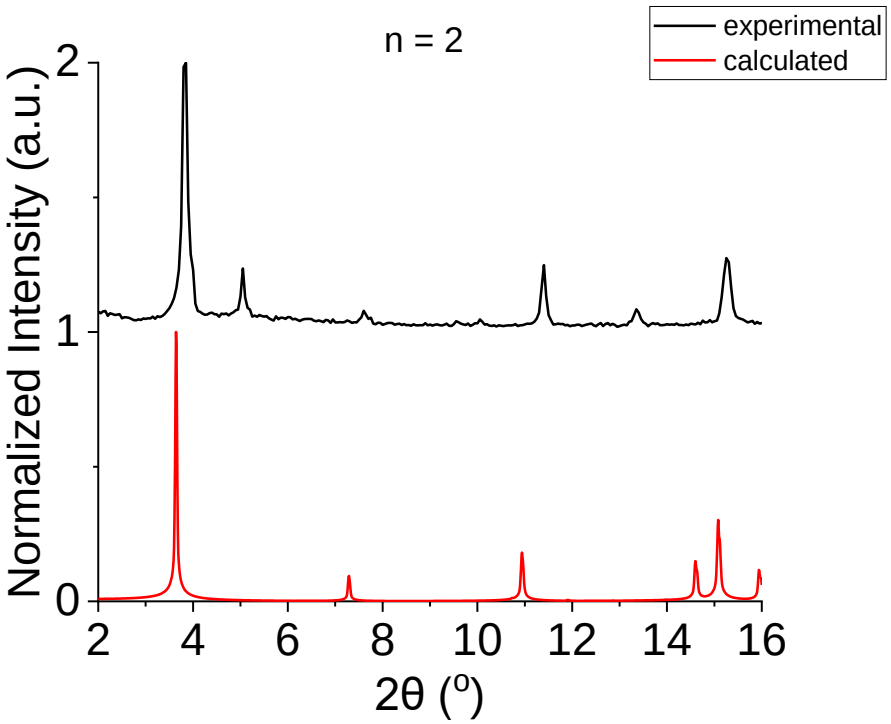

Figure S2: Powder X-ray diffraction (PXRD) patterns of the experimental n=2 compound compared to the calculated pattern at room temperature.

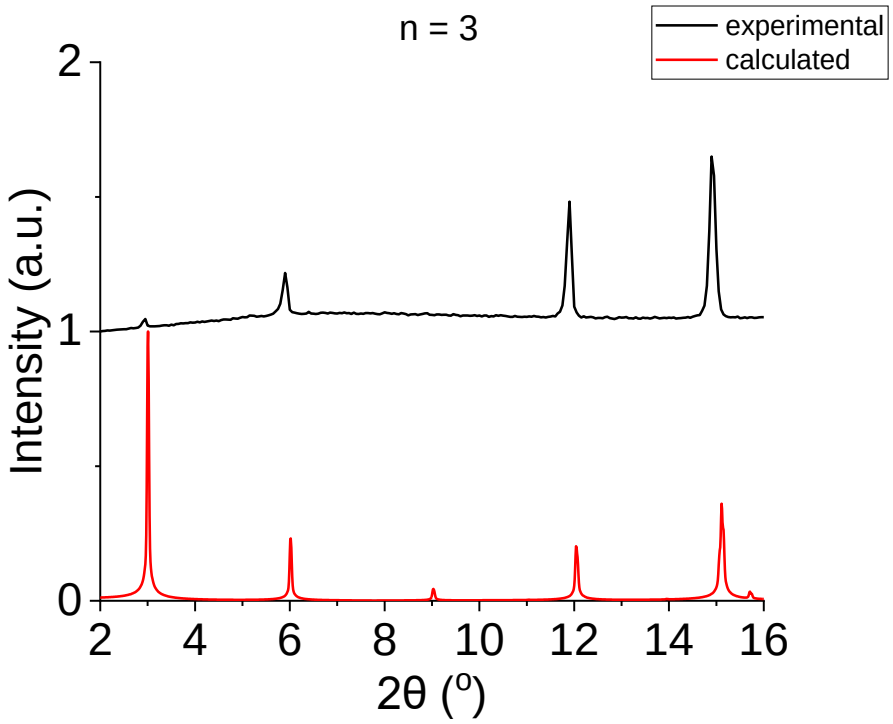

Figure S3: Powder X-ray diffraction (PXRD) patterns of the experimental n=3 compound compared to the calculated pattern at room temperature.

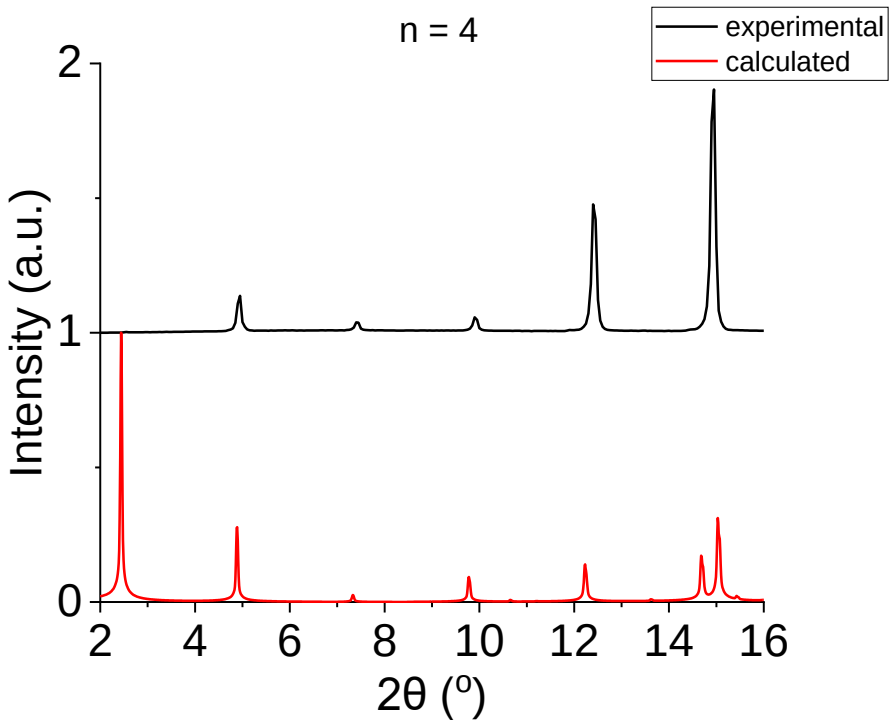

Figure S4: Powder X-ray diffraction (PXRD) patterns of the experimental n=4 compound compared to the calculated pattern at room temperature.

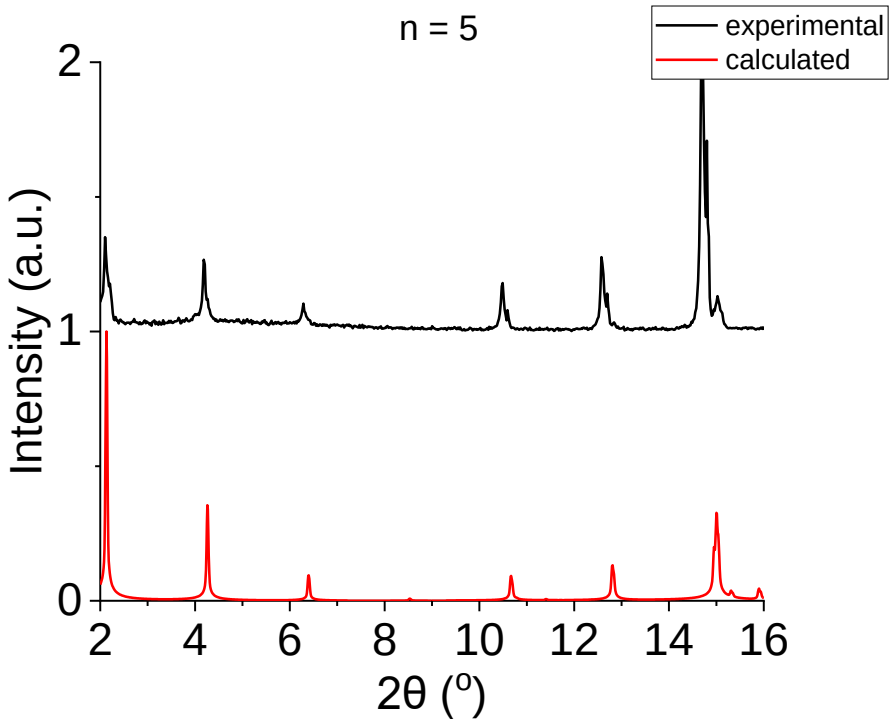

Figure S5: Powder X-ray diffraction (PXRD) patterns of the experimental n=5 compound compared to the calculated pattern at room temperature.

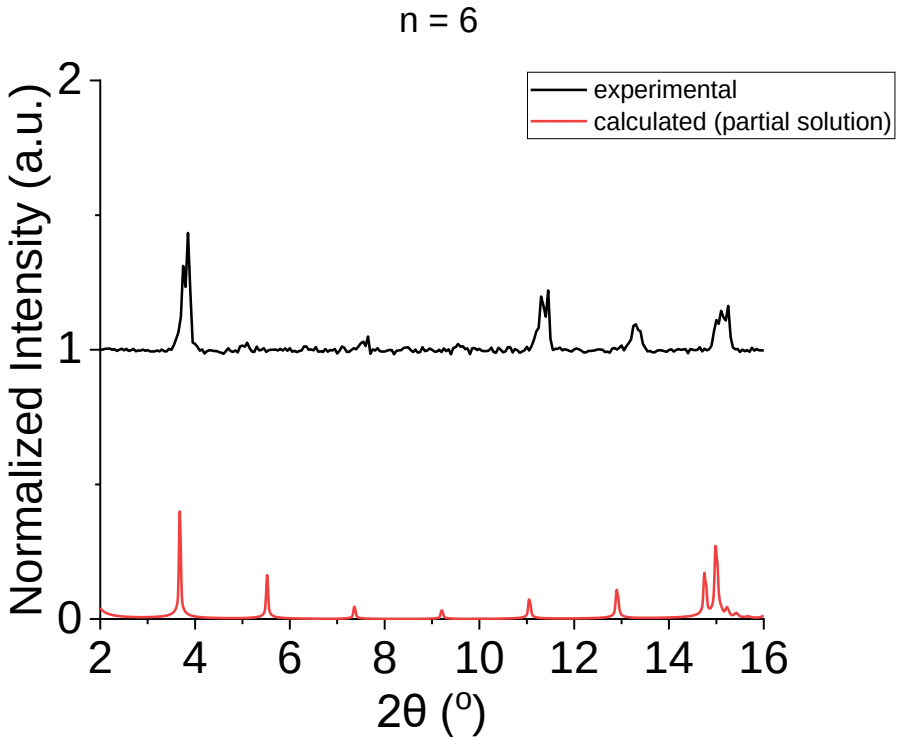

Figure S6: Powder X-ray diffraction (PXRD) patterns of the experimental n=6 compound compared to the calculated pattern at room temperature.

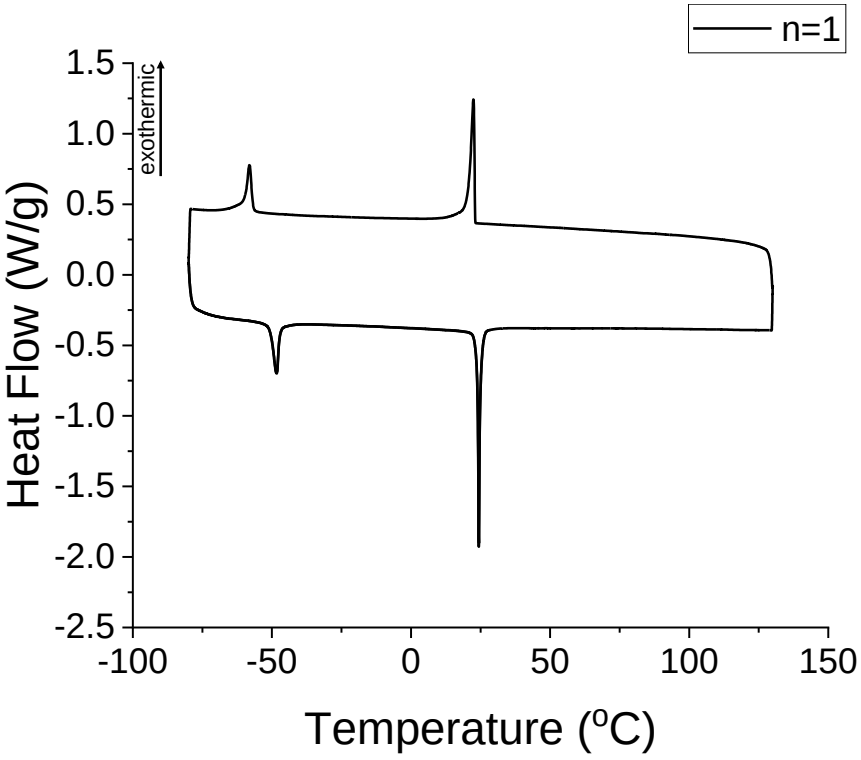

Figure S7: Differential Scanning Calorimetry (DSC) diagrams of n=1 depicting the phase transition that depicts 2 phase transitions at room temperature.

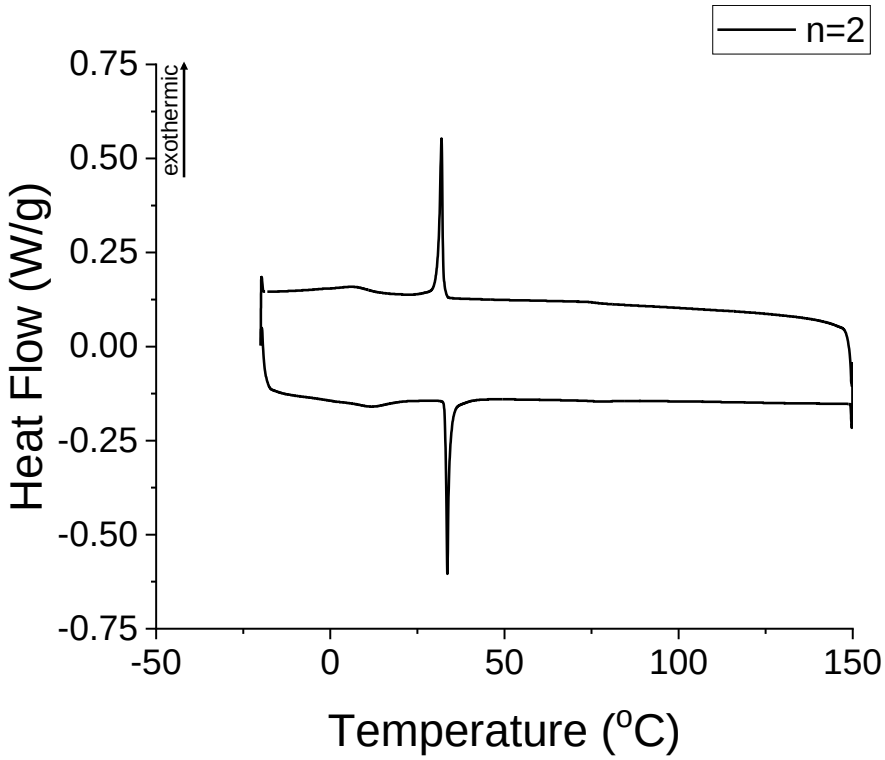

Figure S8: Differential Scanning Calorimetry (DSC) diagrams of n=2 depicting the phase transition that depicts 2 phase transitions at room temperature.

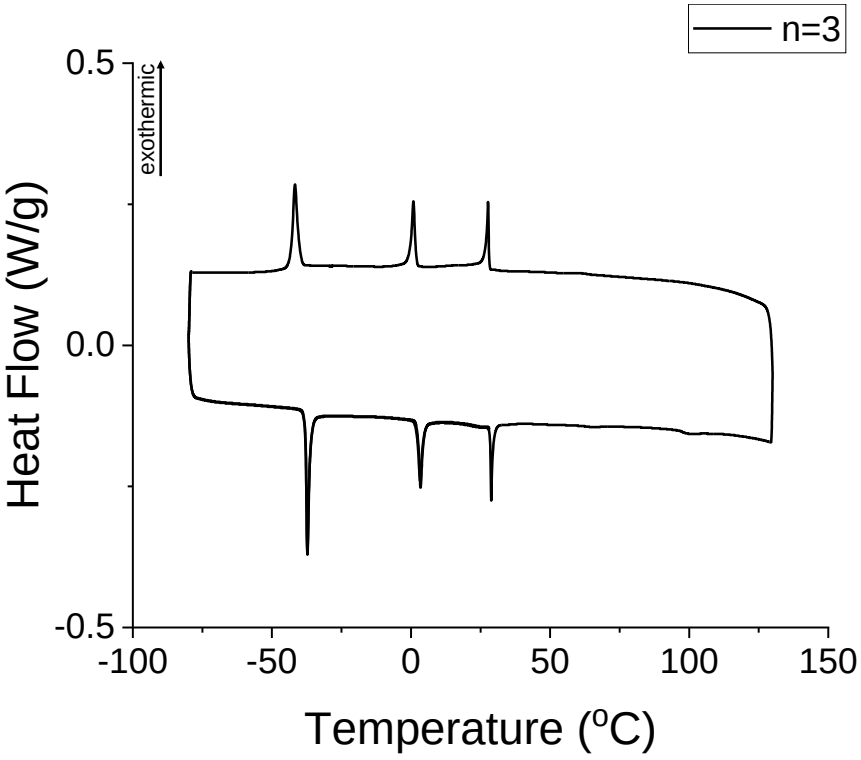

Figure S9: Differential Scanning Calorimetry (DSC) diagrams of n=3 depicting the phase transition that depicts 2 phase transitions at room temperature.

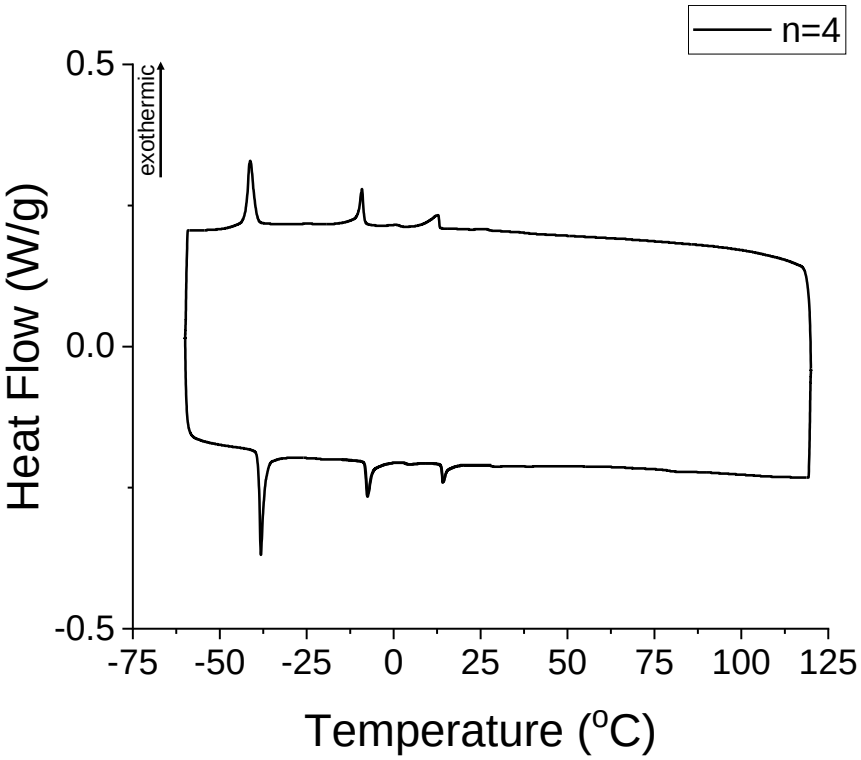

Figure S10: Differential Scanning Calorimetry (DSC) diagrams of n=4 depicting the phase transition that depicts 2 phase transitions at room temperature.

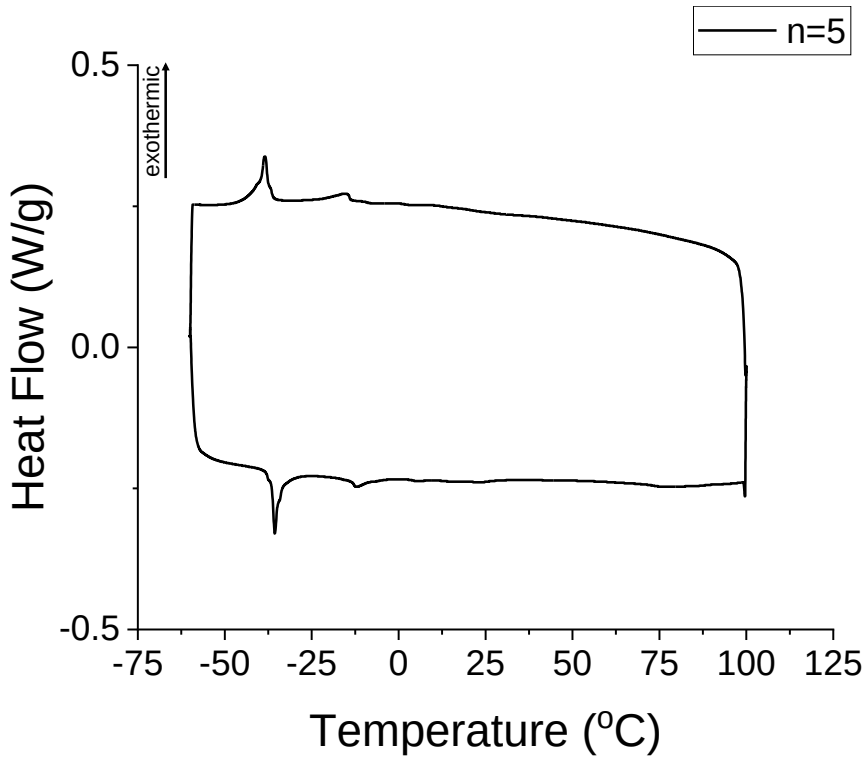

Figure S11: Differential Scanning Calorimetry (DSC) diagrams of n=5 depicting the phase transition that depicts 2 phase transitions at room temperature.

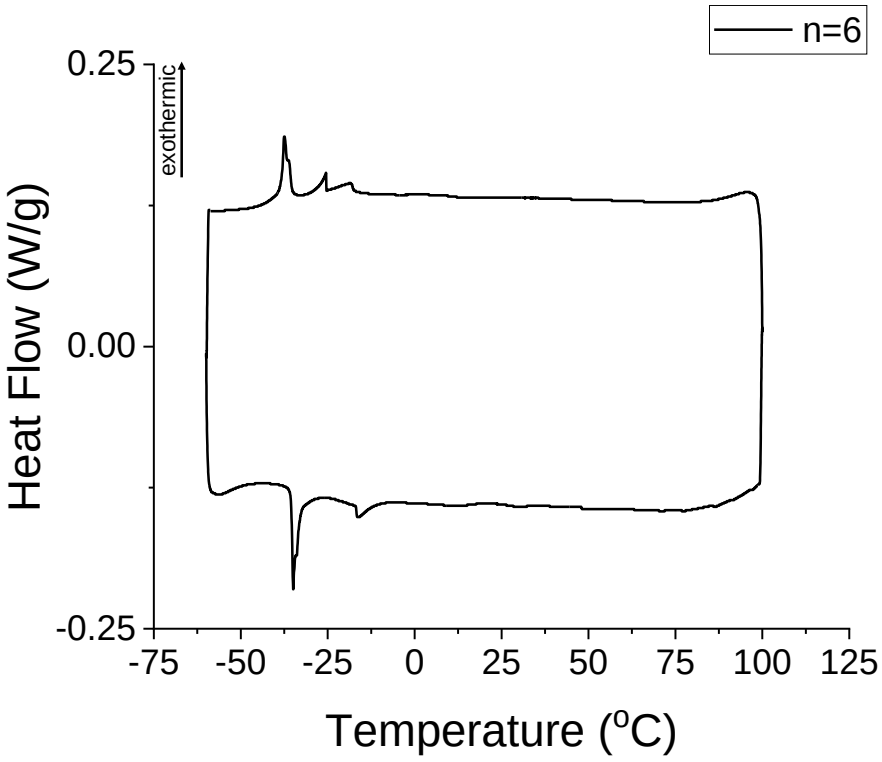

Figure S12: Differential Scanning Calorimetry (DSC) diagrams of n=6 depicting the phase transition that depicts 2 phase transitions at room temperature.

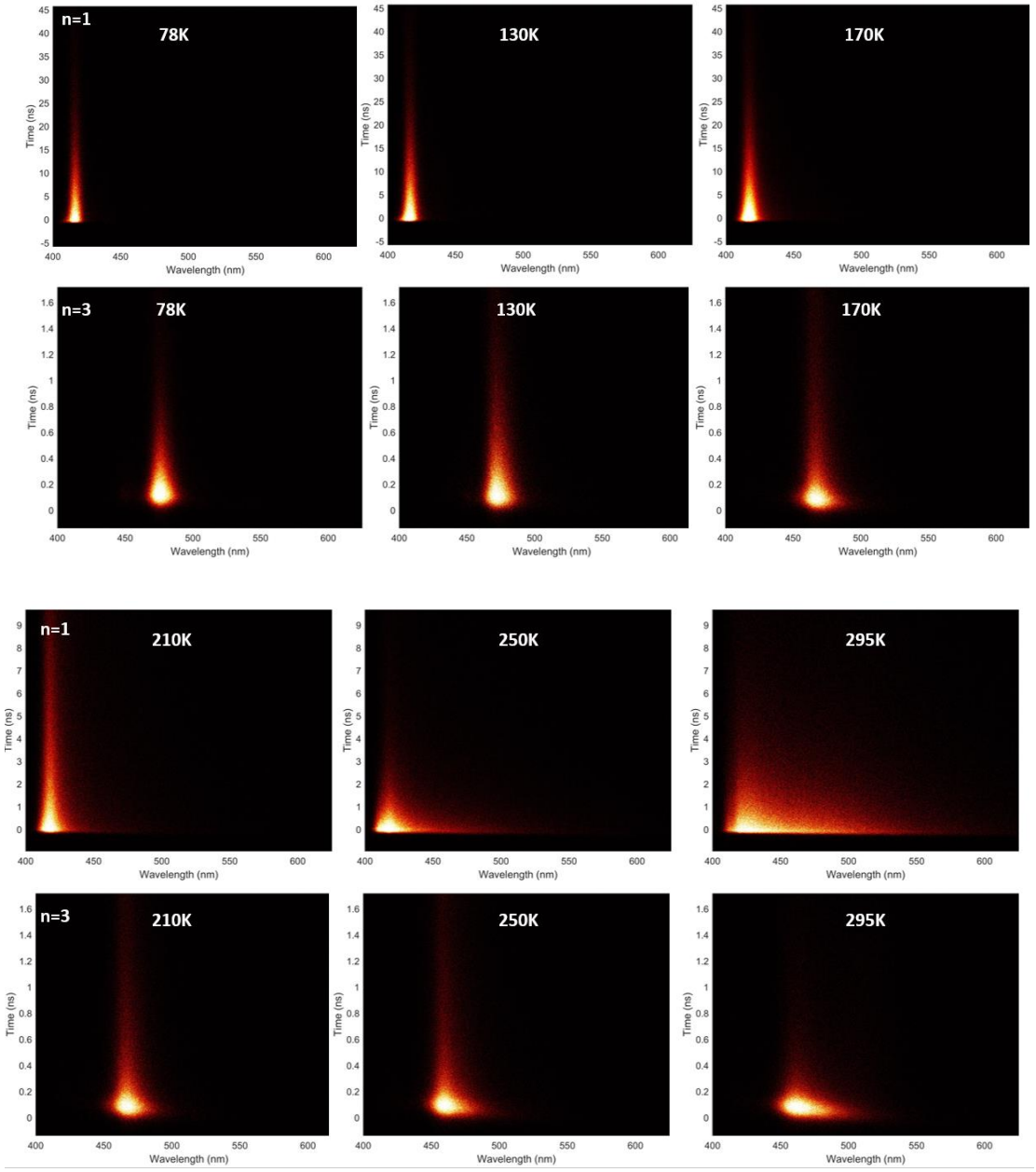

Figure S13: Streak camera images of the n=1 and n=3 compounds at different temperatures, showing all optical phenomena.

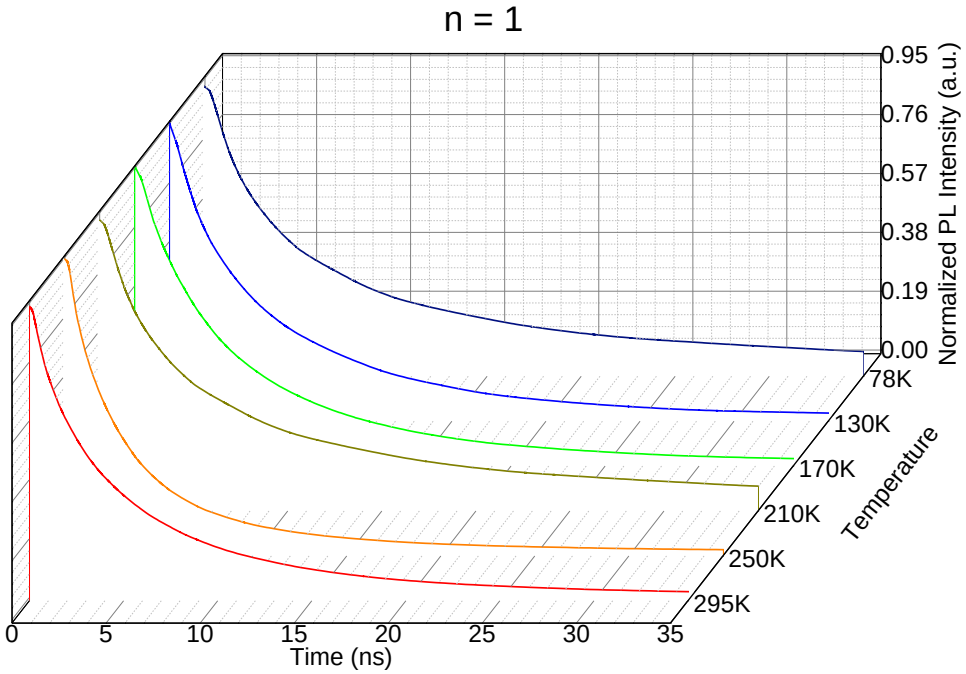

Figure S14: Normalized time resolved PL decay measurements for the n=1 compound plotted against temperature.

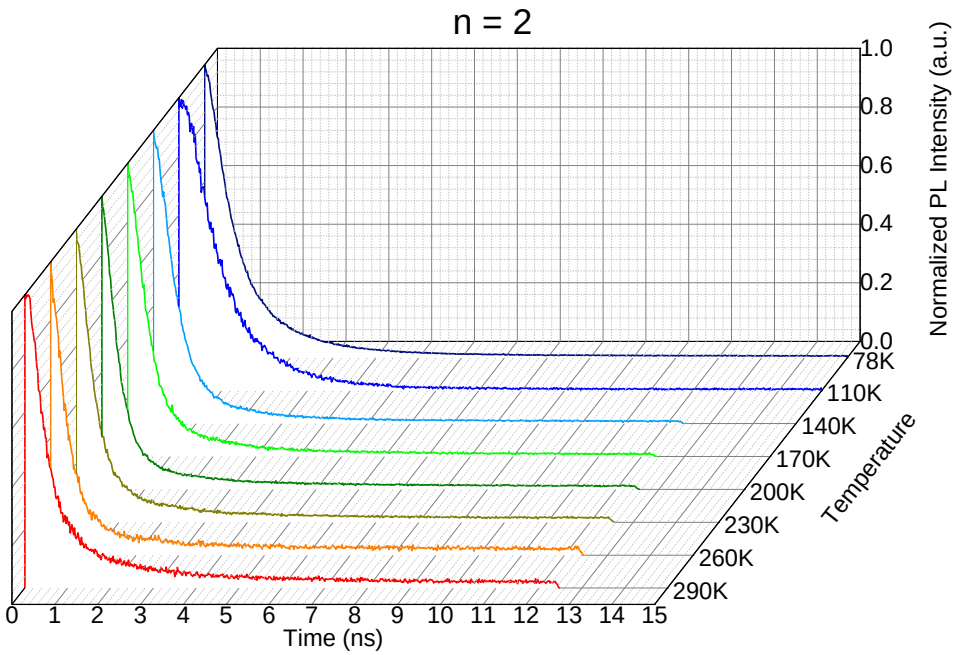

Figure S15: Normalized time resolved PL decay measurements for the n=2 compound plotted against temperature.

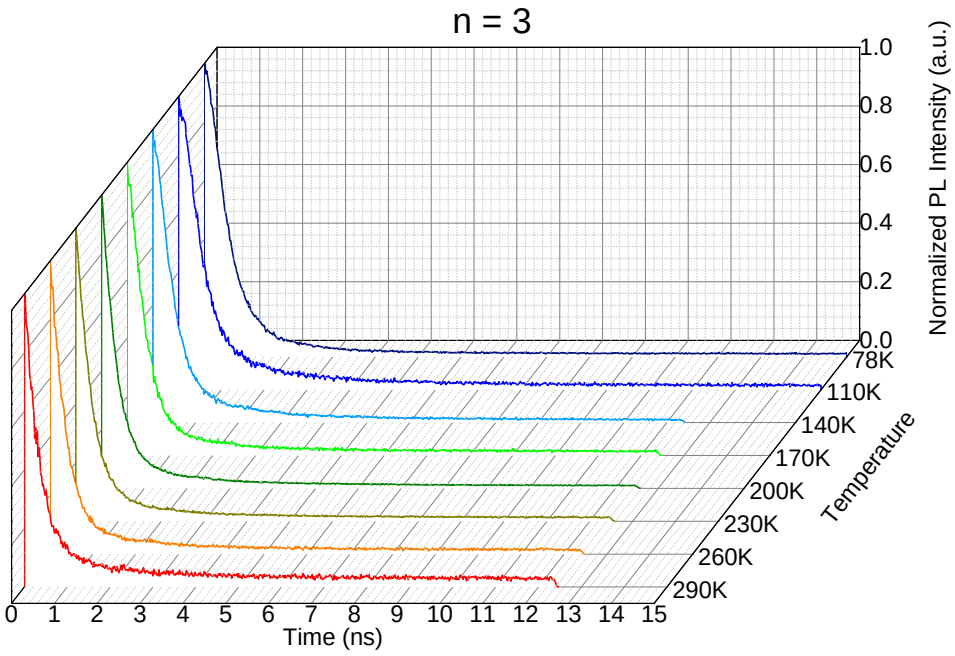

Figure S16: Normalized time resolved PL decay measurements for the n=3 compound plotted against temperature.

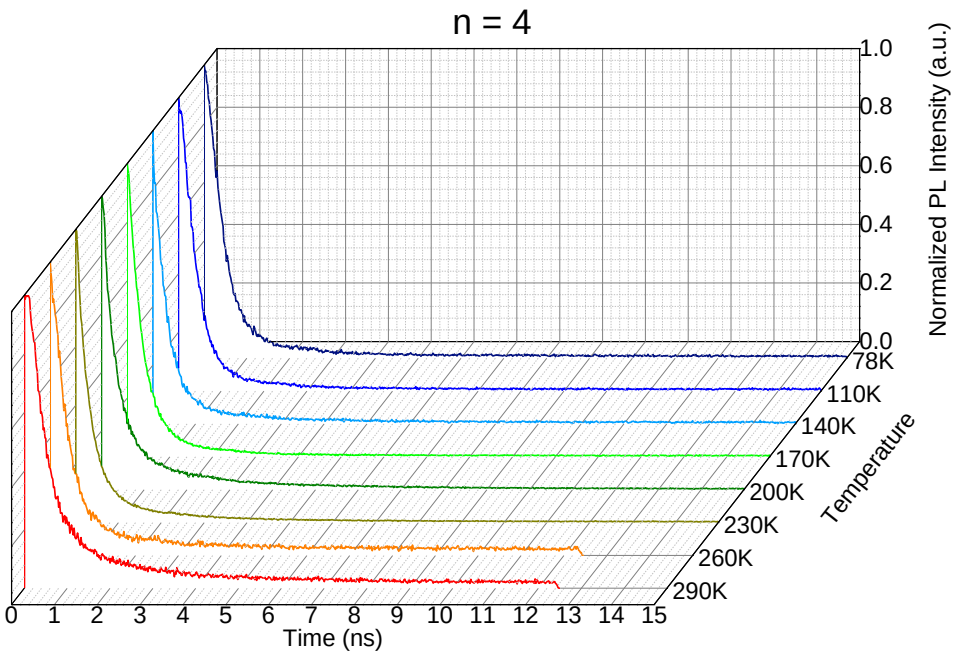

Figure S17: Normalized time resolved PL decay measurements for the n=4 compound plotted against temperature.

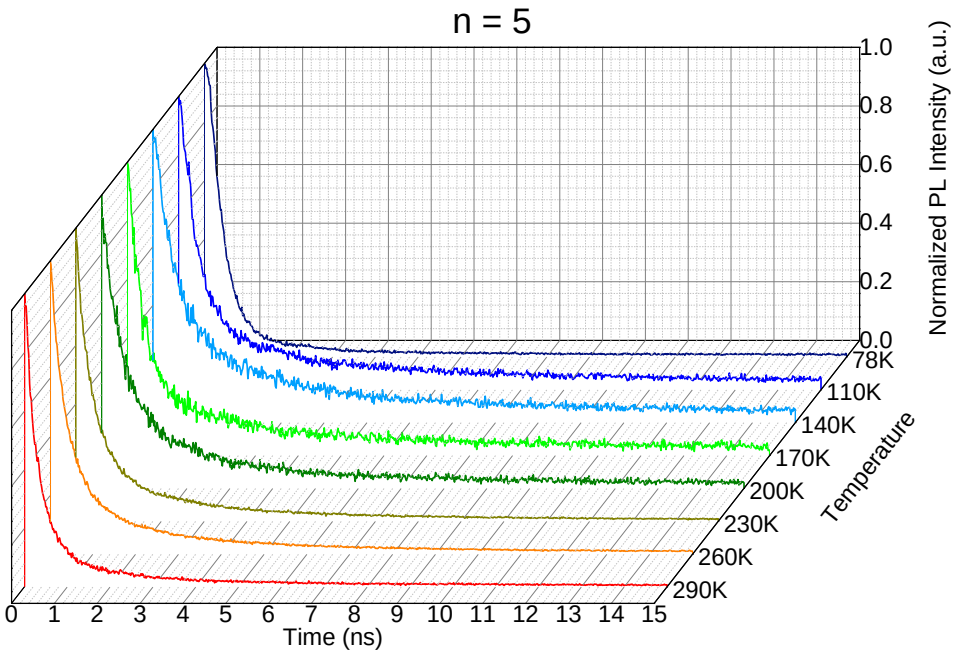

Figure 45: Normalized time resolved PL decay measurements for the n=5 compound plotted against temperature.

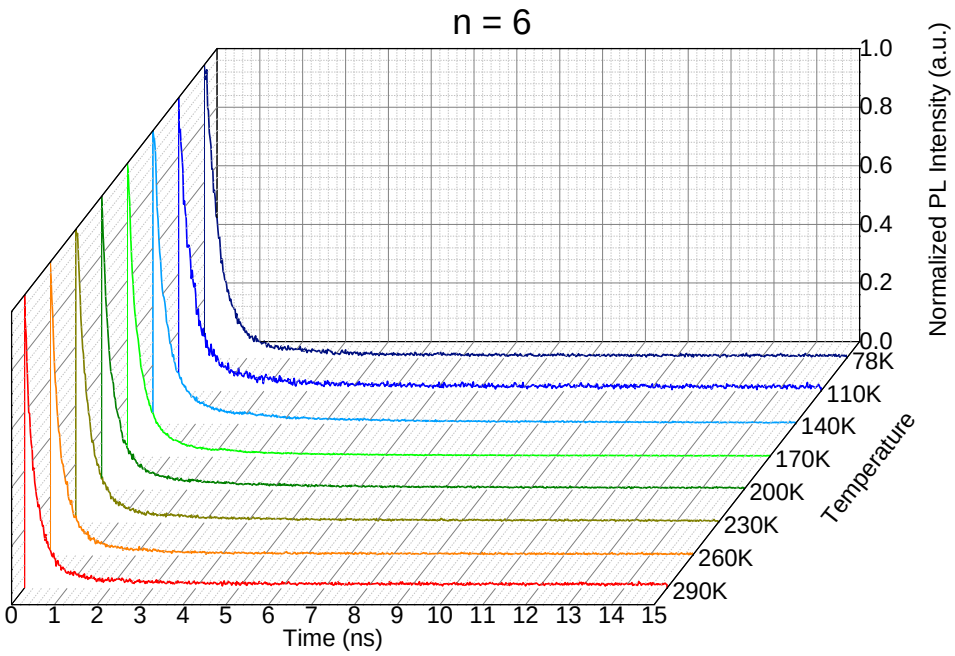

Figure S19: Normalized time resolved PL decay measurements for the n=6 compound plotted against temperature**.**

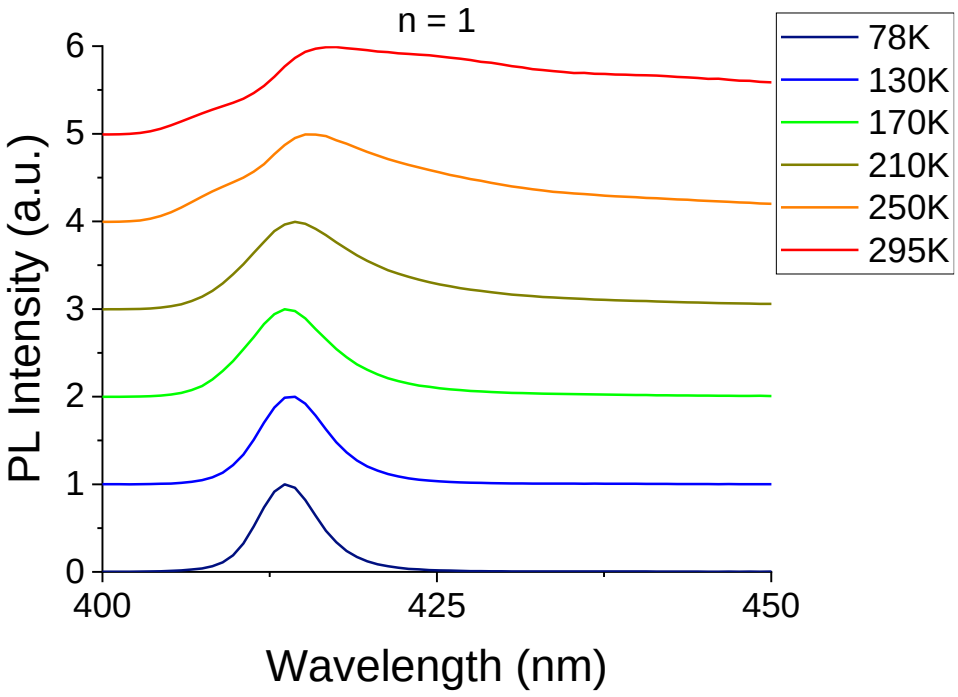

Figure S20: Temperature-dependent photoluminescence measurements for the n=1 compound.

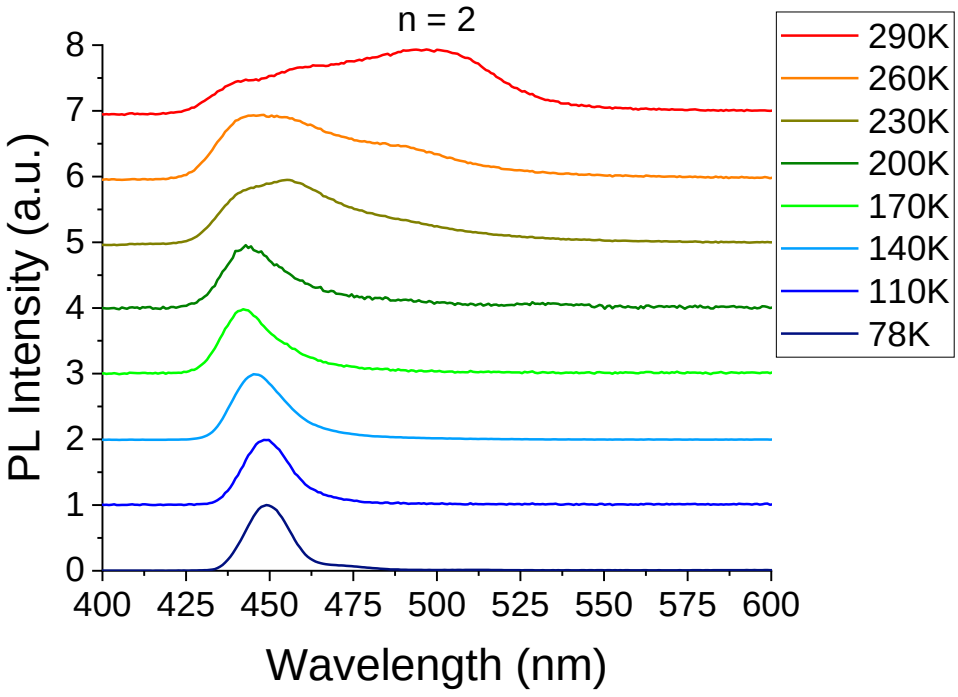

Figure S21: Temperature-dependent photoluminescence measurements for the n=2 compound.

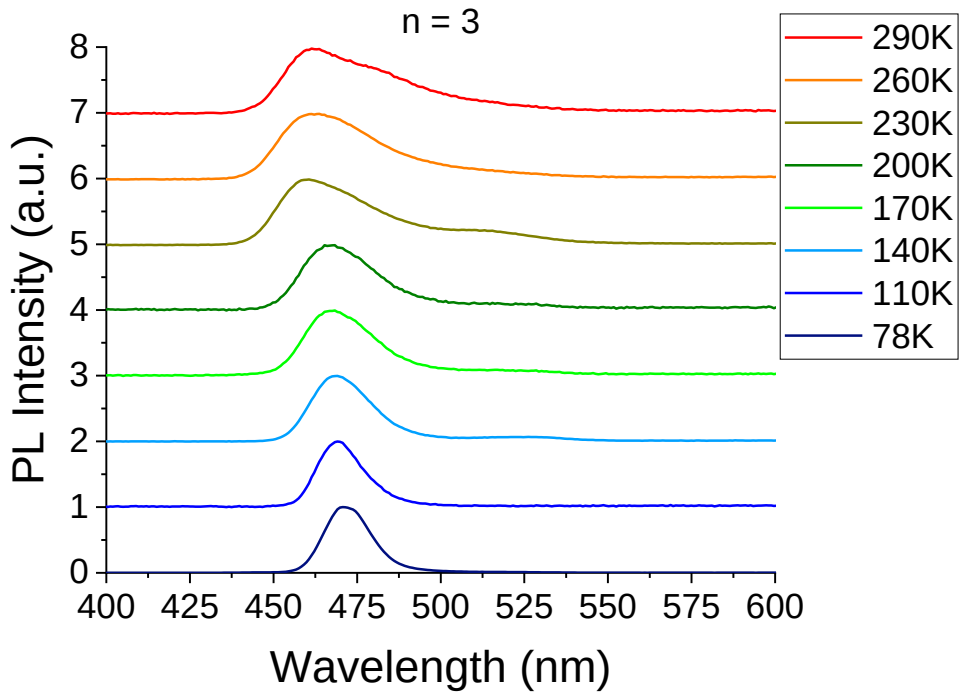

Figure S22: Temperature-dependent photoluminescence measurements for the n=3 compound.

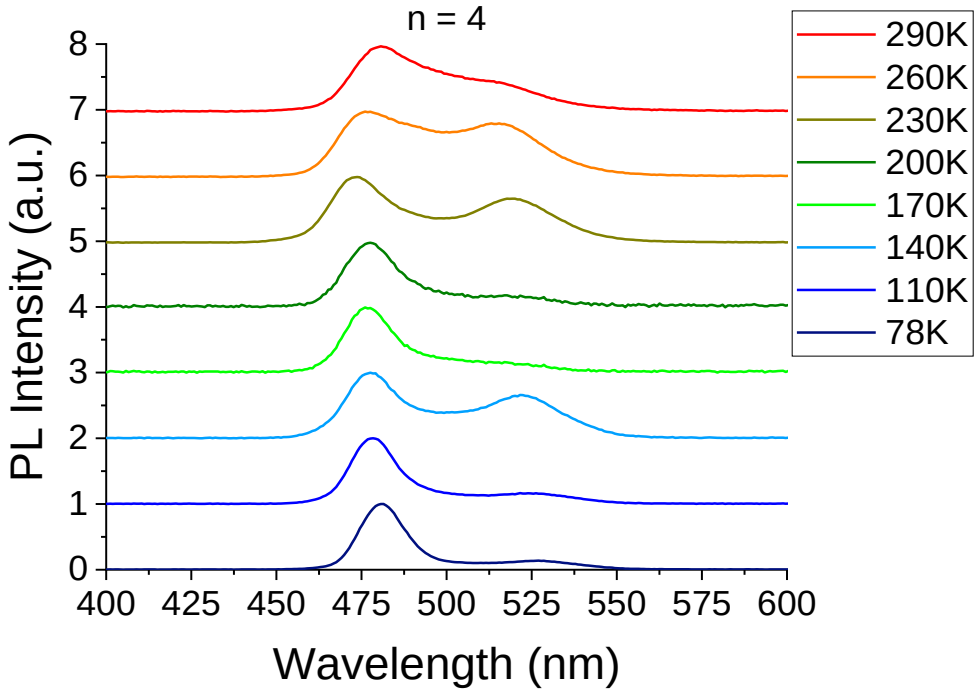

Figure S23: Temperature-dependent photoluminescence measurements for the n=4 compound.

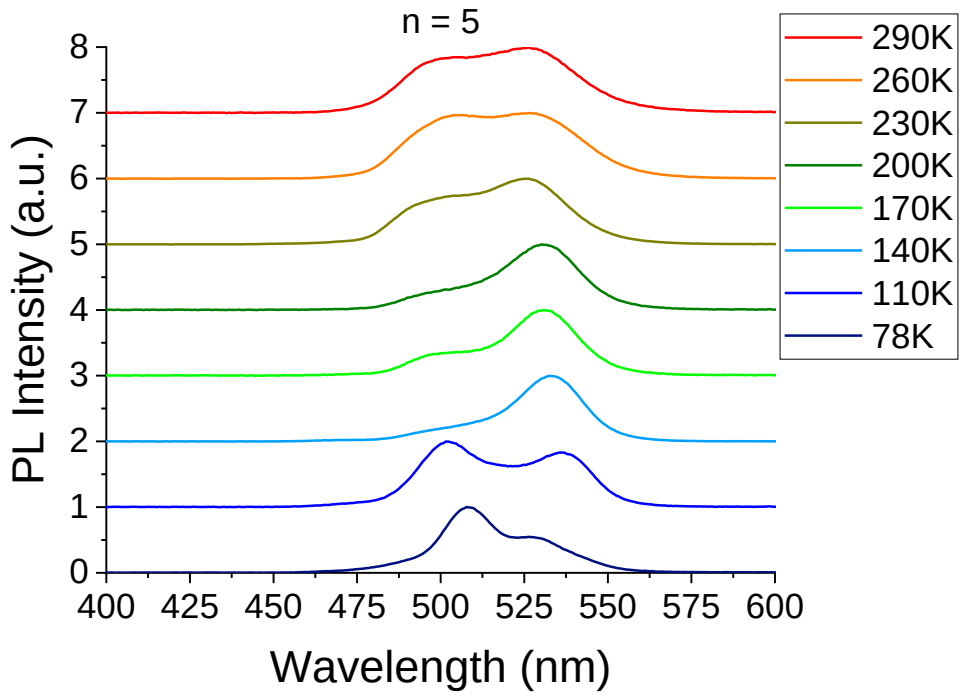

Figure S24: Temperature-dependent photoluminescence measurements for the n=5 compound.

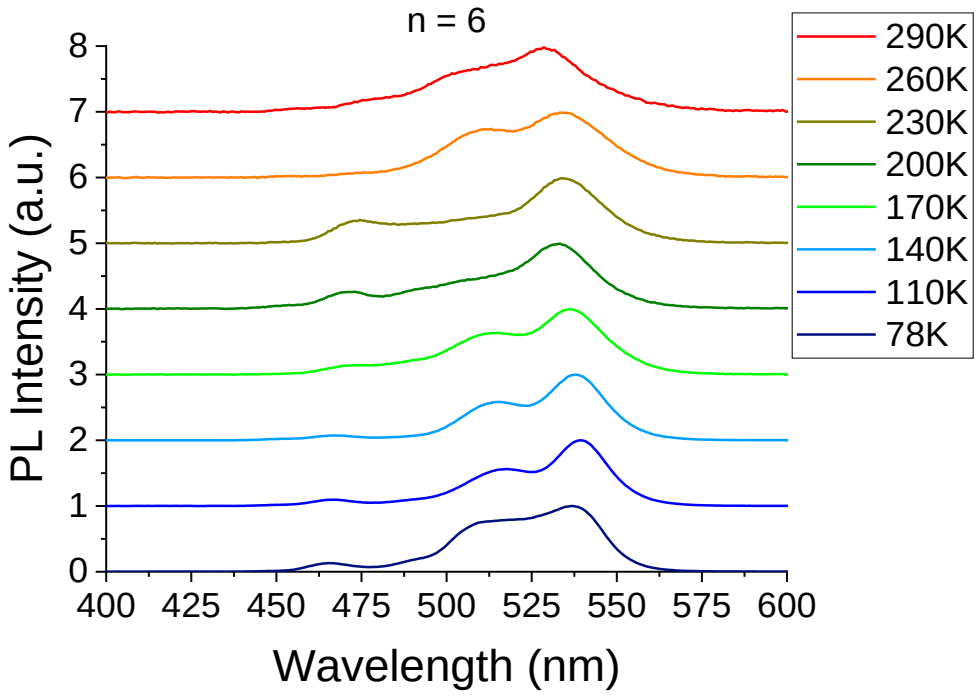

Figure S25: Temperature-dependent photoluminescence measurements for the n=5 compound.

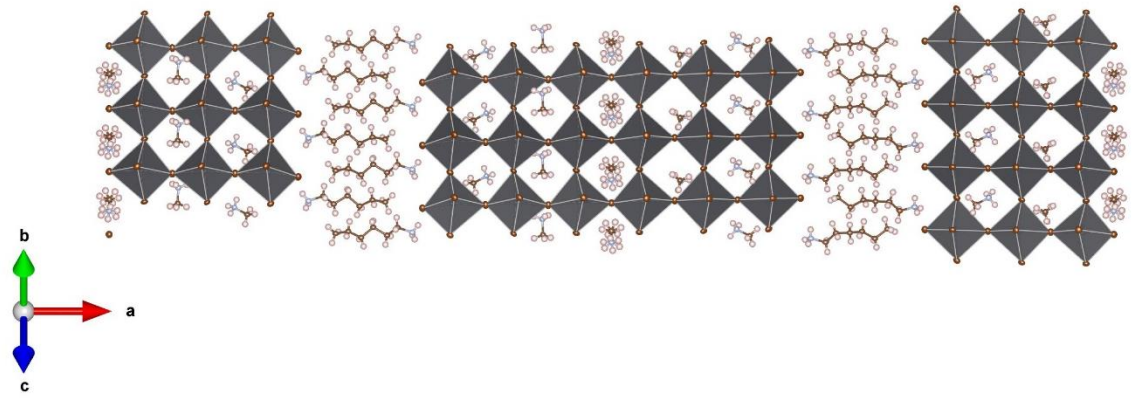

Table S5. Partially solved structure of the n=6 member at 293K.

Compound	(HA)2(MA)5Pb6Br19
Empirical Formula	C17 H62 Br19 N7 Pb6
Formula Weight	731.2
Temperature (K)	293
Wavelength (Å)	0.71073
Crystal System	Orthorhombic
Space Group	*Aea*2
Unit Cell Dimens **a (Å)** **b (Å)** **c(Å)** **α (deg)** **β (deg)** **γ (deg)**	a = 94.82690 b = 8.37010 c = 8.37060 α = 90 β = 90 γ = 90
V (Å^3)	6643.83
Z	4